Modeling and Control of Modular Multilevel Converter Based on Ordinary Differential Equations and Its Applications for HVDC System

Haihao Jiang



Department of Electrical & Computer Engineering

McGill University

Montréal, Canada

December 2019

A thesis submitted to McGill University in partial fulfillment of the requirements for the degree of Doctorate of Philosophy in Electrical Engineering.

Abstract

High-voltage direct current (HVDC) system is more efficient than high-voltage alternating current (HVAC) system for long-distance, bulk power transmission. Modularity, flexibility, reliability and high efficiency make the modular multilevel converter (MMC) the topology of choice in HVDC applications. Because the increasing number of installations shows that the MMC-HVDC is the HVDC of the future, this thesis is continuing research to advance the capability of the MMC-HVDC.

This thesis focuses on fast simulation capability and control strategies for the MMC-HVDC. The main objectives are: (1) to develop a fast and accurate simulation model of a single MMC station and models of multi-terminal MMC-HVDC stations (MTDC-MMC); (2) to investigate the method to design proper parameters for high damping; (3) to design the MMC-HVDC with the capability of power oscillation damping (POD).

Simulation is computation-intensive in MMC. The thesis develops a fast and accurate method by which an MMC station is modeled by ordinary differential equations (ODE). The proposed MMC ODE model is implemented in MATLAB SIMULINK and its correctness is validated by the MMC Detail Equivalent Model (DEM) in RT-LAB. Taking advantage of its speed and accuracy, a Four-Terminal MMC-HVDC system based on the MMC ODE model is developed. The ODE model meets the speed and accuracy requirements of power systems engineers who are concerned with planning, operation and protection studies.

As the ordinary differential equations are nonlinear, small perturbation about a steady-state is applied to obtain the linearized time-periodic matrix. The steady-state takes a long time to simulate because it depends on the transients to have all damped out. The method of Aprille and Trick is applied. Simulation converges to the steady-state in one cycle of 50 Hz. The resultant linearized matrix is time-periodic. The Floquet-Lyapunov Theorem is applied to construct the state-transition matrix from the linearized time-periodic matrix. The eigenvalues of the state-transition matrix contain the coefficients of damping. Graphs of damping coefficients plotted against different sizes of circuit parameters are displayed to assist designers in realizing high damping.

The thesis looks for opportunities to add value to the MMC-HVDC. The active power transmissibility of AC transmission lines is limited by the transient stability limit which is

significantly below the thermal limit. Extensive research and development have been pursued to increase the transient stability limit by flexible AC transmissions system (FACTS). This thesis seeks to use the MMC-HVDC to operate as power oscillation damper to increase the power transmissibility.

The thesis looks for opportunities to integrate previously proven control methods into a common universal control. The Universal Controller brings together the deadbeat control, the circulating current suppression control (CCSC), the POD and the decoupled P-Q strategy in the control of the MMC-HVDC station by the MMC ODE model. Deadbeat control enables the MMC to survive destructively large AC fault currents to improve the transient stability of AC grids.

Résumé

Le système à courant continu haute tension (CCHT) est plus efficace qu'un système à courant alternatif haute tension (CAHT) pour le transport d'électricité sur de longues distances et en vrac. Modularité, flexibilité, fiabilité et haute efficacité font du convertisseur multiniveaux modulaire (MMC) la topologie de choix pour les applications CCHT. Parce que le nombre croissant d'installations montre que le MMC-CCHT est le CCHT de l'avenir, cette thèse poursuit la recherche pour faire progresser la capacité du MMC-CCHT.

Cette thèse porte sur la capacité de simulation rapide et les stratégies de contrôle pour le MMC-CCHT. Les objectifs principaux sont : (1) développer un modèle de simulation rapide et précis d'une seule station MMC et des modèles de stations MMC-CCHT multi-terminales (MTDC-MMC); (2) étudier la méthode de conception de paramètres appropriés pour un amortissement élevé; (3) concevoir le MMC-CCHT avec la capacité d'amortissement par une oscillation de puissance (POD).

La simulation est intensive en calcul dans le MMC. La thèse développe une méthode rapide et précise par laquelle une station MMC est modélisée par des équations différentielles ordinaires (ODE). Le modèle MMC ODE proposé est implémenté dans MATLAB SIMULINK, et son exactitude est validée par le MMC Detail Equivalent Model (DEM) dans RT-LAB. Tirant profit de sa vitesse et de sa précision, un système MMC-CCHT à quatre bornes basé sur le modèle MMC ODE est développé. Le modèle ODE répond aux exigences de vitesse et de précision des ingénieurs de réseaux électriques qui s'occupent des études de planification, d'exploitation et de protection.

Comme les équations différentielles ordinaires sont non linéaires, une petite perturbation autour d'un état stable est appliquée afin d'obtenir la matrice temps-périodique linéarisée. Il faut beaucoup de temps pour simuler l'état d'équilibre, car celui-ci dépend des transitoires pour avoir tout amorti. La méthode de l'aprille et de l'astuce est appliquée. La simulation converge vers l'état d'équilibre en un cycle de 50 Hz. La matrice linéarisée qui en résulte est temporelle et périodique. Le théorème Floquet-Lyapunov est appliqué pour construire la matrice de transition d'état à partir de la matrice temps-périodique linéarisée. Les valeurs propres de la matrice de transition d'état contiennent les coefficients d'amortissement. Des graphiques des coefficients d'amortissement

tracés en fonction de différentes tailles de paramètres de circuit sont affichés pour aider les concepteurs à réaliser un amortissement élevé.

La thèse cherche des occasions d'ajouter de la valeur à MMC-CCHT. La transmissibilité de la puissance active des lignes de transmission CA est limitée par la limite de stabilité transitoire qui est très inférieure à la limite thermique. D'importants travaux de recherche et de développement ont été poursuivis afin d'augmenter la limite de stabilité transitoire par un système de transmission flexible à courant alternatif (FACTS). L'opportunité saisie par cette thèse est d'utiliser MMC-CCHT pour fonctionner comme amortisseur d'oscillations de puissance afin d'augmenter la transmissibilité de puissance.

La thèse cherche des possibilités d'intégrer des méthodes de contrôle éprouvées antérieures dans un contrôle universel commun. Universal Controller réunit le contrôle des temps morts, le contrôle de la suppression du courant de circulation (CCSC), le POD et la stratégie P-Q découplée dans le contrôle de la station MMC-CCHT par le modèle MMC ODE. Le contrôle du temps mort permet au MMC de survivre à des courants de défaut CA destructeurs importants afin d'améliorer la stabilité transitoire des réseaux CA.

Acknowledgement

First and foremost, I would like to thank Prof. Xiaozhe Wang, my supervisor, for her valuable guidance and financial support throughout my Ph.D. work.

I would express the sincerest appreciation from the bottom of my heart to my co-supervisor Prof. Boon-Teck Ooi, for his expert guidance and continuous encouragement throughout my work. He provided me with this research opportunity and promising topic to help me complete my Ph.D. degree. He provided support and helped not only in research work but also in personal life, for which I am fully grateful.

I must thank Prof. Géza Joós for his expert advice for research and financial support to help me complete my Ph.D. degree.

I would like to express my gratitude to Professor Hannah Michalska, Professor Luiz A. C. Lopes, and my Ph.D. committee members for their helpful suggestions and encouragement.

I am also grateful to Prof. Yunwei Li from the University of Alberta for his valuable suggestions and supervision during my research-student exchange from January to May 2018.

I would like to acknowledge Dr. Wei Li and Mr. Jean Bélanger who offered me an internship opportunity at Opal-RT Technologies.

Furthermore, I want to thank all the colleagues and friends at Electric Energy Systems Laboratory of McGill: Avishek Paul, Chu Sun, Debi Prasad Mishra, Diego Mascarella, Dr. Dmitry Rimorov, Dr. Etienne Veilleu, Farah Awan, Dr. Fei Zhang, Georgia Pierrou, Ilias Zenelis, Dr. Hao Sheng, Harmeet Cheema, Jinpeng Guo, Jinling Qi, Dr. Martine Chlela, Dr. Michael Ross, Mohamed Awadalla, Dr. Mike Quashie, Navdeep Kaur Dhaliwal, Dr. Qiushi Cui, Qiyun Dang, Dr. Reza Jalayer Shijia Li, Sanja Dzeletovic, Sijie Qin, Sourabh Sharma, Dr. Subhadeep Bhattacharya, Dr. Syed Qaseem Ali, Yuchong Huo, and Zhiqi Zhao, for their help and inspiring discussions.

I very much appreciate the help I received from the colleagues at OPAL-RT: Fei Gao, Weihua Wang, and Xiao Xiao.

At last, I would like to express my deepest gratitude to my dear family. None of the research work would have been possible without their unconditional support and consistent encouragement. I cannot express what their support means to me.

Contents

Abstı	ract	· • • • • • •		i
Résu	mé			. iii
Ackn	ow]	ledg	ement	v
Cont	ent	S		. vi
List o	of F	igur	es	X
List o	of T	able	es	xiii
List o	of S	ymb	ools	xiv
List o	of A	croi	nyms	xvi
Chap	ter	1.	Introduction	1
1.1		Bac	kground	1
1.2		Lite	rature review	2
1	.2.1	-	HVDC systems	2
1	.2.2	2	Modular Multilevel Converters	6
1	.2.3	3	Power Oscillation of Damping (POD)	12
1	.2.4	1	Damping Sensitivity to Parameters	14
1.3		Pro	blem Statement	14
1.4		Obj	ectives and Contributions	14
1.5		Met	hodology	.15
1	.5.1	-	Mathematic Analysis	.15
1	.5.2	2	Simulation Tools	16
1.6		The	sis Outline	16
Chap	ter	2.	Modular Multilevel Converters	18
2.1		Intr	oduction	18
2.2	2	MM	IC Topologies	18
2.3	}	MM	IC Operation Principle	22
2	2.3.	1	Operation Principle	22
2	2.3.	2	Nearest Level Modulation (NLM) Method	25
2.4		MM	IC Equivalent Circuit	30
2	2.4.	1	Derivation of Neutral Voltage	30
2	2.4.	2	AC and DC equivalent Circuit	31

2.5	Ch	apter Summary	വ
Ŭ		Modular Multilevel Converter Model based on Ordinary Differential	··· 33
-	_	DDE)DE	34
3.1		roduction	
3.2		AC ODE Model	
3.2	2.1	Capacitor Modulation Theory	
3.2	2.2	Single-Phase MMC ODE Model	
3.2	2.3	Three-Phase MMC ODE Model	
3.3	Cir	culating Current Suppression Control (CCSC)	
3.3	3.1	Principle of CCSC	42
3.3	3.2	CCSC Tests	44
3.4	Gro	ounding WYE Connection of AC-Side Transformers Tests	46
3.5		Capacitor Size Tests	
3.5	5.1	Over-Voltage Tests	48
3.5	5.2	Root Mean Square (RMS) Current Tests	
3.6	Mo	del Validation Tests	
3.7	Cha	apter Summary	52
Chapte	er 4.	Dynamic Characteristics Analysis of Modular Multilevel Converters	54
4.1	Int	roduction	54
4.2	No	nlinear and Linearized Models of MMC	55
4.2	2.1	Nonlinear MMC ODE Model	55
4.2	2.2	Model Linearization	55
4.2	2.3	Periodic [At]=[A(t+T)] Matrix	56
4.2	2.4	State-Transition Matrix $\Phi(T,0)$.	56
4.2	2.5	Dynamics of Discrete-Time System	58
4.3	Fas	st Convergence to Steady-State by the Method of Aprille And Trick	60
4.4	Gra	aphs of Damping Coefficients	62
4.4	4.1	Validation of Method	64
4.4	4.2	Bifurcated Regions	67
4.5	Cha	apter Summary	69
Chapte	er 5.	Hybrid AC-DC Platform Using MMC-HVDC based on the ODE Model	70
5.1	Int	roduction	70
5.2	Mu	lltiterminal MMC-HVDC System Based on ODE Model	71
5.3	Int	egrating Multi-Terminal MMC-HVDC	74
5.3	3.1	Stray Capacitor Technique	74

5.3	.2 Modulation Signal Control by M and δ _R	74
5.4	Control of Multi-Terminal MMC-HVDC Platform	75
5.4	.1 DC Voltage Regulator	75
5.4	.2 Station to Receive Stochastic Power	76
5.4	.3 Circulating Currents Suppression Control	76
5.5	Simulation Results	78
5.5.	.1 Test Scenario	79
5.5.	.2 Circulating Currents in Validation Test	83
5.5.	.3 Simulation Speed Comparison	84
5.6	Chapter Summary	84
Chapte	r 6. Damping Capability of MMC-HVDC based on the ODE Model	85
6.1	Introduction	85
6.2	Property Required for Damping	86
6.2	.1 Small Signal Linearization	87
6.2	.2 Dynamics Small Signal Linearization with Damping	88
6.3	Damping Power Implementation	89
6.3	.1 Principle of PLL Operation	89
6.3	.2 Frequency of Power Oscillation	90
6.4	Damping by Modular Multilevel Converter (MMC)	90
6.4	.1 MMC-HVDC and Modulating Signals	90
6.4	.2 Incorporating Signal for Power Oscillation Damping	91
6.5	Multiple Control Capability in MMC-HVDC	92
6.5	.1 Damping control	92
6.5	.2 Decoupled P-Q Control	92
6.5	.3 Regulated Current Control	92
6.6	Simulation Results	94
6.6	.1 Simulation Test Platform	94
6.6	.2 Damping Capability Tests	95
6.6	.3 Transient Stability Test Conditions and Results	96
6.6	.4 Increasing Power Transmissibility by MMC-HVDC Damping	100
6.6	.5 Impact of Damping Power on Ratings of MMC Components	100
6.7	Chapter Summary	102
Chapte	r 7. Conclusions and Future work	103
7.1	Conclusions	103
7.2	Future Work	104

		ix
Appendix A.	Clarke and Park Transformation	105
Appendix B.	Digital Closed-Loop Deadbeat Control	107
Appendix C.	Parameters used in MMC-HVDC Damping Tests	110
References		112

List of Figures

Fig. 1-1 Configuration of the MMC	7
Fig. 1-2 Different topologies of the MMC Sub-Modules.	7
Fig. 2-1 Schematic of 3-phase HBSM-MMC.	19
Fig. 2-2 SM operation states: (a) state 1: T_1 and T_2 are off, i_{SM} is flowing through D_1 or D_2	¹ ₂ ; (b)
state 2: T_1 is on, T_2 is off, i_{SM} is flowing through T_1 or D_1 ; (c) state 3: T_1 is off, T_2 is on,	i _{SM} is
flowing through T_2 or D_2	20
Fig. 2-3 Illustration of the operation of a five-level MMC.	23
Fig. 2-4 Illustration of the phase-a operation of the 5-level MMC.	24
Fig. 2-5 Operation principle of the NLM method.	26
Fig. 2-6 Output voltage of the MMC phase-a: (a) 21-level; (b) 41-level; (c) 61-level	27
Fig. 2-7 FFT of the output voltage of the MMC phase-a: (a) 21-level; (b) 41-level; (c) 61-level	vel 28
Fig. 2-8 Simplified circuit of a three-phase MMC	29
Fig. 2-9 AC side equivalent circuit of a three-phase MMC	32
Fig. 2-10 DC side equivalent circuit of a three-phase MMC	32
Fig. 3-1 Phase-a of the MMC showing n_{ua} capacitors string in the upper arm and n_{la} capacitors	citors
string in the lower arm.	36
Fig. 3-2 (a) Modulation signal $m_{ua}(t)$; (b) $n_{ua}(t)$, number of capacitors, connected in string in u	upper
arm as commanded by $m_{ua}(t)$; (c) output voltage u_a	37
Fig. 3-3 AC side equivalent circuit of the MMC phase-a	39
Fig. 3-4 DC side equivalent circuit of the MMC phase-a	39
Fig. 3-5 i_{cira} , i_{cirb} , i_{circ} of the three-phase MMC ODE Model	45
Fig. 3-6 i_{diffa} , i_{diffb} , i_{diffc} of the three-phase MMC ODE Model	45
Fig. 3-7 Capacitor voltage in the phase-a upper arm.	45
Fig. 3-8 Simulations of 3-phase AC currents when AC-side transformers have grounded	WYE
connection. (a) without CCSC; (b) with CCSC.	46
Fig. 3-9 Simulations of current flowing in the ground wire. (a) without CCSC: (b) with CCS	C. 46

Fig. 3-10 FFT of the phase-a AC currents when the AC-side transformers have a grounded WY	E
connection	7
Fig. 3-11 FFT of current flowed in the ground wire.	7
Fig. 3-12 Percentage Over-Voltage of the IGBT in SM	9
Fig. 3-13 RMS value sub-module current as a function of <i>C</i>	9
Fig. 3-14 Total capacitor voltage in the upper arm of the MMC phase-a5	0
Fig. 3-15 Total capacitor voltage in the lower arm of the MMC phase-a5	0
Fig. 3-16 Differential current of the MMC phase- <i>a</i> 5	0
Fig. 3-17 AC current of the MMC phase-a5	1
Fig. 3-18 Circulating current of the MMC phase-a5	1
Fig. 3-19 Output ac voltage of the MMC phase-a5	1
Fig. 4-1 Eigenvalues of $\Phi(T,0)$ and the unit circle	9
Fig. 4-2 Convergence to steady-state $X_0(t)$ by $t=T=0.02$ s using the method of Aprille and Trick 6	1
Fig. 4-3 Magnitude of Eigenvalue vs C_{arm} (L_{ac} =5mH, L_m =5mH, R_{ac} =0.1 Ω)6	3
Fig. 4-4 Magnitude of Eigenvalues vs L_m (C_{arm} =0.4167mF/arm, L_{ac} =5mH, R_{ac} =0.1 Ω)6	3
Fig. 4-5 Magnitude of Eigenvalues vs L_{ac} (C_{arm} =0.4167mF/arm, L_m =5mH, R_{ac} =0.1 Ω)6	3
Fig. 4-6 Magnitude of Eigenvalues vs R_{ac} (C_{arm} =0.4167mF/arm, L_{ac} =5mH, L_{m} =5mH)6	3
Fig. 4-7 Complex Mode $\gamma 1,2 = -0.4608 \pm j0.6627$ ($C_{arm} = 0.25 \text{mF/arm}$)	6
Fig. 4-8 Mode of $\gamma 1 = 0.8371$ ($C_{arm} = 0.379$ mF/arm)6	6
Fig. 4-9 Mode of $\gamma 2 = 0.7478$ ($C_{arm} = 0.367 \text{mF/arm}$)6	6
Fig. 4-10 50-Hz measurement of the FFT of the total upper capacitor voltage $u_{\sum cua}$ 6	7
Fig. 4-11 100-Hz measurement of the FFT of the total upper capacitor voltage $u_{\Sigma cua}$ 6	7
Fig. 4-12 Upper arm voltage $u_{\sum cua}$ showing force-resonance because C/N is chosen around peak	S
of Fig. 4-10 and Fig.4-116	7
Fig. 5-1 Radial Multi-Terminal MMC Stations <i>n</i> =1,2,3,47	2
Fig. 5-2 Schematic of phase- j ($j=a, b, c$) of the n^{th} MMC	2
Fig. 5-3 Application of voltage of the Stray Capacitor Method for Station n ($n\neq 2$)7	4
Fig. 5-4 Output active power of the MMC1 to the MMC 4	0
Fig. 5-5 DC current of the MMC1 to the MMC 4	0
Fig. 5-6 DC line currents: (a) between the MMC 1 and the MMC 2, (b) between the MMC 2 and	d
the MMC 3 and (c) between the MMC 3 and the MMC 4	1

Fig. 5-7 DC voltage of the MMC1 to the MMC4	81
Fig. 5-8 Enlargement of Fig. 5-7	82
Fig. 5-9 Simulation by ODE (a) i_{diff} , differential current of a, b and c phase of MMC2 (b	o) i_{cir} ,
circulating current of a, b and c phases of the MMC2. No suppression $t < 0.8$ s. Suppression en	abled:
t > 0.8s	82
Fig. 6-1 Three-phase Phase-Locked Loop (PLL)	89
Fig. 6-2 Schematic of three phases of the MMC-HVDC	91
Fig. 6-3 Multi-Function Control Diagram of the MMC	93
Fig. 6-4 Test system of a radial transmission line with the MMC-HVDC station connected	d in a
shunt.	94
Fig. 6-5 Response to load increase (12.5%) at t=0.5s. (a) rotor speed pu (ac grid frequency	(b)
voltage angle δ ;(c) MMC active power output (pu); (d) MMC reactive power output (pu)	95
Fig. 6-6 Power angle during transient stability test (a) P_e =0.4pu, k_θ =0 stable, k_θ =-0.6 stable.	(b) P_e
=0.7pu, k_{θ} =0 unstable, k_{θ} =-0.6 stable. (c) P_{e} =0.85pu, k_{θ} =0 unstable, k_{θ} =-0.6 unstable. ((d) P_e
=0.75pu, k_{θ} =-0.6 unstable, k_{θ} =-0.8 stable.	97
Fig. 6-7 Active power in transmission line in transient stability test. (a) P_e =0.4pu, k_θ =0 stab	ole, k_{θ}
=-0.6 stable. (b) P_e =0.7pu, k_θ =0 unstable, k_θ =-0.6 stable. (c) P_e =0.85pu, k_θ =0 unstable, k_θ	=-0.6
unstable. (d) P_e =0.75pu, k_{θ} =-0.6 unstable, k_{θ} =-0.8 stable.	98
Fig. 6-8 Voltages, currents, active and reactive power of the MMC-HVDC during the trans-	nsient
stability test.	101
Fig. B-1 Schematic of digital current feedback of deadbeat control block	108
Fig. B-2 Three-phase MMC plant circuit.	108

List of Tables

Table 2-I Summary of the Operating States of the Sub-Module	22
Table 2-II Phase-a operation sequence of the upper arm and lower arm SMs	25
Table 3-I Parameters used in CCSC tests	44
Table 3-II Parameters used in Model Validation Tests.	51
Table 4-I Parameters used in MMC Dynamic Characteristics Tests	63
Table 5-I Parameters used in MTDC-MMC-HVDC Test	82
Table 5-II Comparisons of the computing time between the ODE model and the DEM	obtained
from MATLAB/ SIMULINK	83
Table 6-I Transient Stability Test	98
Table 6-II Power Transmissibility Gain from Damping	99

List of Symbols

C MMC sub-module capacitor

Carm MMC arm equivalent capacitor

 C_{bp} Stray capacitor technique Capacitance

 i_a , i_b , i_c MMC output three-phase ac current

 I_{ac} Magnitude of ac output current

 i_{cir} MMC Circulating current

 i_d , i_q d-q components of 3-phase ac currents

*i*_{dc} MMC DC current

 i_{diff} MMC differential current

 i_{SM} Current flows in the Sub-Module

 i_u , i_l Current of MMC upper arm and lower arm

j Phase-j, j=a,b,c

J Moment inertia

 k_{θ} Damping control gain

Lac AC system inductance

 L_m MMC arm inductor

 m_u, m_l Modulating signal of MMC upper arm and lower arm

Magnitude of controlled modulation signal

 n_u , n_l Total Sub-module number inserted in upper arm and lower arm

N Total number of sub-modules in one arm of MMC

P, Q Active power and reactive power

P_e Generator transmitted active power

q Electric charge of a capacitor

 R_{bp} damping resistor

 R_{ac} AC system resistance

 R_m MMC arm equivalent resistance

 T_e Generator counter-torque

 T_t Turbine torque

 u_a , u_b , u_c MMC output three-phase ac voltage

u_c Sub-module capacitor voltage

 u_{cu} u_{cl} Total capacitor voltages inserted in the upper arm and lower arm

 U_{dc} MMC dc bus pole to pole voltage

u_n Neutral voltage

 u_{SM} Output voltage of one sub-module

 u_{ref} MMC reference voltage

 $u_{\sum cu}$ $u_{\sum cl}$ Sum of capacitor voltages in the upper arm and lower arm

 v_a, v_b, v_c AC system three-phase voltage

 $V_{dc\text{-ref}}$ MMC DC reference voltage

 v_{α}, v_{β} α, β components of three-phase voltage

 v_d, v_q d, q components of three-phase voltage

VPCC Voltage of the point of common coupling

X Equivalent transmission line impedance

 ω Angular velocity or frequency

 ϖ Power oscillation frequency

FFT

List of Acronyms

AC, ac Alternative Current

CCSC Circulating Current Suppression Control

CDSM Clamped Double-Cell Sub-Module

CHB Cascaded H-Bridge

CPU Central Processing Unit
CSC Current Source Converter

DC, dc Direct Current

DEM Detail Equivalent Model
EMT Electromagnetic Transient

EMTP Electromagnetic Transient Process

FACTS Flexible Alternative Current Transmission Systems

Fast Fourier Transform

FBSM Full-Bridge Sub-Module

FPGA Field-Programmable Gate Array

GTO Gate Turn-Off Transistor
HBSM Half-Bridge Sub-Module

HVAC High Voltage Alternative Current

HVDC High Voltage Direct Current

IGBT Insulated Gate Bipolar Transistor

IGCT Integrated Gate Commutated Thyristor

KVL Kirchhoff's Voltage Law

LCC Line Commutated Converter

MMC Modular Multilevel Converter

MVDC Medium Voltage Direct Current

NLM Nearest-Level Modulation

ODE Ordinary Differential Equation

p. u. Per Unit

PCC Point of Common Coupling

PI Proportional Integral

PLL Phase-Locked Loop

POD Power Oscillation Damping

PSS Power System Stabilizer

PWM Pulse Width Modulation

RMS Root Mean Square

SM Sub-Module

THD Total Harmonic Distortion

Chapter 1. Introduction

1.1 Background

The battle between the alternative-current (AC) system and direct-current (DC) system of the 1880s ended when George Westinghouse, a proponent of AC systems, beat Thomas Edison, the proponent of DC systems, in debates on technical issues. The key factor is that before power electronics, to convert dc power from different levels of voltage is difficult, expensive and inefficient. The voltage generated and distributed by the dc system must be the same as the customers' loads. Low transmission voltage requires the power plants to be placed near loads to avoid high resistance loss in transmission line. For a given amount of transmitted power, transmission by a higher voltage means a lower current, thus reducing the loss in the wires. Increasing the cross-section of the distribution wires can be another solution. However, larger wires are heavier and costlier. The AC system is capable of stepping up and stepping down transmission voltage by AC transformers. This makes long-distance power transmission feasible. Thanks to transformers with capabilities to change the voltage practically, the low-cost AC transmission and distribution systems prevailed in the following years.

Although the AC system has dominated since the 1890s, there are drawbacks. Regional systems, which operate at different frequencies or at the same frequency but at different voltage angles, cannot be interconnected. Underwater projects, whose cables have large capacitive shunt current lowers the power factor. The limit of underwater transmission distance is around 40 km. This is significant in off-shore wind farms. Transient stability limit decreases when the distance reaches 600 miles due to the large series inductive reactance of the transmission lines. Economic concerns arise because the real estate taken by AC transmission towers when compared with DC towers.

However, with the advent of the mercury-arc valve in 1914 [1], practical power conversion between AC and DC systems became applicable and economical. The difficulties of the AC system mentioned above could be overcome by introducing the high voltage direct current (HVDC) system.

Considering the higher cost of the HVDC stations and the lower cost of DC transmission lines, the total cost of the HVDC system may be less than the high voltage alternative current (HVAC) system, a factor dependent on transmission distance. The break-even point for overhead lines is 700 km while 40 km is for submarine cables [2]. For overhead lines, the transmission loss of the HVDC is typically 30%-50% lower than the AC system, and 3% for submarine cable, taking both cable and converter loss into consideration [3]. For submarine cable systems, dc cable avoids large reactive power introduced by large shunt capacitive current of the extruded polymer cable. For cable longer than 80km, large AC cable shunt capacitive current occupies the conduction area so that there is little room for the current of reactive power. Thus, the HVDC is the better solution. Moreover, the HVDC enables the interconnections between unsynchronized AC systems. Two AC systems cannot be interconnected when they have different frequencies, such as 50hz and 60hz, or, when they have different phase angles although sharing the same frequency. Interconnection is possible when each AC system is connected by an HVDC station. As frequency and phase angle disappear at the terminals of the DC lines, the HVDC stations can be connected on the DC side. Bi-directional power transfer can be controlled by the HVDC stations.

HVDC systems also have a less environmental impact fewer overhead transmission lines are required with respect to HVAC systems to deliver the same amount of power. The reduced right-of-way means less space and less visual impact. Because of the advantages mentioned previously, the HVDC is one of the key technologies for future grids with high penetration of renewable energy sources, which are normally located remotely [4], and which require a high level of controllability for frequency change and storage.

1.2 Literature Review

The literature review follows the topics treated in the different chapters of the thesis. Section 1.2.1 presents a brief introduction of HVDC systems. Section 1.2.2 is on modular multilevel converter (MMC). Section 1.2.3 discusses power oscillation damping. Section 1.2.4 concerns itself with damping sensitivity to parameters.

1.2.1 HVDC Systems

1.2.1.1 Early Method of HVDC

The first long-distance direct current transmission system was commissioned in 1889 in Italy. This early system, developed by Swiss engineer René Thury [5], was based on motor-generator sets

connected in series to increase the voltage. However, rotating machinery had a high energy loss and required high maintenance. Because of high cost and low efficiency, only a few Thury systems were constructed.

1.2.1.2 Line-Commutated Converter Based HVDC (LCC-HVDC)

The method based on motor-generators sets was the only method to convert AC power to DC power before the invention of mercury arc rectifier in 1902. The mercury arc rectifier belongs to the family of vacuum tube electronics which began with the diode and the triode. The power rating increased by filling the vacuum with a conducting gas, giving rise to the thyratron and the mercury arc valve. In contrast to motor-generators sets, the mercury arc valve had a much simpler structure and longer-lasting life by taking advantage of liquid mercury being able to self-restoring. However, once turned on, the gate cannot be turned off.. Conduction ceases only when the voltage reverses in the second half of the AC cycle. This mode of operation is known as Line-Commutation. Taking advantage of the mercury arc valve, the first classic HVDC system was commissioned at Gotland in Sweden in 1954 [6]. The HVDC system based on a mercury arc valve was considered as the first generation of the HVDC system.

Mercury arc valves were widely used in HVDC systems until the solid-state revolution in electronics in the 1960s. Parallel to diode, triode and thyratron, researchers for the power industry developed the power diode, thyratron and the silicon rectifier (to replace mercury rectifier). Due to its higher reliability, lower cost, maintenance and environmental risk [7], mercury arc valves were completely replaced by Silicon Rectifier, better known as the thyristor. Thyristor-based HVDC came into being in the 1970s. Similar to the mercury arc valve, thyristor valves can be turned on at the gate but not turned off. Operation of the thyristor-based HVDC depends on line commutation, requiring an external control circuit to turn on the valve. Although the thyristor valve was more advanced, its shortcomings, such as commutation failure limited its application.

The HVDC system based on thyristor valves can be considered as the second generation of the HVDC system. Including mercury arc rectifiers-based systems, thyristors-based HVDC systems were known as Line-Commutated Converter HVDC systems (LCC-HVDC), also referred to as the classic HVDC systems [8]. As the direct current in the LCC-HVDC is kept constant by the large inductance of the long DC transmission line, or by the installation of a large inductance, the LCC-HVDC is also known as the Current Source Converter HVDC (CSC-HVDC).

The first HVDC system based on the thyristor valve was the Eel River Converter Station in Canada delivered by General Electric and commissioned in 1972 for point-to-point connection [9]. The LCC-HVDC has been widely applied to transmit bulk power over a distance greater than 2000 km in North America, Brazil, China, Russia and India. The world's longest transmission distance, highest power rating, and voltage rating the LCC-HVDC system, the Changji-Xinjiang to Xuancheng-Anhui Ultra HVDC project is currently under construction in China (at ±1100 kV, 10GW and 3300km) [10]. Till now, LCC-HVDC systems still dominate in HVDC transmission systems, and the technologies are well established.

Around 1992, an extensive investigation was conducted on realizing a multi-terminal HVDC [11] to interconnect Quebec—New York—New England. The multi-terminal system had a total capacity of 2000MW and DC voltage ±450 kV [12]. The LCC system required redundant telecommunication for the multi-terminal system to operate. Because reliability could not be assured, the project was abandoned although the 2000MW and DC voltage ±450 kV [12] had already been built.

1.2.1.3 Voltage Source Converter Based HVDC (VSC-HVDC)

LCC-HVDC stations are built only when an extremely long transmission distance is required, or when the amount of transmitted power is high enough to justify the high cost. With the advent of fully controlled semiconductors, such as insulated-gate bipolar transistors (IGBTs), gate turn-off transistors (GTOs), and integrated gate-commutated thyristors (IGCTs), fully-controlled power electronics converters became available. This made smaller HVDC systems more affordable. This opens a new market. In fact, ABB, a multi-national manufacturer of HVDC systems, gives the new product the name HVDC LIGHT. Based on the fully-controlled power electronics, the converter is considered the third generation of HVDC systems, also called the voltage source converter based HVDC system (VSC-HVDC).

VSC-HVDC has the following advantages:

- 1) Fully controlled power electronic switches (IGBT, GTO, IGCT) are free from commutation failure during AC network disturbances.
- 2) Transformers assisting the commutating process are no longer required, thus increasing reliability while reducing the cost.
- 3) Independent control of active and reactive power is possible, leading to decoupled P-Q control.

- 4) Ability to operate with pulse width modulation (PWM). This results in a fast dynamic response, and better quality waveforms in spite of the size reduction of the filters, which brings down the cost.
- 5) Possibility to implement controlled current strategies to protect against large AC short circuit fault current.
- 6) Possibility to connect in parallel on the DC side. This makes multiterminal VSC-HVDC feasible.

The first VSC-HVDC project was installed in Hellsjön–Grängesberg in Sweden in 1997 [13]. Due to its many advantages, VSC-HVDC systems are profitable on the market, particularly in terms of: (1) underground or undersea power transmission; (2)converting power from variable frequency systems, particularly renewable energy, such as wind-turbine 50hz or 60 Hz grid; (3) energy trading.

On the other hand, high-frequency PMW operated by VSC-HVDC has high switching losses, Electromagnetic Compatibility/Electromagnetic Interference (EMC/EMI) problems, as well as high-frequency oscillations, which are challenging and being solved gradually only.

1.2.1.4 Modular Multilevel Converter Based HVDC (MMC-HVDC)

Despite the voltage rating of IGBTs, IGCTs and other solid-state devices have already reached 6.5 kV and keep increasing; hundreds of IGBTs need to be connected in series to reach the 500kVdc of thyristor-based LCC-HVDCs. To prevent cascading failure, it is necessary to equalize the voltages across all the IGBTs, IGCTs or GTOs, not only in steady-state but also in transients. Equalization circuits(snubbers), in parallel with IGBTs, IGCTs or GTOs, have been developed and put to use successfully by a major HVDC manufacturing company. However, the snubbers are proprietary. Competitors have not invested in developing the snubbers because they see different topologies based on Multilevel Cascaded H-Bridge (CHB)[14]-[16]. The CHB topologies significantly reduce the numbers of IGBTs connected in series and provide the DC fault blocking capability. However, the complexity of voltage balance control of the individual capacitor across each module increases with the module numbers.

In 2001, Professor R. Marquardt invented the Modular Multilevel Converter (MMC) [17]. The MMC-HVDC is the fourth generation of the HVDC. By interleaving (phase-shifted triangle carrier principle) the switching of sub-modules, the MMC-HVDC outputs quality waveforms (eliminating

harmonic filters) with significant switching losses reduction. By increasing the number of series-connected submodules, the MMC is able to extend the operating voltage to any level. With a reduction of both size and cost, the MMC-HVDC has an important role in power systems [18].

The first MMC-HVDC system was Transbay Bay Cable Project commissioned in 2010 across the bay from San Francisco to Pittsburgh [19]. The MMC-based HVDC transmission system continues to advance due to its outstanding benefits. Several MMC-HVDC projects systems have been commissioned recently, such as: the back-to-back MMC-HVDC INELFE project between France and Spain commissioned in 2015 with a voltage rating at ±320 kVdc and a total capacity of 2000 MW [20]; the Multi-Terminal MMC-HVDC project (MTDC-MMC-HVDC) commissioned in 2014 in Zhoushan with 5-Terminal, voltage rating at ±200kV and a total capacity of 1000MW [21]. Increased numbers of MMC-HVDC projects are under construction, i.e., the Four-Terminal MMC-HVDC project between Zhangbei and Beijing with a voltage rating of ±500kV and a total capacity of 3000MW, which will be put in service in 2020 [22].

1.2.2 Modular Multilevel Converters

The topology of modular multilevel converters (MMC) was first proposed by Professor Marquardt in 2001 [17]. Retaining the cascaded connections features, the MMC does not require costly phase-shift transformers or isolated DC sources. The configuration of the MMC is shown in Fig. 1-1. Sub-Modules (SM) connected in series enables the increase of voltage and power capacity. The topologies of MMCs with different kinds of SMs continue to develop in recent years. Half-bridge SMs (HBSM), Full-bridge SMs (FBSM), and Clamped Double-Cell SMs (CDSM) [23] constitute the most common SM structures, which are shown in Fig. 1-2.

The SM topology of HB-MMC, as shown in Fig. 1-2 (a), has been widely established in the market for point-to-point, back-to-back and multi-terminal HVDC systems [24]-[28]. Though HB-MMC uses the least number of semiconductors among the three structures; its drawback is that it is incapable of blocking DC faults. This limits its attraction in several DC grid applications. The SM schematic of FB-MMC, as shown in Fig. 1-2(b). The FB-MMC (Full Bridge MMC) is capable of blocking fault current and controlling the current during the DC fault. However, the number of semiconductors and the conducting time are doubled, which leads to an increase in cost and losses. Due to its outstanding performance during DC faults, the FB-MMC has been widely applied in medium voltage direct current (MVDC) applications [29]-[34]. The SM configuration of CDSM-

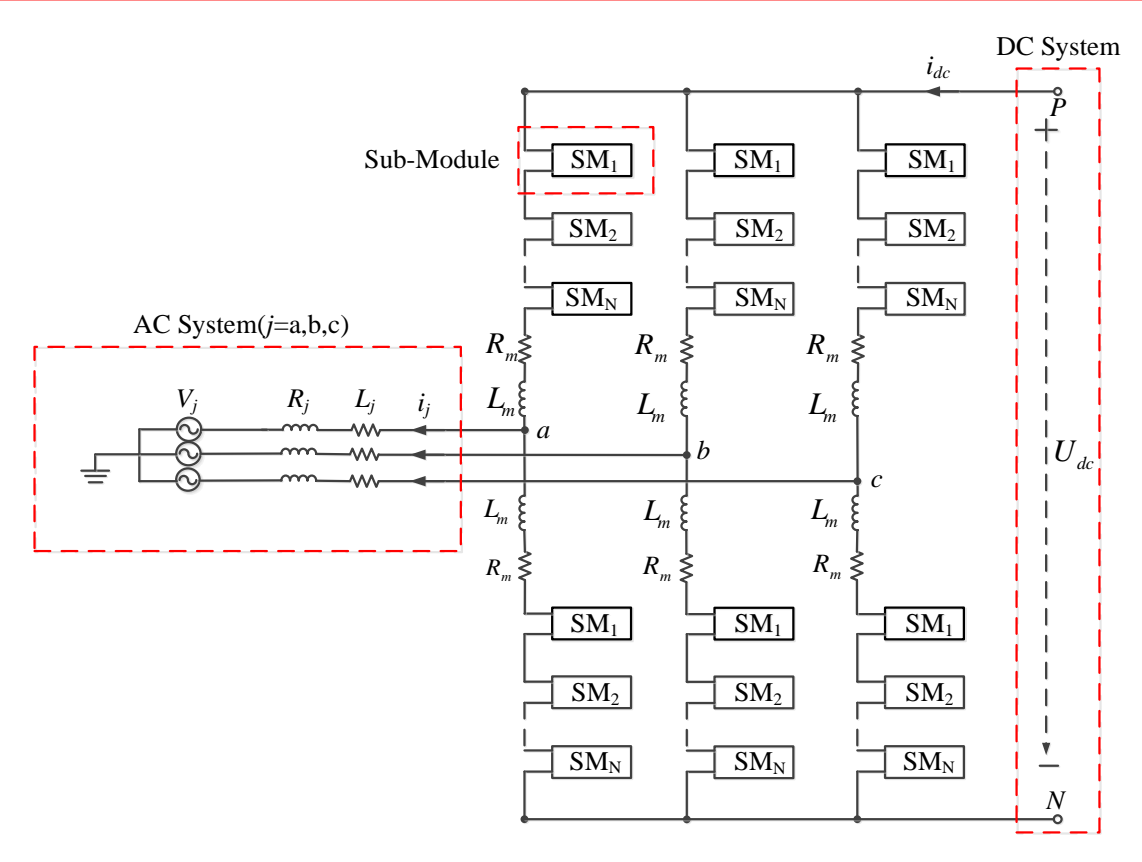


Fig. 1-1 Configuration of the MMC

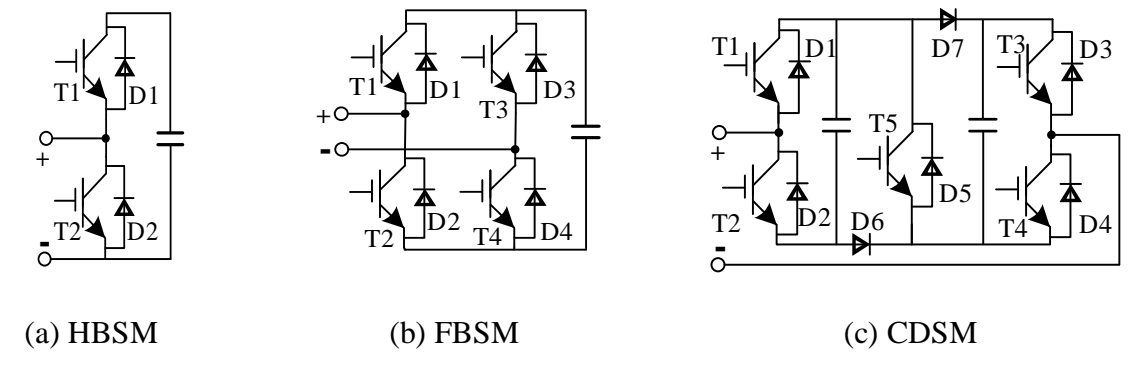


Fig. 1-2 Different topologies of the MMC Sub-Modules.

MMC is shown in Fig. 1-2(c). Consisting of two HBSMs connected in series with one IGBT and two diodes, the CDSM is capable of blocking dc fault current, but it cannot control the current during the fault. The CDSM requires fewer semiconductors and has lower losses in comparison to the FBSM.

Although the MMC has been considered as one of the most promising converter topologies in high power applications, several challenges [35]-[37] continue to be investigated. These challenges

are: 1) MMC designing constraints; 2) capacitor voltage balance methods; 3) MMC low-order circulating current suppression; 4) MMC modulation methods; 5) MMC modeling techniques; 6) MMC in grid-connected applications.

1.2.2.1 Literature on MMC Designing Constraint

To design the proper size of arm inductors and submodule capacitors is important. The arm inductors limit the short circuit current during the DC faults and filter the switching frequency harmonics in arm current. M. Hagiwara et al. [38] reduced the common mode inductance by coupling the inductance between upper and lower arm. Capacitor voltage ripple issues are severe in motor drive applications because a low or zero speed operation will introduce a significant charge and discharge of the capacitors. An obvious solution is to select large capacitors to reduce the ripples; however, large capacitors increase the cost. One feasible solution is to implement MMC matrix configurations [39] to ensure MMC normal operation at zero or low-speed conditions at a rated torque without large voltage ripples.

1.2.2.2 Literature on MMC Capacitor Voltage Balance Control

Capacitor voltage balance control is another important issue for the MMC. The capacitor voltage balance control can be divided into two categories: the centralized voltage control to balance the voltage between upper and lower arms, and the decentralized control to balance the individual capacitor voltage inside the arms [37]. The objective of the centralized voltage control is to keep the voltage of the arm equivalent capacitor equal to the reference value. In order to achieve that, the MMC input power should be equal to the output power plus the losses [40]. Voltages or energies of different arms could be balanced by controlling the current flowing in the different arms. Several methods have been investigated to mitigate the impact on input and output current by making use of common-mode voltages [41] or circulating currents [42]. In order to keep the voltage of individual capacitor equalized, the decentralized voltage control algorithm is necessary. Among them, the sorting algorithm [35] is a widely used method, which selects certain numbers of SM capacitors with the highest voltage or lowest voltage to charge or discharge depending on the directions of the arm current flow.

1.2.2.3 Literature on MMC Circulating Current Control

The circulating current, which produces voltage ripples, needs to be eliminated. The voltage ripples have twice the line frequency of the circulating currents current. The proportional-integral

(PI) controller has been used [43][44] to mitigate the double line frequency circulating current after it had been transformed from the stationary-*abc* frame to the synchronous-*dq* frame. [45]-[47] established and implemented the resonant controller to eliminate the dominant second and other higher-order harmonics from the circulating current. Other methods have been proposed for unbalanced situations, such as: the parallel combination [48] or cascade structure [49] of repetitive and PI regulators; the proportional-integral resonant regulators [50]; the ideal [51] and the nonideal [52] proportional resonant (PR) regulators.

1.2.2.4 Literature on MMC Modulation Techniques

The Pulse-Width-Modulation (PWM) techniques, widely used in VSCs [53][56], have been modified and applied to MMCs [57][58]. Based on the switching frequency f_{sw} , the PWM techniques for the MMC are divided into three categories: high-frequency modulation (f_{sw} >2000Hz), medium-frequency modulation (100Hz< f_{sw} <2000Hz) and low-frequency modulation. The low-frequency modulation is also called fundamental-frequency modulation [37].

High-frequency modulation techniques include the phase shifting carrier-based modulation (PS-PWM) [59] and the level shifting carrier-based modulation (LS-PWM) [60]-[62]. The gating signals of PS-PWM and LS-PWM are generated by comparing these to horizontal and vertical multiple carriers, and to the phase modulation signals, respectively. Although the implementation of the PS-PWM and the LS-PWM are simple, the high switching losses limit their application in high power converters.

The sampled average modulation (SAM) [63] and the space vector modulation (SVM) [64] are two main techniques within medium-frequency modulation. The principle of SAMs and SVMs are similar. The SVM controls the line-to-line voltage of an MMC directly, while the SAM controls the phase voltage instead. Although the SAM algorithm is easy to implement in the MMC with any SMs numbers, its unequal distributed zero vectors in switching sequence introduce a high distortion in output voltages. On the other hand, it is hard and complicated to implement the SVM in MMCs with a large number of SMs (*N*>10).

The popular low-frequency modulation technique or the fundamental modulation technique is the staircase modulation or Nearest-Level modulation (NLM) [65][66]. In order to reduce the switching losses, the converter with NLM is switched at fundamental frequency. This leads to a high distortion output voltage and current for MMCs, which have a small number of SMs.

However, in MMC-HVDC application, hundreds of SMs are connected in each arm. The large number of SMs significantly reduces the total harmonic distortion (THD) to less than 1%. Moreover, the NLM is easy and simple to extend for the MMC with different SMs numbers. Because it has low switching loss, small THD and because it is a simple algorithm, the NLM method is the most widely used modulation method in MMC-HVDC application.

1.2.2.5 Literature on MMC Modeling Techniques

Various types of MMC computational models have been proposed in recent years [67]-[85]. Depending on the application, these models are classified into seven types [67]: Type 1-Full Physics Models (PM) [68]-[69]; Type 2-Full Detail Models (DM) [70][71]; Type 3-Models based on switchable resistance (SRM); Type 4- Detail Equivalent Circuit Model (DEM) [72]-[77]; Type 5-Average Value Models based on switching functions (AVM) [72]-[80]; Type 6-Simplified Average Value Models (SAVM) [81]-[84]; Type 7- Load-Flow Models (LFM).

For Type 1-PM, called either differential equations or equivalent circuits, are used to model every single diode and solid-state switch. Since the computation time is very large, Type1 is typically used for simulation of a sub-system, for example, to investigate the dynamics of single SMs. Type 1 is not used for simulation at the converter level or at the grid application level [67]. With the advent of the Graphics Processor Unit (GPU), its massively parallel architecture enables Type 1 to be employed. Recently, an MMC-MTDC system based on the exact nonlinear MMC model was successfully implemented in the GPU [68][69]. However, the GPU is not compatible with most power simulation software, and to implement the algorithms to the GPU is complicated.

Unlike Type 1-PM, the IGBT model in Type 2-DM is simplified to an ideal controlled switch with two non-ideal diodes, which are modeled as nonlinear resistances. Type 2 is typically used for the validation of simplified models and the investigation of abnormal SM actions. Due to the nonlinearity characters of diodes, it is extremely time-consuming to simulate Type 2 on computers or on CPU. Recently, through the piecewise linearization of the behavior of IGBTs and diodes, the Type 2 MMC model has been implemented to a field-programmable gate array (FPGA) for variable-speed drive application [70] and the GPU for variable time-stepping model application in MTDC systems [71].

Similar to Type 2-DM, Type 3-SRM is obtained by further simplifying the IGBTs and diodes into switchable two-value resistors R_{on} and R_{off} , neglecting the transient states. Type 3 is also used

for the validation of simplified models, and for the investigation of abnormal SM actions. Although Type 3-SRM is significantly faster than Type 2, solving large numbers of electrical nodes still takes a long simulation time. For a better computation time, Type 3-SRM requires a solver algorithm to deal with the rapid nonlinear switching.

Type 4-DEM is based on the SRM, but uses a more computationally efficient method. In order to obtain a simple circuit while maintaining the model's accuracy, the internal electrical nodes are eliminated, and a Thevenin equivalent circuit is obtained. The Thevenin equivalent circuit increases simulation speed significantly [72]-[74]. Type 4-DEM is mainly used for investigating the Electromagnetic Transient Process (EMTP) and for designing the low-level controls, e.g., voltage balancing controls [86]-[87]. Since the simulation equations for each SM are calculated separately, Type 4-DEMs are employed in multiple-parallel CPUs for real-time implementation [75]-[77].

To further simplify the model to investigate transient studies on AC grids and design high-level control systems, the proposed Type 5-AVM neglects details regarding switching, and uses controlled voltage and current sources with the harmonic components to model DC and AC dynamics. It assumes that the voltages of capacitors in each SM are equality distributed [72]-[73]. Type 5-AVM is used to investigate transients on AC grids and to design high-level control systems.

It should be pointed out that all simulations are based on numerical integration of the ordinary differential equation of an inductor or a capacitor. There are as many as a hundred sub-modules in one arm of one MMC phase. Each sub-module has a capacitor C. Detail simulation is slow because hundreds of ordinary differential equations of the capacitors C have to be numerically integrated. Recently, the formulation based on the ordinary differential equations (ODE) of [78] has increased the simulation speed significantly. The ODE of [78] treats each arm of the n(t) series-connected SM as having an equivalent capacitor of size C/n(t). The method based on the ordinary differential equations (ODE) of [78] has only 12 equations to integrate numerically. (Each phase has one equation for the upper arm of the equivalent capacitor $C/n_U(t)$, and one equation for the lower arm of the equivalent capacitor $C/n_U(t)$. One KVL equation of the AC-side and one KVL of the dc-side). Further speed increase, which comes from the coarser integration step-size, can be used [79]-[80].

Type 6-SAVM is also called as the Phasor Model, the fundamental frequency model, or electro-mechanical models. By assuming that all harmonics are neglected and an ideal sinusoidal

output is produced, the controlled voltage and current sources are represented in the phasor domain to model DC and AC dynamics. This type of model is mainly applied for medium-term (400ms to 10s) and long-term (10s to several mins) studies, including transient and voltage stability, long-term stability and daily load evolutions [67]. The first MMC dynamic PM is proposed in [81]. Several improved PM models are proposed considering the following aspects: second-order terms with Circulating Current Suppression Control (CCSC) [82]; dominant harmonic components with extended frequency range [83]; shifted PM in Real-Time implementation [84].

Type 7-LFM is mainly used for power flow studies in large hybrid AC/DC systems, including normal system conditions and contingency system conditions. Similar to Type 6-SAVM, harmonics are ignored, and an ideal sinusoidal output is assumed. Therefore Type 7-LFM cannot be applied to converter controller design, harmonics analysis or internal investigations of MMC.

1.2.3 Power Oscillation of Damping (POD)

Power System Stabilizers (PSS) [88] were proposed in the early 1960s to maintain the stability of power grids. At the level of an individual generator, stability centers around excitation system tuning [89]. As power systems grew in size, oscillatory modes in the lower frequency range of 0.01–0.08 Hz are encountered. Poor damping in modal oscillations of wide-area systems is investigated through the eigenvalues of linearized [A]-matrix [90]. The low frequencies are beyond the frequency range of the existing PSS design [91].

Although there are several variations of the classical PSS [92], the basic structure remains the same. The input is frequency deviation $\Delta \omega_r$ measured by a speed transducer on the rotor. The output is the current of the field winding of the generator. Between the input and the output are Lead-Lag blocks and a Washout block.

To cope with the extended frequency range reported in [91], the multi-band approach is explored in [93][94].

1.2.3.1 Literature of POD by Power Electronic Controllers

Because controllers of the HVDC and the Flexible AC Transmission Systems (FACTS) [95] do not have information of frequency deviation $\Delta \omega_r$ measured from speed transducers of the generators' rotors of the power system, measurements have to be taken from the AC voltage terminals of the HVDC or the FACTS station.

Taking Mercury Arc Technology to be the 1st generation of HVDC, the LCC thyristor HVDC of the 2nd generation made use of terminal voltage measurements to suppress a negatively damped 1/3 Hz oscillation in Pacific AC Intertie [96]. This stabilization allowed the rating of Pacific AC Intertie to increase from 2100 MW to 2500 MW. An analysis of the controls is given in [97]. Research of the Pacific AC Intertie continues, for example, in multi-terminal subsystem validation [98].

Advancing to the 3rd generation of 2-level VSC, the major reference is [99]. From sample publications, applications of power oscillation damping include: wind farms [100]-[104], wide area control (WAC) [105]-[108], sub-synchronous resonance instability (SSR) [109]-[112], and Flexible AC Transmission Systems (FACTS) [113][114]. Selected control methodologies for WAC are treated in [115][116].

Moving on to the recent 4th generation of IGBT-based modular multilevel converters (MMC), research in power oscillation damping is pioneered in [117]-[121].

1.2.3.2 Literature of POD Control in Classical Power System Stabilizer (PSS)

Power oscillation damping control of the 2^{nd} , 3^{rd} and 4^{th} generations is adapted from the classical PSS of generators [92]. But in most cases, there is no rotor to measure frequency deviation $\Delta \omega_r$. Although there is no long-time delay of the field winding, many researchers continue to retain Lead-Lag blocks [100]-[108]. Analysis of Pacific DC Intertie [97] states that a differentiator is required for the damping.

As there is no guidance as to how damping is achieved for HVDC stations, Section II presents an analysis showing that damping power must be proportional to the derivative of voltage angle δ , which is $d\delta/dt$. Time differentiation is, from a theoretical viewpoint, not realizable. Numerical derivatives introduce noise, which requires filtering by a low-pass filter. As low pass filtering consists of integration, it requires skillful design to avoid nullifying the numerical derivative.

1.2.3.3 Literature of POD using Phase-Locked Loop (PLL)

Heeding frequently repeated warnings to avoid differentiation, the paper turns to the phase-locked loop (PLL) [122]-[130]. HVDC experts are already familiar with the 3-phase phase-locked loop (PLL) because it was first introduced to the HVDC in [131]. Engineers, who use the decoupled P-

Q control, have already applied the PLL to measure the voltage angle θ to transform the a-b-c to the d-q reference frame. The PLL is also used in the HVDC to maintain synchronization with weak AC transmission [132].

1.2.4 Damping Sensitivity to Parameters

As the author is treading new ground in exploring how damping of MMC HVDC is affected by the choice of the sizes of capacitor, inductance, resistance and other parameters the prior references are limited [133]-[136].

1.3 Problem Statement

The MMC HVDC is now a favoured hardware choice for HVDC applications because it is economical and efficient. However, there remain 3 issues which are addressed in the thesis. The first issue is how to analyze the stability of the MMC. Secondly, to investigate the capability of MMC-HVDC to increase the stability to the powers system by operating as a power system stabilizer (PSS) to damp power oscillation. With the integration of renewable energy technologies (especially offshore wind farms), and with the capability of the MMC-HVDC to be connected in parallel with the DC-side as Multi-Terminal MMC-HVDC (MTDC-MMC-HVDC), power system engineers require software for planning, operations and protection studies.

The thesis undertakes to address the challenges by providing the following:

- i. A fast and accurate simulation model for a single MMC station and the MTDC system.
- ii. An analytical method to design parameters to improve the stability of the MMC.
- iii. The MMC with the capability to damp the power oscillation and increase the transient stability for AC grid.

1.4 Objectives and Contributions

This thesis is focused on the modeling and stability analysis techniques of MMC and its control strategies. The main objectives of this thesis are listed as follows:

- i. To develop a fast and accurate analytical model for single MMC stations and MTDC systems.
- ii. To use the proposed model to improve stability and damping.
- iii. To design a control strategy for MMC-HVDC to damp power oscillation and improve the transient stability of connected AC grids.

This thesis developed the model proposed in [78] to form a fast and accurate analytical simulation model of MMC based on Ordinary Differential Equations (ODE). Aprille and Trick method [133] and Lyapunov-Floquet Theorem [135] are studied and applied to the proposed ODEs Model for steady-state investigation and stability analysis. The proposed ODEs model is extended to a four-terminal HVDC system with stochastic wind farm connection. The four-terminal system will be used for future studies on hybrid AC/DC grids with renewable energy integrations. In addition to the developed MMC models, a universal control strategy including the POD control, the decoupled PQ control, the deadbeat control, the second-order circulating current control, is proposed for MMC which is integrated into two-bus one generator systems.

The original contributions of this thesis are summarized as follows:

- A fast and accurate analytical model based on the ODE is developed for a single MMC station and extended to MTDC systems. The proposed models are evaluated and validated by the Detail Equivalent Model (DEM) in RT-LAB.
- ii. By linearizing and manipulating the proposed MMC model, the Aprille and Trick method is applied for fast convergence to the steady-state of MMC. The Floquet-Lyapunov Theorem is applied to compute the damping coefficients of MMC transients.
- iii. Innovative application of the phase-locked loop (PLL) to extract the frequency and the phase angle from electrical signals at the AC-terminals is proposed and investigated. Simulation results show that MMC HVDC can provide POD by applying the extracted signal of the PLL.
- iv. A universal control has been proposed including the POD control, the decoupled PQ control, the deadbeat control and the CCSC. The deadbeat control enables MMC to survive destructively large AC fault currents to improve the transient stability of AC grids.

1.5 Methodology

The methodology consists of two parts: (1) mathematic analysis; (2) simulation tools.

1.5.1 Mathematic Analysis

The author follows the original algebraic MMC model proposed in [78] to develop the ODEs and equivalent circuits of MMC for both the DC and the AC sides. The ODEs model of MMC-HVDC station is obtained and extended to a Multi-Terminal MMC HVDC system.

The challenge in MMC research is to find a systematic approach to design a fast response with high damping. The algebraic equations are nonlinear. Normally, the answer is found through linearized equations. Small perturbation linearization requires the steady-state to be solved first. Numerical integration requires the transients to be damped out leaving the steady-state. To avoid the long wait for transients to subside, the Aprille and Trick method [133] is applied. The limit cycle is reached within one cycle of 50 or 60 Hz. The linearized equations are characterized by the periodic matrix [A(t)]=[A(t+T)] where T is the period of 50 or 60 Hz. The Floquet-Lyapunov Theorem is found to be the entry point to the development of a method by which the size of circuit parameters, such as resistances, inductances and capacitors are chosen in order to arrive at a good damping.

Further analysis shows that the nonlinearity is classified as bilinear, and that the state-variables are multiplied by the forcing function. Because of the bilinearity, dynamic characteristics of small disturbances apply to large disturbances.

Poor damping does not come from a poor choice in parameter sizes only. The MMC-HVDC station encounters power oscillation from the AC grid. The research tackles this external problem by measuring the oscillations at the point-of-common coupling and using the signal as feedback so that the MMC-HVDC station produces active power to damp the power oscillations. The signal is extracted from a phase-locked loop (PLL).

1.5.2 Simulation Tools

Two tools are used in this thesis. The proposed ODEs models and corresponding control strategies are simulated in MATLAB/SIMULINK. The second tool is RT-LAB, which is a real-time simulation software developed by OPAL-RT. RT-LAB offers the most complex model-based design [137].

1.6 Thesis Outline

Chapter 2 presents a brief introduction of 3-phase modular multilevel converters. Configurations, operation principles and the nearest level modulation technique are discussed. The equivalent circuit for both AC and DC sides are developed through the circuit analysis.

Chapter 3 presents the MMC model derived from ordinary differential equations. The circulating current suppression control is discussed. The dynamic performance of the proposed ODE MMC model is compared and validated by the Detailed Equivalent Model (DEM).

Chapter 4 introduces two useful techniques applied to the MMC. The first one is the method of Aprille and Trick by which the steady-state is solved within one period of 50 or 60 Hz, without having to wait for transients to be damped out. The second one is the Floquet-Lyapunov Theorem by which graphs of the damping coefficients of transients are computed to guide system designers in choosing the best size of circuit parameters. The steady-state and stability analysis are studied and discussed.

Chapter 5 presents a Multi-Terminal MMC-HVDC system (4 terminals). It exemplifies the accurate and fast digital simulation platform, which power system engineers want for design, operation and planning studies on the large hybrid (AC-DC) grids in the foreseeable future. The steady-state and dynamic performance of the ODE model of the MTDC-MMC system are compared and validated through the DEM of the MTDC-MMC system.

Chapter 6 presents the capability of MMC HVDC to provide Power Oscillation Damping (POD). Small signal analysis is applied to confirm that the requisite power to implement POD is proportional to $d\delta/dt$, where δ is the voltage angle. An innovative passive local control method is proposed based on a three-phase, phase-locked loop (PLL) which measures the signal $d\delta/dt$ without differentiation. The damping provided by MMC-HVDC is applied to increase the transient stability limit and thereby increase the active power transmissibility of the AC transmission lines. A Universal Control Strategy is proposed. The Universal Controller includes the POD control, the decoupled PQ control, the second-order circulating current control, and the reference current control deadbeat to protect MMC from AC side short circuit faults. The Universal Controller is, in fact, functioning because the controls of the MMC-HVDC are fitted with the Universal Controller in the simulation tests in this chapter.

Chapter 7 summarizes the main conclusions of the thesis and addresses future work.

Chapter 2. Modular Multilevel Converters

2.1 Introduction

High-voltage direct current (HVDC) is more efficient and economical than high-voltage alternating current (HVAC) in long-distance, bulk power transmission systems. Because it has desirable features (modularity, flexibility, reliability and high efficiency), the modular multilevel converter (MMC) is the most attractive converter topology.

This chapter first introduces the basic configuration of a 3-phase MMC system made up of the half-bridge sub-module (HBSM) connected in series in the upper arm and the lower arm of each of the three phases. The basic operation principle of the HBSM-MMC is described. The widely used modulation technique in the MMC-HVDC, the Nearest-Level Modulation (NLM), is briefly explained. The equivalent circuit for both the AC and DC side of MMC is obtained from the circuit theory.

2.2 MMC Topologies

The topology of modular multilevel converters (MMC) was first proposed by professor Marquardt in 2001 [17]. The basic schematic of MMC is shown in Fig. 1-1 in Chapter 1. Sub-Modules (SMs) connected in series enable the voltage and power to be increased. Some topologies of MMC being developed are shown in Fig. 1-1 in chapter 1, and they include: the Half-bridge SM (HBSM), the Full-bridge SM (FBSM) and the Clamped Double-Cell Sub-Module (CDSM) [23]. Although the topologies of the FBSM and the CDSM are briefly discussed in this chapter, only the HBSM-based MMC is studied throughout this thesis. Therefore, SM refers to HBSM hereafter in the thesis.

The configuration of the 3-phase MMC, including the detailed internal structure of the HBSM, is shown in Fig. 2-1. An MMC is composed of three phases and each phase includes two arms, the

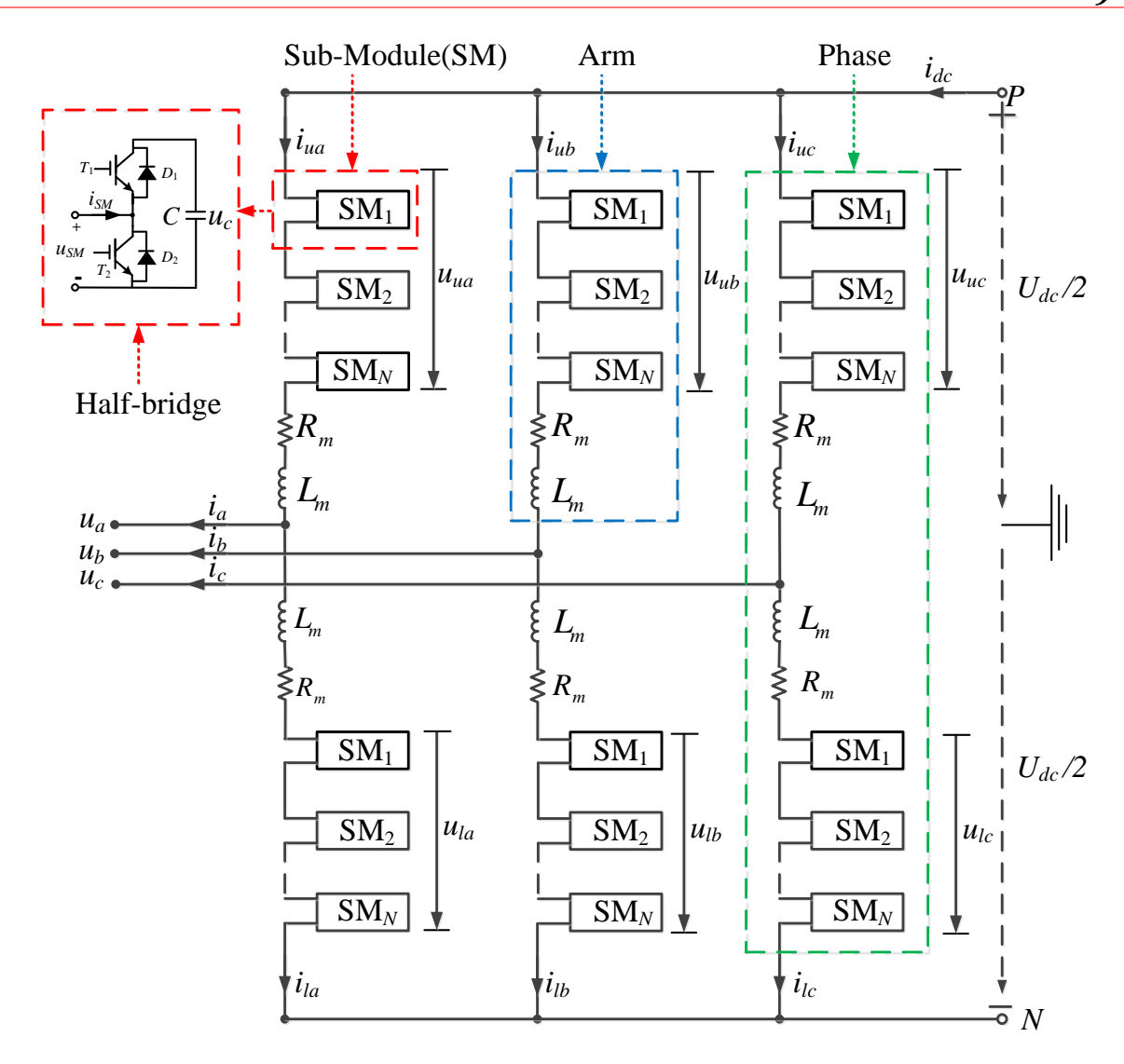


Fig. 2-1 Schematic of the 3-phase HBSM-MMC.

upper arm and the lower arm. Each arm includes N identical SMs connected in series with one arm inductor L_m and one equivalent resistor Rm, which presents the losses of SMs. The arm inductor L_m facilitates suppression of circulating current and limits the AC/DC fault current. In Fig. 2-1, i_{dc} is the DC-link current. Both the voltage between the positive pole to the ground and the ground to the negative pole are $U_{dc}/2$. The total dc voltage between the positive and negative poles is U_{dc} . The symbols u_j and i_j (j=a,b,c) represent the output three-phase voltages and currents respectively. Taking phase-a as an example, i_{ua} represents for the current in the upper arm while i_{la} represents for the current in the lower arm. u_{ua} stands for the total SMs' capacitor voltages inserted in the upper arm and u_{la} stands for the total SMs' capacitor voltages inserted in the lower arm.

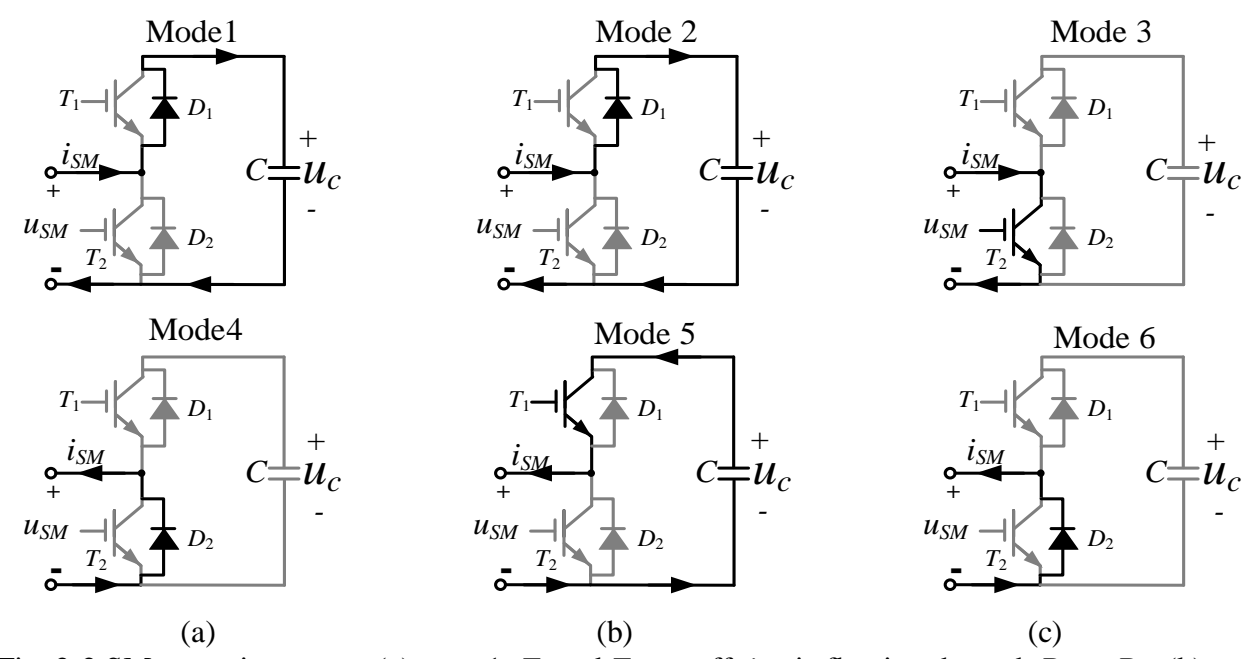


Fig. 2-2 SM operation states: (a) state 1: T_1 and T_2 are off, i_{SM} is flowing through D_1 or D_2 ; (b) state 2: T_1 is on, T_2 is off, i_{SM} is flowing through T_1 or D_1 ; (c) state 3: T_1 is off, T_2 is on, t_{SM} is flowing through T_2 or D_2

To withstand the same DC voltage, HBSM is the most economical structure comparing to the FBSM and the CDSM, because it includes the least number of IGBTs, which makes it the favourable choice with regard to HVDC applications. Each HBSM consists of two IGBTs (T_1 and T_2), which are connected in series. Two freewheeling diodes D_1 and D_2 are connected in antiparallel with T_1 and T_2 , respectively. A capacitor C is connected across T_1 and T_2 . The voltage across C is defined as u_c . u_{SM} stands for the output voltage of each individual SM and i_{SM} stands for its current. By controlling T_1 and T_2 alternately, each individual SM has six different modes as shown in Fig. 2-2.

Based on the current flowing directions and gate signals, the six operating modes could be divided into 3 states. To better explain the operation states, the positive direction of the SM current i_{SM} is defined as flowing into the SM from '+' to '-', and as negative as the reverse direction as shown in Fig. 2-2.

State 1 is shown in Fig. 2-2 (a). It includes Mode 1 and Mode 4. In this state, T_1 and T_2 are applied with turn-off signals and both of them are off. When i_{SM} is positive, the SM operates in Mode 1. i_{SM} flows through the anti-parallel diode D_1 and charges the capacitor C. D_2 is reverse-biased. Therefore, u_C increases, and the output voltage of SM u_{SM} equals u_C .

When i_{SM} is negative, the SM operates in Mode 4; i_{SM} is flowing through the anti-parallel diode D_2 and the capacitor C is bypassed. Therefore, u_C remains the same value and the output voltage of SM u_{SM} is equal to zero, neglecting the forward voltage drop on D_2 .

State 1 is also named as the block state. The blocking state can only be applied in the precharge process, or during the DC-fault protection. In the pre-charge process, both T_1 and T_2 are switched off, and the capacitors are charging through the an-parallel diodes. During the DC-fault protection process, both T_1 and T_2 are required to be turned off in order to block the fault current and bypass the capacitors in a cooperative operation with the DC breaker. During the normal operations, the block state should be precluded in order to avoid abnormal states.

State 2 is presented in Fig. 2-2 (b). It consists of Mode 2 and Mode 5. While in this state, T_1 is applied with a turn-on signal, and T_2 is applied with a turn-off signal. Both T_2 and D_2 are off. i_{SM} flows through T_1 or D_1 , depending on the current directions. When i_{SM} is positive, the SM operates in Mode 2. i_{SM} is flowing through the anti-parallel diode D_1 and charging the capacitor C.

When i_{SM} is negative, the SM operates in Mode 5; i_{SM} is flowing through T_1 and discharging the capacitor C. D_1 is blocked by an applied reverse-biased voltage. In this case, u_C decreases and the output voltage of SM u_{SM} is still equal to u_c . State 2 is also called as 'on state' or 'insert state'.

State 3 is presented in Fig. 2-2 (c). It includes Mode 3 and Mode 6. During this state, T_1 is applied with a turn-off signal and T_2 is applied with a turn-on signal. Both T_1 and D_1 are off. i_{SM} flows through T_2 or D_2 , depending on the current directions. When i_{SM} is positive, the SM operates in Mode 3. i_{SM} is flowing through T_2 and bypassing the capacitor C. D_1 is blocked by an applied reverse-biased voltage. Therefore, u_C remains the same value, and the output voltage of SM u_{SM} equals zero.

When i_{SM} is negative, the SM operates as illustrated in Mode 6. i_{SM} is flowing through the antiparallel diode D_2 and bypassing the capacitor C. Although T_2 is applied with a turn-on signal, the applied reverse-biased voltage keep it turned off. In this situation, u_C decreases and the output voltage of SM u_{SM} is equal to zero. State 3 is also called as 'off state' or 'bypass state'.

Therefore, state 2 (on state) and state 3 (off state) are the two operating states during the MMC's normal operations. The details of the above three states are summarized in Table 2-I. In the table, '1' represents a turn-on gate signal is applied and '0' refers to a turn-off gate signal.

State	Gate Signal		On/Off						
	T_1	T_2	T_1	T_1 T_2 D_1 D_2		D_2	$l_{ m SM}$	$u_{\rm C}$	$u_{\rm SM}$
Block	0	0	off	off	on	off	$i_{\rm SM} > 0$	charge	$u_{\rm SM}=u_{\rm C}$
			off	off	off	on	$i_{\rm SM}$ < 0	bypass	$u_{SM=}0$
Insert/on	1	0	off	off	on	off	$i_{\rm SM} > 0$	charge	$u_{\text{SM}}=u_{\text{C}}$
IIISCI (/ OII	1	U	on	off	off	off	$i_{\rm SM}$ < 0	discharge	$u_{\text{SM}}=u_{\text{C}}$
Bypass/off	0	1	off	on	off	off	$i_{\rm SM} > 0$	bypass	$u_{SM=}0$
		1	off	off	off	on	$i_{\rm SM}$ < 0	bypass	$u_{SM=}0$

Regardless of the gate signals and current flow directions, only one component is allowed to conduct during each state. When the gate signal of T_1 and T_2 are 0, the SM is blocked and uncontrollable. When the gate signal of T_1 is 1 and T_2 is 0, the SM is inserted in the arm. The capacitor voltage is either charging or discharging, based on the current flow directions. When the gate signal of T_1 is 0, and the one of T_2 is 1, the SM is bypassed in the arm. During the normal operation of the MMC, and by controlling the gate signals of T_1 and T_2 , each SM is either inserted or bypassed in the six arms to generate the arm voltages u_{ij} and u_{ij} (j=a,b,c) so to produce the required 3-phase output voltages u_i (j=a,b,c), as shown in Fig 2-1.

2.3 MMC Operation Principle

2.3.1 Operation Principle

The basic principle of MMC operation is to generate a series of gate signals to insert an SM or bypass an SM to join a series string of capacitors, which constitutes the upper arm or the lower arm of one phase. The objective is to generate 3-phase AC voltages which meet the total harmonic distortion (THD) requirement from the voltages across the string of capacitors.

In order to illustrate the operation principle, the N submodule configuration of Fig. 2-1 is reduced to a five-level configuration in Fig. 2-3. Each arm of the five-level MMC is composed of six SMs, which can be connected in series by "inserted" or "bypassed" by switching the IGBTs. In Fig. 2-3, u_C represents for the balanced capacitor voltage in each SM, and U_{dc} denotes the pole to pole DC voltage. u_{uj} (j=a,b,c) is the total capacitor voltage inserted in the upper arm of phase-j, and u_{lj} (j=a,b,c) corresponds to the total capacitor voltage inserted in the lower arm of phase-j. The three-phase output AC voltage is u_i (j=a,b,c) generated by u_{uj} and u_{lj} .

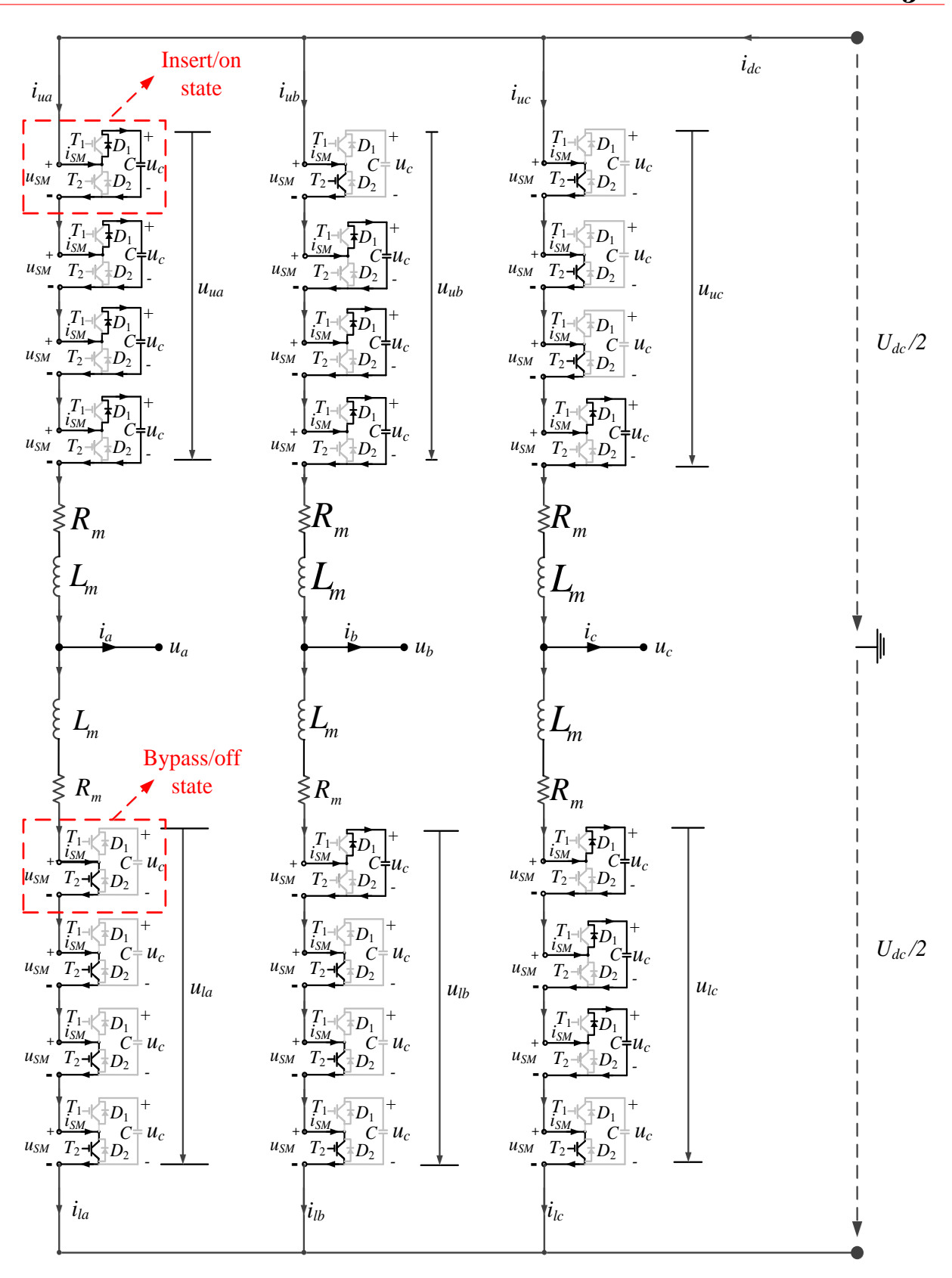


Fig. 2-3 Illustration of the operation of a five-level MMC.

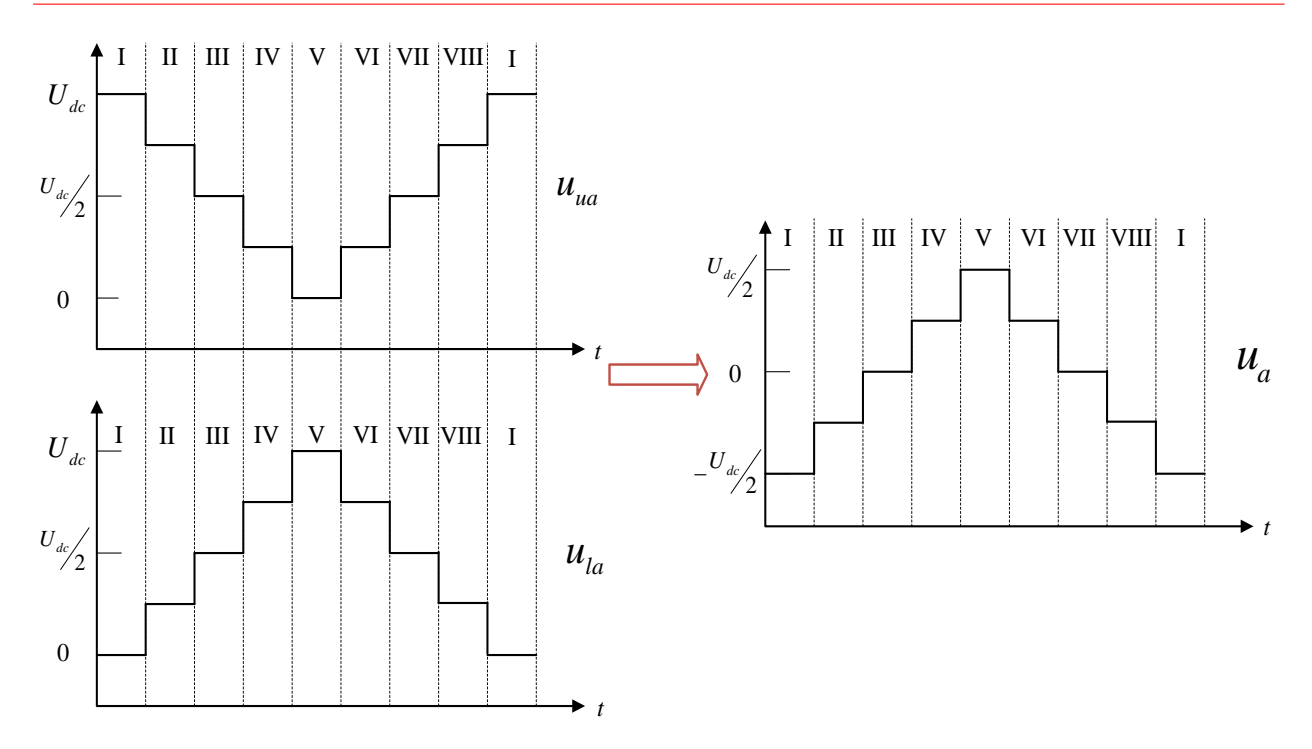


Fig. 2-4 Illustration of the phase-a operation of the 5-level MMC.

Since the operation principle of the phase-b and the phase-c are the same as the phase-a, except for a 120-degree phase-shift, only the waveforms of u_{ua} , u_{la} and u_a in Fig. 2-3 are presented in Fig. 2-4. In Fig. 2-4, a full cycle of 50 Hz is divided into eight time divisions (I, II, III,... VII, VIII). A coarse representation of the sinusoidal output voltages is shown in Fig. 2-4.

In section I of Fig. 2-4, all SMs in the upper arm are inserted (on state) in the arm while all SMs in the lower arm are bypassed (off state) in the arm. The 'on state' and 'off state' are displayed in the phase-a of Fig. 2-3. Based on the circuit theory, the AC terminal voltage u_a is $-U_{dc}/2$. The detail operation information of the eight subsections and the generated output voltages are summarized in Table 2-II.

The results in Fig.2-4 and Table 2-II clearly show that an MMC with four SMs in each arm will produce a five-level output voltage on the AC side. A more general conclusion is that for an MMC with N SMs connected in each arm will generate an N+1-level AC voltage, where N is the total number of SMs connected in one arm. Therefore, N 'on state' or inserted SMs produce the DC voltage $U_{\rm dc}$, that is,

$$U_{dc} = N \times u_c \tag{2-1}$$

The quality of the output AC voltage $u_i(j=a,b,c)$ will improve if N increases.

Table 2-II Phase-*a* operation sequence of the upper arm and lower arm SMs.

	Subsections							
	I	II	III	IV	V	VI	VII	VIII
Number of on state SMs in the upper arm n_{ua}	4	3	2	1	0	1	2	3
Number of on state SMs in the lower arm n_{la}	0	1	2	3	4	3	2	1
Number of on state SMs in one phase	4	4	4	4	4	4	4	4
Upper arm inserted voltage u_{ua}	U_{dc}	$\frac{3}{4}U_{dc}$	$\frac{1}{2}U_{dc}$	$rac{1}{4}U_{dc}$	0	$rac{1}{4}U_{dc}$	$\frac{1}{2}U_{dc}$	$\frac{3}{4}U_{dc}$
Lower arm inserted voltage u_{la}	0	$\frac{1}{4}U_{dc}$	$\frac{1}{2}U_{dc}$	$\frac{3}{4}U_{dc}$	U_{dc}	$\frac{3}{4}U_{dc}$	$\frac{1}{2}U_{dc}$	$\frac{1}{4}U_{dc}$
Output voltage u_a	$-\frac{1}{2}U_{dc}$	$-\frac{1}{4}U_{dc}$	0	$\frac{1}{4}U_{dc}$	$\frac{1}{2}U_{dc}$	$\frac{1}{4}U_{dc}$	0	$-\frac{1}{4}U_{dc}$
DC bus voltage	U_{dc}	U_{dc}	U_{dc}	U_{dc}	U_{dc}	U_{dc}	U_{dc}	U_{dc}

To ensure that the MMC works in the normal state, a constant DC voltage on the DC side should be maintained. Taking phase-a as an example, in order to generate a constant DC bus voltage, the total SMs inserted, or the in 'on state' in phase-a has to be equal to N, shown in (2-2):

$$n_{ua} + n_{la} = N \tag{2-2}$$

where n_{ua} and n_{la} denote the total number of SMs inserted in the upper arm and the lower arm of phase-a, respectively.

Substituting(2-1) into (2-2), we have

$$u_c = \frac{U_{dc}}{N} = \frac{U_{dc}}{n_{ua} + n_{la}} \tag{2-3}$$

Based on (2-3), a Nearest-Level-Modulation (NLM) is proposed, which the subsequent section discusses.

2.3.2 Nearest Level Modulation (NLM) Method

The Pulse Width Modulation (PWM) and the Staircase Modulation are two common modulation methods for different MMC applications [138]. The Nearest Level Modulation (NLM) is one

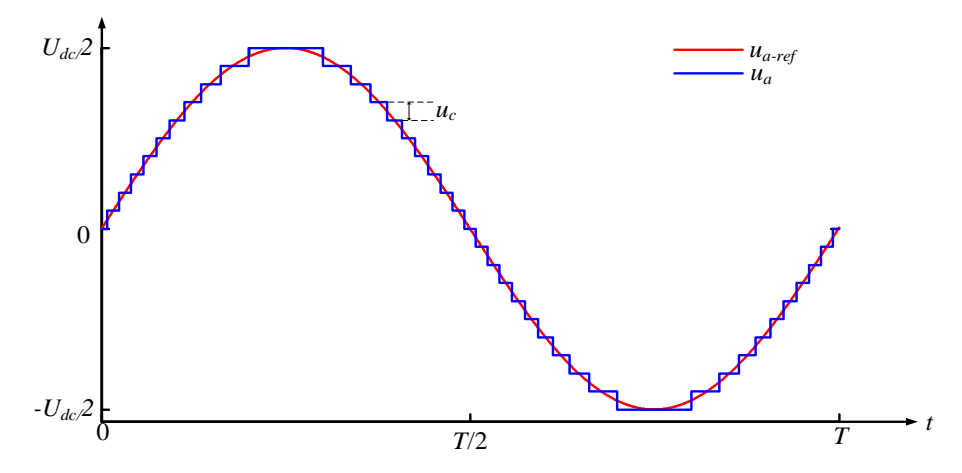


Fig. 2-5 Operation principle of the NLM method.

popular method of the Staircase Modulation. It is preferred in HVDC applications because the converter with the NLM is switched at the fundamental frequency, thus reducing the switching loss significantly. The quality of the output waveform of the NLM is poor if the level number is small. However, in HVDC applications, the total harmonic distortion (THD) of the generated three-phase output voltage is less than 1% since hundreds of SMs are connected in each arm. In addition, the NLM method is easy and simple to extend for the MMC with different SMs number. With low switching loss, a small THD and a simple algorithm, the NLM method is the most widely used modulation approach in MMC-HVDC applications.

The detail operation process of the NLM is illustrated in Fig. 2-5. Taking Fig. 2-5 to represent the phase-a as an example, phase-b and phase-c are similar, except for phase shifts of -120 and -240 degrees, respectively. The red curve $u_{a\text{-ref}}$ in Fig. 2-5 is the reference signal of phase-a, which is decided by control objectives, i.e., active power, reactive power and DC voltage. The blue staircase curve u_a represents outcome of Nearest Level Modulation (NLM) Method. During each cycle T, that is 0.02s corresponding to a 50Hz line frequency, each SM will be inserted or bypassed only once. By inserting or bypassing one SM each time, the output voltage will either increase or decrease by u_c , which is the capacitor voltage of one SM.

Because the IGBT switching inserts or bypasses one SM at a time, the switching loss is low. The number of the SMs instantaneously inserted or bypassed in the upper arm and lower arm are as follows:

$$n_{ua} = \frac{N}{2} - round(\frac{u_{a-ref}}{u})$$
 (2-4)

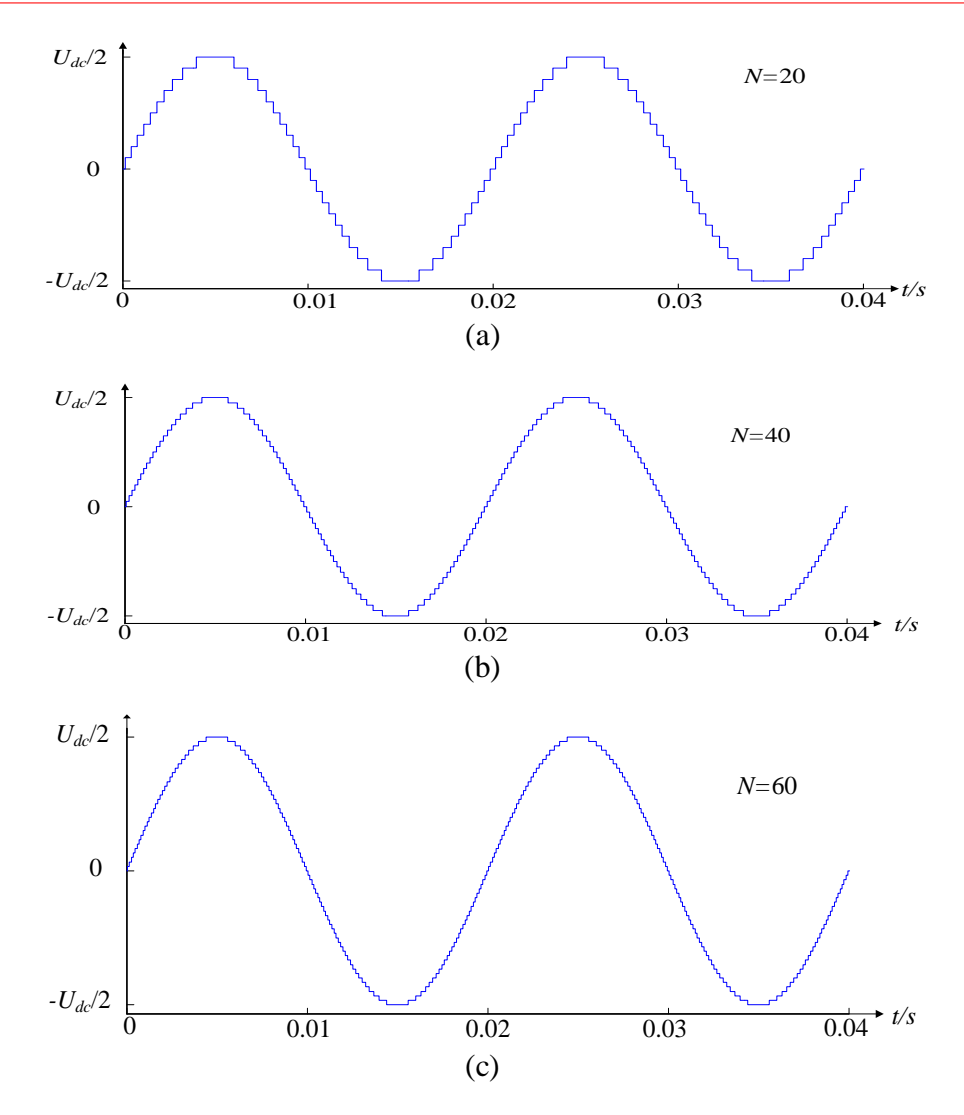


Fig. 2-6 Output voltage of the MMC phase-a: (a) 21-level; (b) 41-level; (c) 61-level

$$n_{la} = \frac{N}{2} + round(\frac{u_{a-ref}}{u_c})$$
 (2-5)

where *N* is the total number of the SMs connected in each arm, and round $\left(\frac{u_{a\text{-ref}}}{u_c}\right)$ presents the nearest integer around $\frac{u_{a\text{-ref}}}{u_c}$.

The reference voltage of the phase-a is

$$u_{a-ref} = \frac{1}{2} m_a U_{dc} \cos(\omega t + \varphi)$$
 (2-6)

where m_a is the magnitude with a range of [-1,1], and $\omega(2\pi f)$ is the system angular frequency, and φ is the control angle.

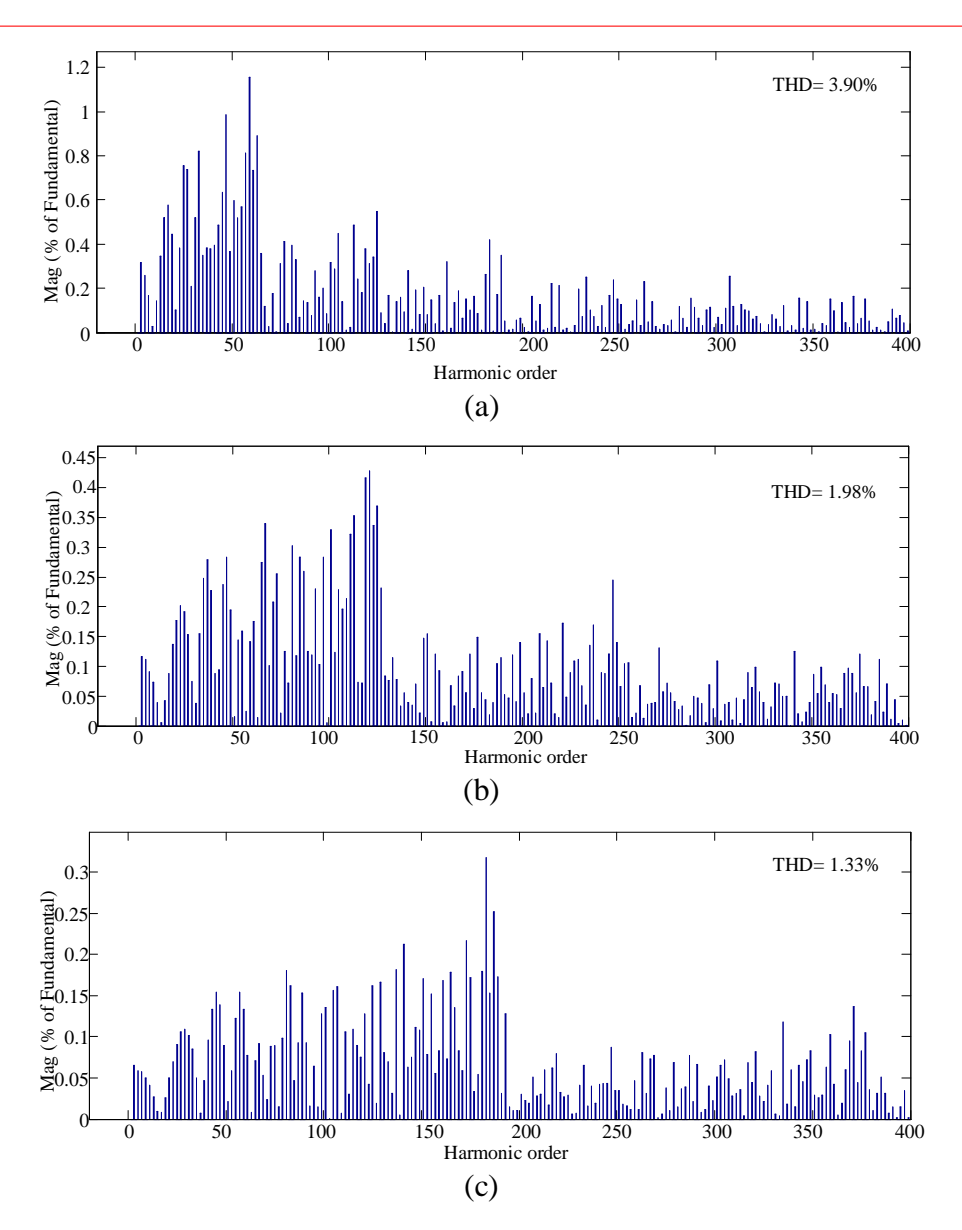


Fig. 2-7 FFT of the output voltage of the MMC phase-a: (a) 21-level; (b) 41-level; (c) 61-level

Substituting(2-6) and (2-1) into (2-4) and (2-5), we have

$$n_{ua} = \frac{N}{2} - round \left\{ \frac{N}{2} \cdot m_a \cos(\omega t + \varphi) \right\}$$
 (2-7)

$$n_{la} = \frac{N}{2} + round \left\{ \frac{N}{2} \cdot m_a \cos(\omega t + \varphi) \right\}$$
 (2-8)

Since $-1 \le m_a \cos(\omega t + \varphi) \le 1$, (2-9) is always satisfied during the modulation operations

$$0 \le n_{ua}, n_{la} \le N \tag{2-9}$$

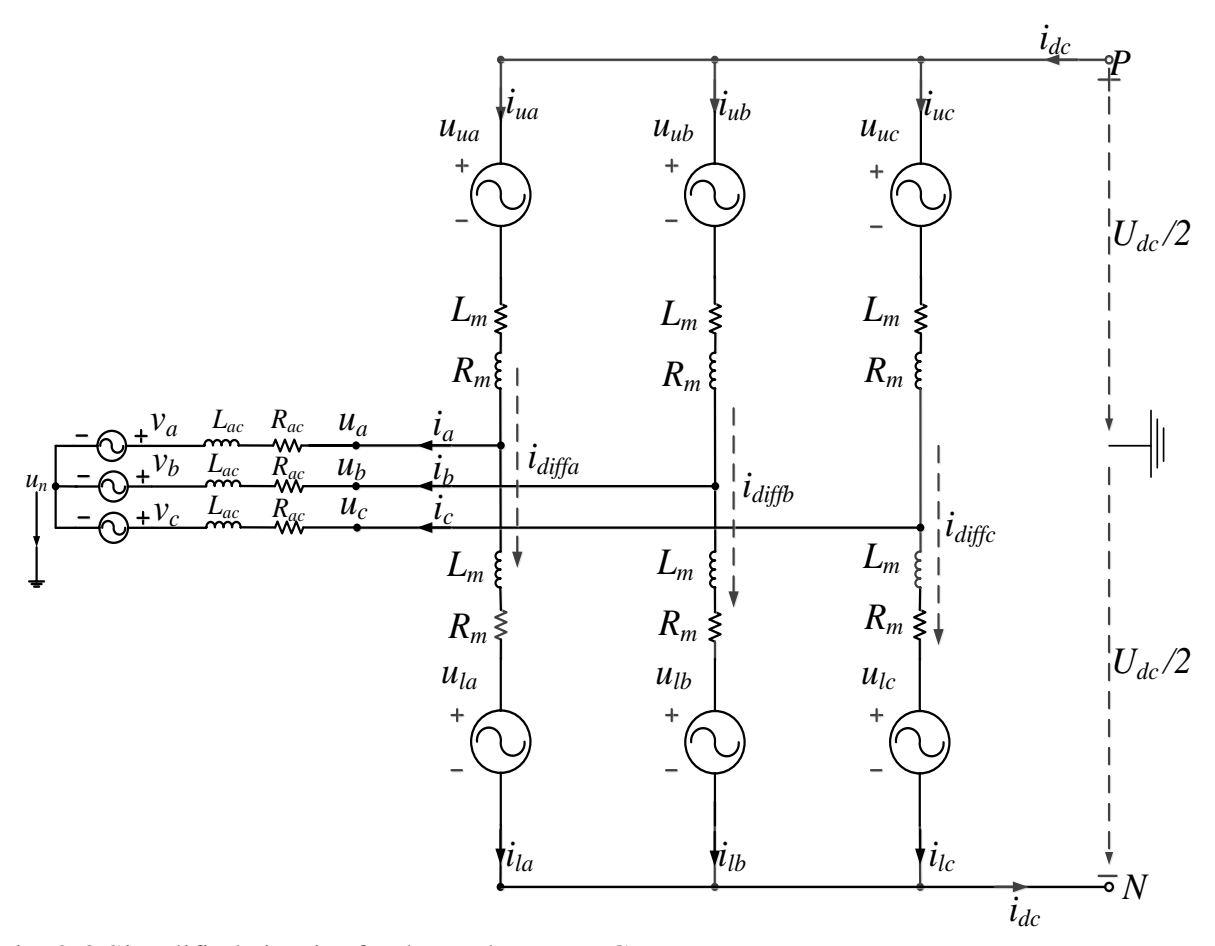


Fig. 2-8 Simplified circuit of a three-phase MMC

Fig. 2-6 (a) (b) (c) presents the ideal output voltage u_a for the 21-level, 41-level and 61-level MMC, respectively, and the corresponding total number of SMs inserted in one arm (N) is 20, 40 and 60. Fig. 2-6 clearly shows that with an increasing N, the quality of output voltage u_a improves.

Fig. 2-7 (a) (b) (c) shows the Fast Fourier Transform (FFT) results of the 3^{rd} order to the 400^{th} order harmonics of u_a at the 21-level, 41-level and 61-level MMC. In Fig. 2-7 (a), the THD at 21-level is 3.90%. The magnitudes of individual harmonics are less than 1.2% of the magnitude of the fundamental component. In Fig. 2-7 (b), the THD for 41-level is 1.98%. The magnitudes of individual harmonics are less than 0.45% of the magnitude of the fundamental component. In Fig. 2-7 (c), the THD at 61-level is 1.33%. The magnitudes of individual harmonics are all less than 0.35% of the magnitude of the fundamental component. It can be easily concluded that the THD of the output voltage decreases proportionally with level increases. Generally speaking, there are hundreds of levels in MMC-HVDC projects. Taking the world first MMC-HVDC, the Trans Bay Cable, as an example, 200 SMs are connected in each arm, that is, 201-levels in total.

2.4 MMC Equivalent Circuit

The three-phase MMC of Fig. 2-1 becomes amenable to analysis when modeled as Fig. 2-8. As indicated by arrows, the currents include: the AC current i_j (j=a,b,c), the differential current i_{diffj} (j=a,b,c), and the DC current i_{dc} . An important current is the circulating current $i_{cirj}(j=a,b,c)$, hidden in $i_{diffj}(j=a,b,c)$. Section 2.4 develops the equivalent circuit. In Fig. 2-8, the AC lines terminate in a WYE, with a neutral voltage un, which is not zero when not grounded. Section 2.4.1 is devoted to solving the neutral voltage u_n so that the Kirchhoff's Voltage and Current Laws can be used to establish simplified models. Section 2.4.2 unravels a property of the circulating current $i_{cirj}(j=a,b,c)$. With this knowledge, Circulating Current Suppression Control (CCSC) is implemented in chapter 3.

During a MMC operation, SMs are either inserted or bypassed during the normal operation. The capacitor voltages of all the SMs in one arm can be equivalent as one controlled voltage source. In Fig. 2-8, i_{diffj} (j=a,b,c) represent the differential current of phase-j (j=a,b,c) between the upper and the lower arm. During the normal operation, the upper arm and the lower arm of the j^{th} phase (j=a,b,c) share half of the AC current i_j (j=a,b,c). The upper arm and the lower arm carry the differential current i_{diffj} (j=a,b,c). The differential current i_{diffj} (j=a,b,c) consists of $i_{dc}/3$ and the circulating current i_{cirj} (j=a,b,c).

$$i_{uj} = \frac{1}{2}i_j + i_{diffj} \quad (j=a,b,c)$$
 (2-10)

$$i_{lj} = -\frac{1}{2}i_j + i_{diffj} \quad (j=a,b,c)$$
 (2-11)

$$i_{diffj} = \frac{1}{3}i_{dc} + i_{cirj} \quad (j=a,b,c)$$
 (2-12)

2.4.1 Derivation of Neutral Voltage

The 3-phase lines on the ac side usually terminate as an open WYE to exclude the zero sequence. This section derives u_n , the voltage of the neutral point. When applying Kirchhoff's voltage law (KVL) for the AC loop for the upper arms and lower arms, the results are as follows:

$$-\frac{1}{2}U_{dc} + u_{uj} + R_m i_{uj} + L_m \frac{di_{uj}}{dt} + R_{ac} i_j + L_{ac} \frac{di_j}{dt} + v_j + u_n = 0 \quad (j=a,b,c)$$
 (2-13)

$$\frac{1}{2}U_{dc} - u_{lj} - R_m i_{lj} - L_m \frac{di_{lj}}{dt} + R_{ac} i_j + L_{ac} \frac{di_j}{dt} + v_j + u_n = 0 \quad (j=a,b,c)$$
 (2-14)

Adding (2-13) and (2-14), we have

$$u_{uj} - u_{lj} + R_m(i_{uj} - i_{lj}) + L_m(\frac{di_{uj}}{dt} - \frac{di_{uj}}{dt}) + 2R_{ac}i_j + 2L_{ac}\frac{di_j}{dt} + 2v_j + 2u_n = 0 \ (j=a,b,c) \ (2-15)$$

Substituting (2-10) and (2-11) in (2-15)

$$u_{uj} - u_{lj} + R_m i_j + L_m \frac{di_j}{dt} + 2R_{ac} i_j + 2L_{ac} \frac{di_j}{dt} + 2v_j + 2u_n = 0 \quad (j=a,b,c)$$
 (2-16)

Rewriting (2-16) as a-b-c terms

$$u_{ua} - u_{la} + R_{m}i_{a} + L_{m}\frac{di_{a}}{dt} + 2R_{ac}i_{a} + 2L_{ac}\frac{di_{a}}{dt} + 2v_{a} + 2u_{n} = 0$$
 (2-17)

$$u_{ub} - u_{lb} + R_m i_b + L_m \frac{di_b}{dt} + 2R_{ac} i_b + 2L_{ac} \frac{di_b}{dt} + 2v_b + 2u_n = 0$$
 (2-18)

$$u_{uc} - u_{lc} + R_m i_c + L_m \frac{di_c}{dt} + 2R_{ac} i_c + 2L_{ac} \frac{di_c}{dt} + 2v_c + 2u_n = 0$$
 (2-19)

Summing (2-17), (2-18) and (2-19)

$$\sum_{j=a,b,c} \left(u_{uj} - u_{lj} \right) + \left(R_m + 2R_{ac} \right) \sum_{j=a,b,c} i_j + \left(L_m + 2L_{ac} \right) \sum_{j=a,b,c} \frac{di_j}{dt} + 2 \sum_{j=a,b,c} v_j + 6u_n = 0 \quad (j=a,b,c) \quad (2-20)$$

For a balanced three-phase system

$$\sum_{j=a,b,c} i_j = 0, \sum_{j=a,b,c} \frac{di_j}{dt} = 0, \sum_{j=a,b,c} u_j = 0$$
 (j=a,b,c) (2-21)

Substituting (2-21) in (2-20)

$$\sum_{j=a,b,c} \left(u_{uj} - u_{lj} \right) + 6u_n = 0 \qquad (j=a,b,c) \quad (2-22)$$

Therefore, the neutral voltage is

$$u_n = -\frac{1}{6} \left[\left(u_{ua} - u_{la} \right) + \left(u_{ub} - u_{lb} \right) + \left(u_{uc} - u_{lc} \right) \right]$$
 (2-23)

2.4.2 AC and DC Equivalent Circuit

Subtracting (2-14) from (2-13)

$$-U_{dc} + u_{uj} + u_{lj} + R_m(i_{uj} + i_{lj}) + L_m(\frac{di_{uj}}{dt} + \frac{di_{lj}}{dt}) = 0 \quad (j=a,b,c)$$
 (2-24)

Substituting (2-10) and (2-11) in (2-24)

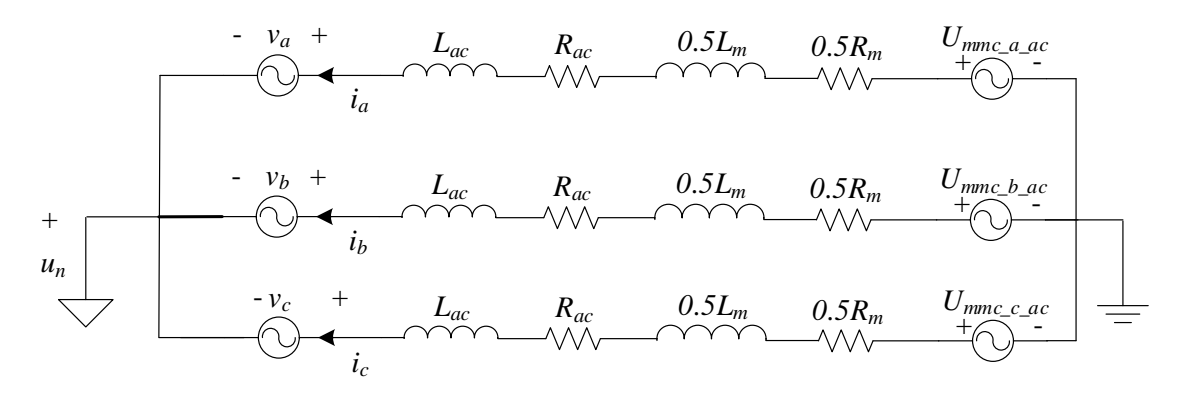


Fig. 2-9 AC side equivalent circuit of a three-phase MMC

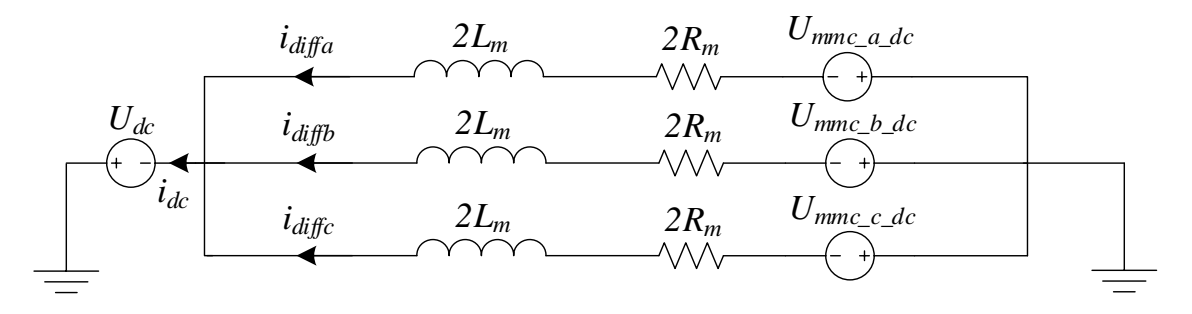


Fig. 2-10 DC side equivalent circuit of a three-phase MMC

$$-U_{dc} + u_{uj} + u_{lj} + 2R_m i_{diffj} + 2L_m \frac{di_{diffj}}{dt} = 0 (j=a,b,c) (2-25)$$

Two terms $U_{mmc_j_ac}$ and $U_{mmc_j_dc}$ (j=a,b,c) are defined to represent the equivalent AC or DC voltage generated by MMC, shown in (2-26) and (2-27)

$$U_{mmc_{-}j_{-}ac} = \frac{u_{lj} - u_{uj}}{2} \quad (j=a,b,c)$$
 (2-26)

$$U_{mmc_{-}j_{-}dc} = u_{uj} + u_{lj} \ (j=a,b,c)$$
 (2-27)

When substituting (2-26) to (2-16), the equation of the AC side equivalent circuit of the MMC is defined as

$$U_{mmc_{-}j_{-}ac} + (0.5L_m + L_{ac})\frac{di_j}{dt} + (0.5R_m + R_{ac})i_j + v_j + u_n = 0 \quad (j=a,b,c)$$
 (2-28)

Substituting (2-27) into (2-25), the equation of the DC side equivalent circuit of MMC is defined as

$$-U_{dc} + U_{mmc_{-j_{-}dc}} + 2R_{m}i_{diffj} + 2L_{m}\frac{di_{diffj}}{dt} = 0 (j=a,b,c) (2-29)$$

Based on (2-28) and (2-29), the AC side and the DC side equivalent circuit of a three-phase MMC are developed and shown in Fig. 2-9 and Fig. 2-10 respectively.

From Fig. 2-10

$$i_{diffa} + i_{diffb} + i_{diffc} = i_{dc} (2-30)$$

According to (2-12),

$$i_{diffa} + i_{diffb} + i_{diffc} = i_{dc} + \sum_{i=a,b,c} i_{cirj}$$
(2-31)

Therefore,

$$\sum_{i=a,b,c} i_{cirj} = 0 (2-32)$$

(2-32) is applied in the Circulating Current Suppression Control (CCSC) in chapter 3.

2.5 Chapter Summary

The 3-phase HBSM-based MMC system has been introduced in this chapter. By triggering the gate signals of the IGBTs in a submodule with respect to the current directions, three operation states are controlled. Among the three states, one state represents the block state, which is applied during the pre-charge process, or, short circuit fault protection. The other two states ('on state' or 'off state') stand for normal operation into which the SM is either inserted or bypassed from the upper or lower arm of one phase.

The basic operation principle of the HBSM-MMC was studied next. In order to ensure that the MMC operates with a constant DC voltage, the total number of 'on state' SMs in the upper and lower arms must equal to the total number of the SMs connected in each arm. This ensures that the sum of the capacitor voltages of the SMs is equal to the DC voltage across the DC bus at all times. While observing this constraint, the Nearest-Level Modulation (NLM) method is implemented. NLM switching at a fundamental frequency produces output voltages that replicate the modulation signal with a high THD. The illustration of waveforms, when the level number is small, was given. However, in MMC-HVDC application, when the number is high enough, the harmonics are neglected because of their small magnitudes.

In using Kirchhoff's voltage and current laws of circuit theory, the equivalent circuits for both the AC and DC sides of the MMC have been generated. The equivalent circuits will be applied to the investigations of later chapters.

Chapter 3. Modular Multilevel Converter Model Based on Ordinary Differential Equation (ODE)

3.1 Introduction

Apart from laboratory prototyping, research and design rely on digital simulations that are computation-intensive for MMCs. This is because detail simulation is based on the numerical integration of ordinary differential equations, that is, one set of equations for one sub-module (SM). But there are as many as a hundred sub-modules in one MMC phase. The turnaround computation time is reduced by parallel processing and averaging methods [72]-[74][139]. In the last two decades, the formulation based on the ordinary differential equations (ODE) of [78] has increased in speed, since it requires only 12 ordinary differential equations (ODE) for one MMC-HVDC station. There is a further speed increase due to the use of a coarser integration step-size [79][80].

Inherent nonlinearity in the MMC produces circulating currents, which appear as voltage ripples. The ripples need to be eliminated to satisfy the THD standard. The frequency of the circulating currents corresponds to twice the line frequency. The circulating current can be reduced by large sub-module capacitors, but they are bulky and costly. Pioneering efforts [43]-[45][50] to reduce the circulating currents are based on singling out its second harmonic by means of an electronic/digital filter and through applying the negative feedback in order to eliminate the second-harmonic as an error. Compared to the overall cost of the MMC HVDC, the cost of electronic/digital filters is negligibly small. For reliability, however, it is preferred to avoid adding electronic or digital filters since they complicate the system equations; therefore, analysis to ensure that they will not lead to instability [140] is challenging. The innovative method proposed in this chapter reduces the probability of hidden instability, because it does not require an electronic/digital filter.

In this chapter, the capacitor modulation theory is introduced first given that it leads to the MMC model based on the ordinary differential equation (ODE) of [78]. Next, the circulating current suppression control (CCSC) is proposed. The method is validated through simulation results.

The third part of this chapter tests the grounded WYE connection of the ac-side of the MMC-HVDC model. This third part contains a long explanation. The circulating current is undesirable because it proliferates the 3rd-order and odd harmonics on the AC side [141]. Most MMC-HVDC designs have the AC-side connected in open-wye so as to prevent the flow the 3rd-order and odd harmonics. Protection engineers prefer a grounded WYE to detect the zero-sequence. By suppressing the circulating current by the CCSC method, grounding the WYE connection of the AC-side transformer test will not prevent the flow of 3rd-order and odd harmonics.

The proposed MMC ODE model is validated by comparing its simulation results with the results obtained by the MMC Detail Equivalent Model (DEM), both of which are simulated in RT-LAB.

3.2 MMC ODE Model

3.2.1 Capacitor Modulation Theory

The schematic of the phase-a is depicted in Fig. 3-1. In Fig. 3-1; the upper arm and lower share half of the AC current and the voltage across the capacitor are assumed to be equal in all SMs. n_{ua} and n_{la} stand for the total number of the inserted SMs in the upper and lower arms, which are determined by the modulation signals m_{ua} and m_{la} .

 $u_{\Sigma Cua}$ and $u_{\Sigma Cla}$ are defined to represent the voltages across N capacitors in the upper and lower arms, respectively. u_{ua} and u_{la} symbolize the voltage across the upper and lower arm, respectively: $u_{ua} = n_{ua}u_{\Sigma cua}$ and $u_{la} = u_{la}u_{\Sigma cla}$.

The operation of the upper arm in Fig.3-1 is illustrated in Fig. 3-2. Fig. 3-2 (a) shows the modulating signal $m_{ua}(t)$. From the Nearest Level Modulation algorithm presented in Chapter 2 section 2.3.2, the modulation signal $m_{ua}(t)$ ($0 < m_{ua}(t) < U_{dc}$) connects $n_{ua}(t)$ ($0 < n_{ua}(t) < N$) capacitors (each of size C) in series, as illustrated in Fig. 3-2 (b). When the total number of capacitors in each arm is N, and when the voltage across the DC buses is U_{dc} , the instantaneous, connected number is

$$n_{ua}(t) = \frac{N}{U_{de}} m_{ua}(t)$$
 (3-1)

The output voltage u_a is illustrated in Fig. 3-2 (c).

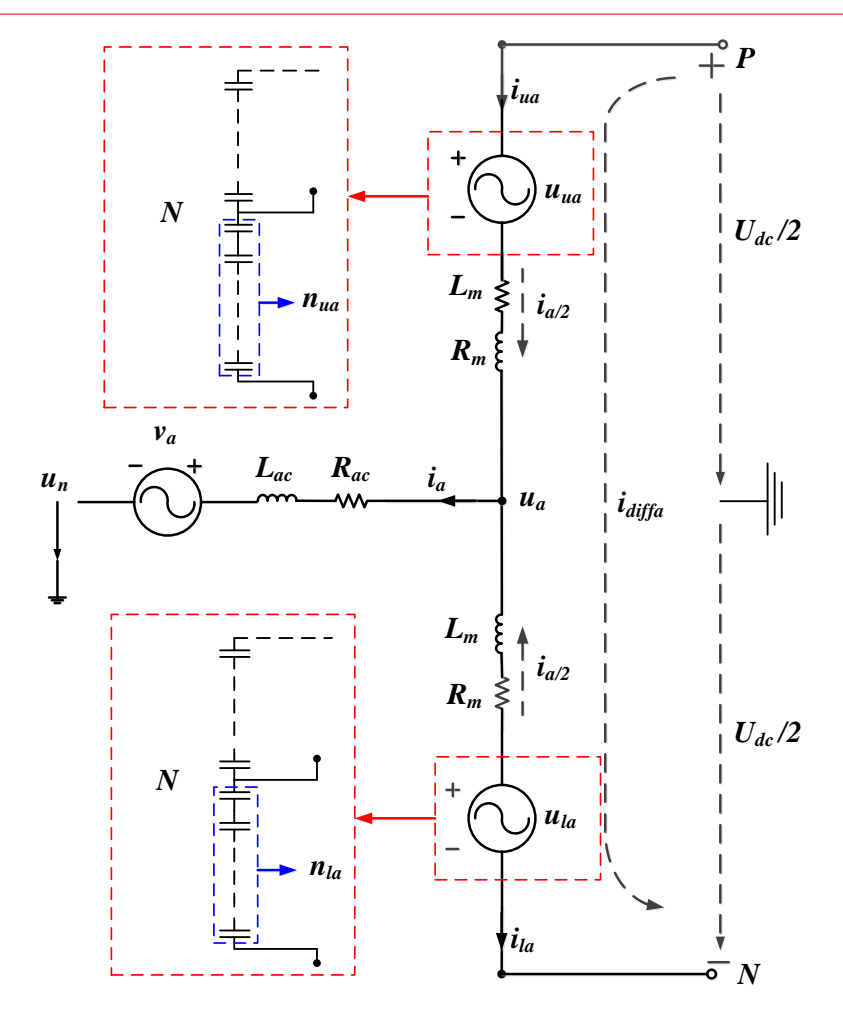


Fig. 3-1 Phase-a of the MMC show n_{ua} capacitors string in the upper arm and n_{la} capacitors string in the lower arm.

The equivalent capacitor size is $C/n_{ua}(t)$. From circuit theory, the electric charge q(t) of a capacitor of size $C/n_{ua}(t)$ is related to the voltage u(t). If u(t) is the voltage of the arm, we have:

$$q(t) = \frac{C}{n_{ua}(t)}u(t) \tag{3-2}$$

The electric current i_{ua} is:

$$i_{ua}(t) = \frac{dq(t)}{dt} = \frac{Cdu(t)}{n_{ua}(t)dt} - \frac{Cu(t)}{n_{ua}(t)^2} \frac{dn_{ua}(t)}{dt}$$
(3-3)

Research results based on retaining only the first term on the right side of (3-3) have been validated by simulations and a limited number of experimental tests [141][142]. In spite of the validation, there is still concern over the treatment of switching noise in the theoretical derivation. This section shows that switching noise is accounted for in the term containing $dn_{ua}(t)/dt$ in (3-3).

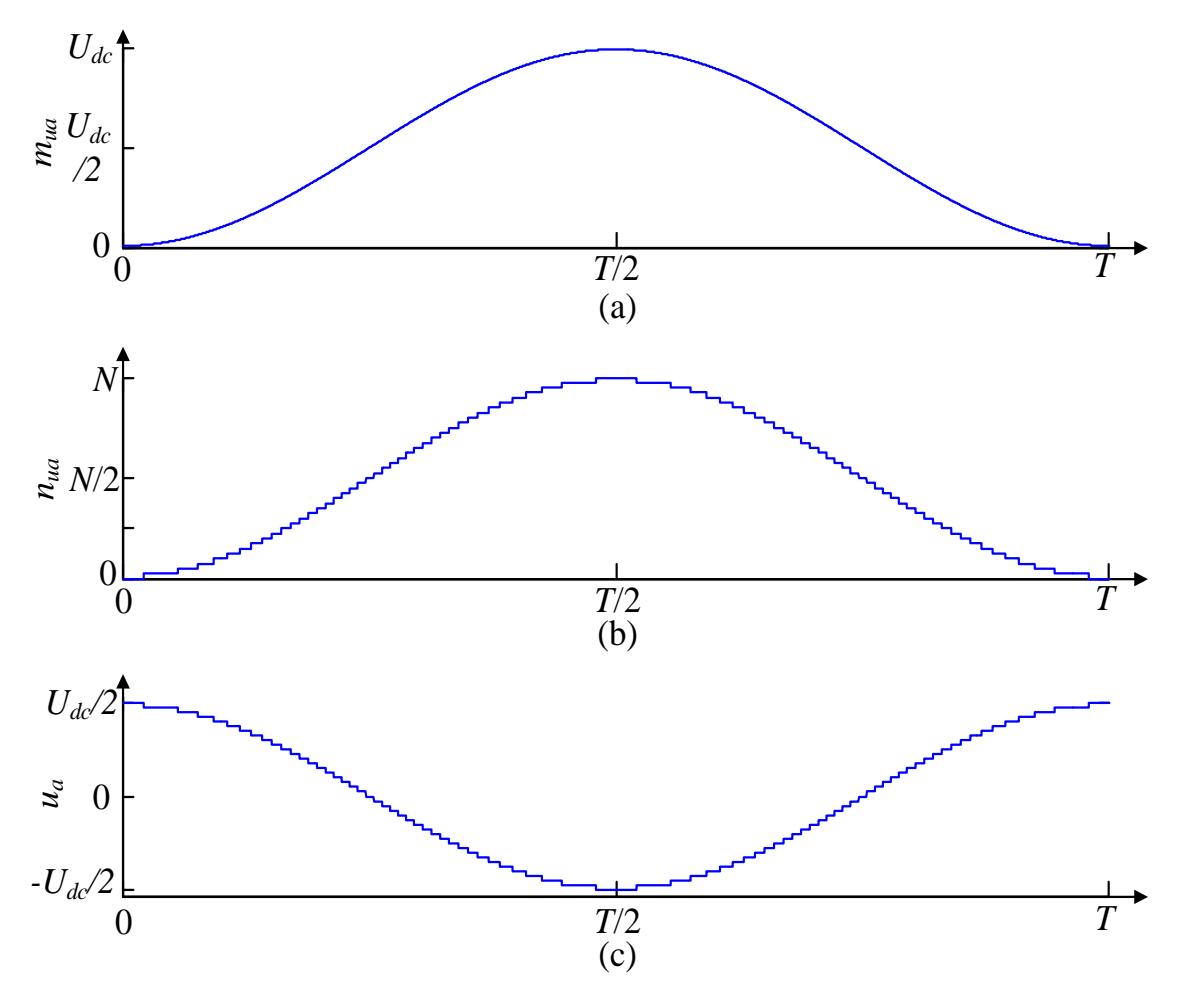


Fig. 3-2 (a) Modulation signal $m_{ua}(t)$; (b) $n_{ua}(t)$, number of capacitors, connected in string in upper arm as commanded by $m_{ua}(t)$; (c) output voltage u_a

The variation of $n_{ua}(t)$ in the MMC operation is shown in Fig. 3-2 (b). Between two switching instants, $n_{ua}(t)$ is a constant and therefore $dn_{ua}(t)/dt=0$ in (3-3). Non-zero $dn_{ua}(t)/dt$ occurs at the instant when one or more capacitors are connected to or disconnected from the string of capacitors. Mathematically, the differentiation of step functions leads to impulse functions. As (3-3) is an equation of current terms, the non-zero $dn_{ua}(t)/dt$ terms constitute impulse currents. In (3-3), the current impulses are integrated back as successive step voltage functions which account for the granularity of the voltage $u_{ua}(t)$, as illustrated in Fig. 3-2 (c). Since the switching occurrences are at high frequencies, they have been disregarded as switching noise in the ODE formulation of [79].

Disregarding the $dn_{ua}(t)/dt$ term in (3-3), the remaining term is:

$$\frac{C}{n_{\cdots}(t)}\frac{du(t)}{dt} = i_{ua}(t) \tag{3-4}$$

Substituting (3-1) in (3-4)

$$\frac{C}{N}\frac{du(t)}{dt} = \frac{i_{ua}(t)m_{ua}(t)}{U_{dc}}$$
(3-5)

Considering $i_{ua}(t)m_{ua}(t)/U_{dc}$ is the current flowing through one capacitor. The voltage $u^{I}(t)$ across a single capacitor is solved by

$$C\frac{du^{1}(t)}{dt} = \frac{i_{ua}(t)m_{ua}(t)}{U_{dc}}$$
 (3-6)

The voltage across N capacitor in the upper arm of phase-a is

$$u_{\varsigma_{cua}}(t) = Nu^{1}(t) \tag{3-7}$$

The value of N capacitors connected in series is C/N. Thus, the voltage in (3-5) is $u_{\sum cua}(t)$, and the voltage across N capacitors connected in series (3-5) is rewritten as

$$\frac{C}{N}\frac{du_{\Sigma cua}(t)}{dt} = \frac{i_{ua}(t)m_{ua}(t)}{U_{da}}$$
(3-8)

The voltage across the string of $n_{ua}(t)$ capacitors is:

$$u_{ua} = \frac{n_{ua}(t)}{N} u_{\Sigma cua}(t) = \frac{m_{ua}(t)}{U_{L}} u_{\Sigma cua}(t)$$
 (3-9)

3.2.2 Single-Phase MMC ODE Model

Because phase-*b* and phase-*c* are similar to phase-*a*, and to simplify the analysis, only phase-*a* of the MMC is discussed in this section. Based on Fig. 2-9 and Fig. 2-10, the AC and DC sides equivalent circuits of the MMC phase-*a* are shown in Fig. 3-3 and Fig. 3-4, respectively.

According to the modulation strategy, the modulation signals for the upper and lower arms are

$$m_{ua} = \left(\frac{1}{2} - \frac{u_{refa}}{U_{dc}}\right) \cdot U_{dc} \tag{3-10}$$

$$m_{la} = \left(\frac{1}{2} + \frac{u_{refa}}{U_{dc}}\right) \cdot U_{dc} \tag{3-11}$$

where u_{refa} is the phase-a reference signal for modulation.

Substituting (3-10) and (3-11) in (3-9), we have

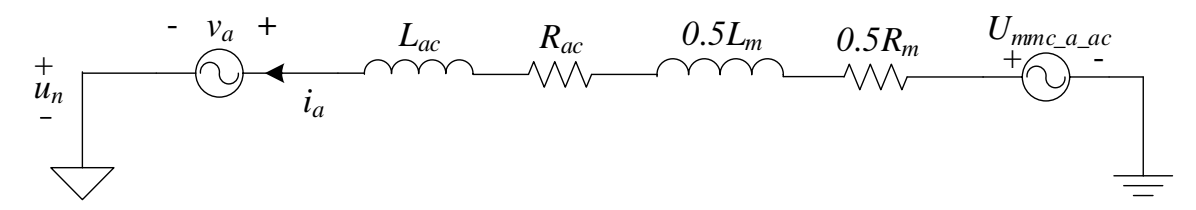


Fig. 3-3 AC side equivalent circuit of the MMC phase-a

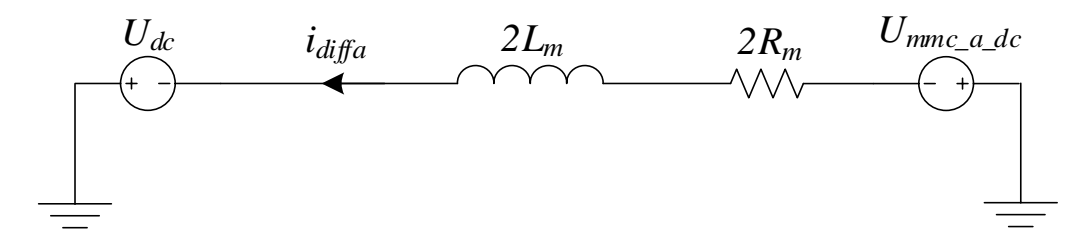


Fig. 3-4 DC side equivalent circuit of the MMC phase-a

$$u_{ua} = \left(\frac{1}{2} - \frac{u_{refa}}{U_{dc}}\right) u_{\Sigma cua} \tag{3-12}$$

$$u_{la} = \left(\frac{1}{2} + \frac{u_{refa}}{U_{dc}}\right) u_{\Sigma cla}$$
(3-13)

Substituting(3-12) and (3-13) in (2-26) and (2-27), we have:

$$U_{mmc_a_ac} = \left(\frac{1}{4} + \frac{u_{refa}}{2U_{dc}}\right) u_{\Sigma cla} - \left(\frac{1}{4} - \frac{u_{refa}}{2U_{dc}}\right) \cdot u_{\Sigma cua}$$
(3-14)

$$U_{mmc_a_dc} = \left(\frac{1}{2} + \frac{u_{refa}}{U_{dc}}\right) u_{\Sigma cla} + \left(\frac{1}{2} - \frac{u_{refa}}{U_{dc}}\right) u_{\Sigma cua}$$
(3-15)

Revising (2-28) and (2-29):

$$\left(\frac{1}{2}L_{m} + L_{ac}\right)\frac{di_{a}}{dt} = U_{mmc_{-}a_{-}ac} - \left(\frac{1}{2}R_{m} + R_{ac}\right)i_{a} - v_{a} - u_{n}$$
(3-16)

$$2L_{m}\frac{di_{diffa}}{dt} = U_{dc} - U_{mmc_{a}_{dc}} - 2R_{m}i_{diffa}$$
 (3-17)

According to (3-8), the total capacitor voltage in the lower arm of phase-a is:

$$\frac{du_{\Sigma cla}(t)}{dt} = \frac{N}{CU_{dc}} i_{la}(t) m_{la}(t)$$
(3-18)

Rewrite (2-10) and (2-11), the upper and lower arm currents for phase-a are

$$i_{ua} = \frac{1}{2}i_a + i_{diffa} \tag{3-19}$$

$$\dot{i}_{la} = -\frac{1}{2}\dot{i}_a + \dot{i}_{diffa} \tag{3-20}$$

Applying the modulated capacitor model and substituting (3-19) and (3-20) in (3-8) and (3-18):

$$C\frac{du_{\sum cua}}{dt} = N\left(\frac{1}{2} - \frac{u_{refa}}{U_{dc}}\right)\left(\frac{1}{2}i_a + i_{diffa}\right)$$
(3-21)

$$C\frac{du_{\sum cla}}{dt} = N\left(\frac{1}{2} + \frac{u_{refa}}{U_{dc}}\right)\left(-\frac{1}{2}i_a + i_{diffa}\right)$$
(3-22)

Substituting (3-14) and (3-15) in (3-16) and (3-17):

$$\frac{di_{a}}{dt} = \frac{1}{\left(\frac{1}{2}L_{m} + L_{ac}\right)} \left[\left(\frac{1}{4} + \frac{u_{refa}}{2U_{dc}}\right) u_{\Sigma cla} - \left(\frac{1}{4} - \frac{u_{refa}}{2U_{dc}}\right) \cdot u_{\Sigma cua} - \left(\frac{1}{2}R_{m} + R_{ac}\right) i_{a} - v_{a} - u_{n} \right] \quad (3-23)$$

$$\frac{di_{diffa}}{dt} = \frac{1}{2L_m} \left[U_{dc} - \left(\frac{1}{2} + \frac{u_{refa}}{U_{dc}} \right) u_{\Sigma cla} - \left(\frac{1}{2} - \frac{u_{refa}}{U_{dc}} \right) \cdot u_{\Sigma cua} - 2R_m i_{diffa} \right]$$
(3-24)

(3-21) to (3-24) represent the single-phase MMC ODE Model.

Assume $x=[x_1,x_2,x_3,x_4]=[u_{\sum cla},u_{\sum cla},i_{diffa},i_a],$ (3-21) to (3-24) are rewritten as:

$$\frac{dx_1}{dt} = \frac{1}{C_{arm}} \left(\frac{1}{2} - \frac{u_{refa}}{U_{dc}} \right) \cdot \left(x_3 + \frac{1}{2} x_4 \right)$$
 (3-25)

$$\frac{dx_2}{dt} = \frac{1}{C_{arm}} \left(\frac{1}{2} + \frac{u_{refa}}{U_{dc}} \right) \cdot \left(x_3 - \frac{1}{2} x_4 \right)$$
 (3-26)

$$\frac{dx_3}{dt} = \frac{1}{L_m} \left[\frac{U_{dc}}{2} - \left(\frac{1}{4} + \frac{u_{refa}}{2U_{dc}} \right) x_2 - \left(\frac{1}{4} - \frac{u_{refa}}{2U_{dc}} \right) \cdot x_1 - R_m x_3 \right]$$
(3-27)

$$\frac{dx_4}{dt} = \frac{1}{L_{eq}} \left[\left(\frac{1}{4} + \frac{u_{refa}}{2U_{dc}} \right) x_2 - \left(\frac{1}{4} - \frac{u_{refa}}{2U_{dc}} \right) \cdot x_1 - R_{eq} x_4 - v_a - u_n \right]$$
(3-28)

where
$$C_{arm} = \frac{C}{N}$$
, $L_{eq} = 0.5L_m + L_{ac}$, $R_{eq} = 0.5R_m + R_{ac}$, $u_n = 0$

Combining(3-25) to (3-28), the ODE model for MMC single phase is rewritten as the following nonlinear equation:

$$\underline{\dot{x}} = f\left(\underline{x}, \underline{u}, t\right) \tag{3-29}$$

where \underline{x} present for the system state variables and \underline{u} are the system inputs.

3.2.3 Three-Phase MMC ODE Model

The three-phase MMC ODE model is extended based on the single-phase MMC ODE Model discussed in the previous section.

let $\underline{x} = [x_1, ..., x_{12}] = [u_{\sum cua}, u_{\sum cub}, u_{\sum cuc}, u_{\sum cla}, u_{\sum clb}, u_{\sum clc}, i_{diffa}, i_{diffb}, i_{diffc}, i_a, i_b, i_c]$, the equations for the three-phase MMC ODE model are shown as following:

$$\frac{dx_1}{dt} = \frac{1}{C_{arm}} \left(\frac{1}{2} - \frac{u_{refa}}{U_{dc}} \right) \cdot \left(x_7 + \frac{1}{2} x_{10} \right)$$
(3-30)

$$\frac{dx_2}{dt} = \frac{1}{C_{qrm}} \left(\frac{1}{2} - \frac{u_{refb}}{U_{dc}} \right) \cdot \left(x_8 + \frac{1}{2} x_{11} \right)$$
(3-31)

$$\frac{dx_3}{dt} = \frac{1}{C_{qrm}} \left(\frac{1}{2} - \frac{u_{refc}}{U_{dc}} \right) \cdot \left(x_9 + \frac{1}{2} x_{12} \right)$$
 (3-32)

$$\frac{dx_4}{dt} = \frac{1}{C_{arm}} \left(\frac{1}{2} + \frac{u_{refa}}{U_{dc}} \right) \cdot \left(x_7 - \frac{1}{2} x_{10} \right)$$
 (3-33)

$$\frac{dx_5}{dt} = \frac{1}{C_{arm}} \left(\frac{1}{2} + \frac{u_{refb}}{U_{dc}} \right) \cdot \left(x_8 - \frac{1}{2} x_{11} \right)$$
 (3-34)

$$\frac{dx_6}{dt} = \frac{1}{C_{qrm}} \left(\frac{1}{2} + \frac{u_{refc}}{U_{dc}} \right) \cdot \left(x_9 - \frac{1}{2} x_{12} \right)$$
 (3-35)

$$\frac{dx_7}{dt} = \frac{1}{L_m} \left[\frac{U_{dc}}{2} - \left(\frac{1}{4} + \frac{u_{refa}}{2U_{dc}} \right) x_4 - \left(\frac{1}{4} - \frac{u_{refa}}{2U_{dc}} \right) \cdot x_1 - R_m x_7 \right]$$
(3-36)

$$\frac{dx_8}{dt} = \frac{1}{L_m} \left[\frac{U_{dc}}{2} - \left(\frac{1}{4} + \frac{u_{refb}}{2U_{dc}} \right) x_5 - \left(\frac{1}{4} - \frac{u_{refb}}{2U_{dc}} \right) \cdot x_2 - R_m x_8 \right]$$
(3-37)

$$\frac{dx_9}{dt} = \frac{1}{L_m} \left[\frac{U_{dc}}{2} - \left(\frac{1}{4} + \frac{u_{refc}}{2U_{dc}} \right) x_6 - \left(\frac{1}{4} - \frac{u_{refc}}{2U_{dc}} \right) \cdot x_3 - R_m x_9 \right]$$
(3-38)

$$\frac{dx_{10}}{dt} = \frac{1}{L_{eq}} \left[\left(\frac{1}{4} + \frac{u_{refa}}{2U_{dc}} \right) x_4 - \left(\frac{1}{4} - \frac{u_{refa}}{2U_{dc}} \right) \cdot x_1 - R_{eq} x_{10} - v_a - u_n \right]$$
(3-39)

$$\frac{dx_{11}}{dt} = \frac{1}{L_{eq}} \left[\left(\frac{1}{4} + \frac{u_{refa}}{2U_{dc}} \right) x_5 - \left(\frac{1}{4} - \frac{u_{refb}}{2U_{dc}} \right) \cdot x_2 - R_{eq} x_{11} - v_b - u_n \right]$$
(3-40)

$$\frac{dx_{12}}{dt} = \frac{1}{L_{eq}} \left[\left(\frac{1}{4} + \frac{u_{refc}}{2U_{dc}} \right) x_6 - \left(\frac{1}{4} - \frac{u_{refc}}{2U_{dc}} \right) \cdot x_3 - R_{eq} x_{12} - v_c - u_n \right]$$
(3-41)

where
$$C_{arm} = \frac{C}{N}$$
, $L_{eq} = 0.5L_m + L_{ac}$, $R_{eq} = 0.5R_m + R_{ac}$, $u_n = -\frac{1}{6}[(u_{ua} - u_{la}) + (u_{ub} - u_{lb}) + (u_{uc} - u_{lc})]$ or

0, u_{ref} (j=a,b,c) are the three-phase reference signals for modulation.

3.3 Circulating Current Suppression Control (CCSC)

3.3.1 Principle of CCSC

The feedback reduction methods of [43][45][50] depend on using an electronic/digital filter to identify the circulating currents that are used as an error to be eliminated by negative feedback. In the MMC-HVDC, the cost of the filters is negligibly small. But the addition of sub-systems of any kind leads to a complexity instability analysis. Since the method described here does not add an electronic/digital filter, it is more reliable.

Feedback is introduced through the signals $\xi_j(j=a,b,c)$, which are added in the contents of u_{refj} (j=a,b,c) from (3-30) to (3-41). The references of phase-a, phase-b and phase-c are:

$$u_{refa} = M\cos(\omega_0 t + \delta) + \xi_a \tag{3-42}$$

$$u_{refb} = M\cos(\omega_0 t - 120^{\circ} + \delta) + \xi_b$$
 (3-43)

$$u_{refc} = M \cos(\omega_0 t - 240^{\circ} + \delta) + \xi_c$$
 (3-44)

where M is the magnitude control, ω_0 is the angular frequency, and δ is the voltage angle control.

The sections below strictly show the isolation of the circulating currents to form the feedback signals $\xi_j(j=a,b,c)$. In Fig. 3-1, for phase-a, the portion of the ac-current is defined as:

$$i_a = I_{ac} \cos(\omega_0 t + \varphi) \tag{3-45}$$

where φ is the phase angle and I_{ac} equates to the magnitude of the AC current.

$$i_{diffa} = \frac{1}{3}i_{dc} + \sum_{i=1}^{\infty} I_{2j}\cos(2j\omega_0 t + \mu_j)$$
 (3-46)

where i_{dc} is the current measured in the DC bus, and where the circulating current i_{cira} is expressed as a Fourier Series through the formula:

$$i_{cira} = \sum_{i=1}^{\infty} I_{2j} \cos(2j\omega_0 t + \mu_j)$$
 (3-47)

The currents flowing through the three-phase upper arm capacitors of Fig. 3-1 are:

$$i_{ua} = \frac{1}{2} I_{ac} \cos(\omega_0 t + \varphi) + \frac{1}{3} i_{dc} + \sum_{j=1}^{\infty} I_{2j} \cos(2j\omega_0 t + \mu_j)$$
 (3-48)

$$i_{ub} = \frac{1}{2} I_{ac} \cos(\omega_0 t + \varphi - 120^\circ) + \frac{1}{3} i_{dc} + \sum_{j=1}^{\infty} I_{2j} \cos(2j(\omega_0 t - 120^\circ) + \mu_j)$$
(3-49)

$$i_{uc} = \frac{1}{2} I_{ac} \cos(\omega_0 t + \varphi + 120^\circ) + \frac{1}{3} i_{dc} + \sum_{i=1}^{\infty} I_{2i} \cos(2j(\omega_0 t + 120^\circ) + \mu_i)$$
(3-50)

Adding (3-48), (3-49) and (3-50), the upper DC bus current is:

$$i_{ua} + i_{ub} + i_{uc} = i_{dc} ag{3-51}$$

This is because:

$$I_{ac}\cos(\omega_0 t + \varphi) + I_{ac}\cos(\omega_0 t + \varphi - 120^\circ) + I_{ac}\cos(\omega_0 t + \varphi + 120^\circ) = 0$$
 (3-52)

$$\cos(2j\omega_0 t + \mu_j) + \cos[(2j(\omega_0 t - 120^\circ) + \mu_j] + \cos[(2j(\omega_0 t - 240^\circ) + \mu_j] = 0 \text{ for } j = 1, 2... \infty$$
 (3-53)

From (3-45) to (3-50), it follows that the three-phase circulating currents can be obtained by subtracting portions of the DC-side and the AC-side currents so that filters are not required.

$$i_{cira} = i_{ua} - \frac{1}{2} I_{ac} \cos(\omega_0 t + \varphi) - \frac{1}{3} i_{dc}$$
 (3-54)

$$i_{cirb} = i_{ub} - \frac{1}{2}I_{ac}\cos(\omega_0 t + \varphi - 120^\circ) - \frac{1}{3}i_{dc}$$
 (3-55)

$$i_{circ} = i_{uc} - \frac{1}{2} I_{ac} \cos(\omega_0 t + \varphi + 120^\circ) - \frac{1}{3} i_{dc}$$
 (3-56)

The signals $\xi_j(j=a,b,c)$ added to the modulating signals of (3-42) to (3-44) are the outputs of *P-I* blocks. K_P is the proportional gain and K_I expresses the integral gain of the circulating currents from (3-54) through (3-56):

$$\xi_a = K_p i_{cira} + K_I \int_{-\infty}^{t} i_{cira}(\tau) d\tau$$
 (3-57)

$$\xi_b = K_P i_{cirb} + K_I \int_{-\infty}^{t} i_{cirb}(\tau) d\tau$$
 (3-58)

$$\xi_c = K_P i_{circ} + K_I \int_{-\infty}^t i_{circ}(\tau) d\tau$$
 (3-59)

3.3.2 CCSC Tests

The three-phase MMC ODE model with CCSC has been implemented in MATLAB-SIMULINK.

The results shown in Fig. 3-5, Fig. 3-6 and Fig. 3-7 are from the same simulation run, which has reached steady-state at t=3.0s without feedback reduction of the circulating current. At t=3.0s, the feedback elimination method is applied. At t=3.25s, the steady-state is reached. The measurements for 2.95 < t < 3.0 should be compared with those for 3.25 < t < 3.3s. The three figures show effective reductions of the circulating current by means of the CCSC.

Fig. 3-5 shows the circulating currents of (3-54), (3-55) and (3-56), which are different from i_{diff} of Fig. 3-6 because $i_{dc}/3$ is added. The reduction of circulating currents means that conduction and switching losses in the IGBTs are reduced.

Fig. 3-7 shows the voltage across the capacitor of a single sub-module. In this example, 2kV is the designed average voltage. For *C*=9mF, the overvoltage of about 11.5% is reduced to about 4%, which is when the circulating current is eliminated. The dominant fluctuation in Fig. 3-7 is the line frequency of 50 Hz. The distortion is due to the circulating current, which when reduced, lowers the voltage peaks. IGBTs are more prone to failure from overvoltage than from over-current. Parameters used for this experiment are shown in Table 3-I.

Table 3-I Parameters used in CCSC tests

Parameters	Values		
DC Grid Voltage U_{dc}	400kV		
AC Grid Voltage	220kV		
Number of Sub-modules per Arm N	200		
Sub-module capacitor voltage u_c	2kV		
Arm Inductance L_m	40mH		
Arm Equivalent Resistance R_m	0.1Ω		
SM Capacitance C	9mF		
AC Equivalent Inductance L_{ac}	50mH		
AC Equivalent Resistance R_{ac}	0.1Ω		
Control Parameters K_P	0.5		
Control Parameters K_I	5		
Nominated Power P_{rated}	400MW		
Frequency f	50Hz		

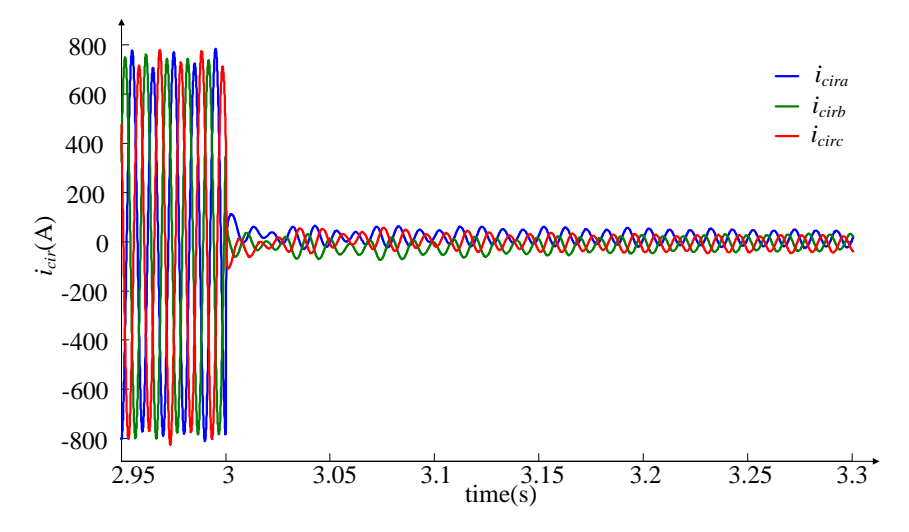


Fig. 3-5 i_{cira} , i_{cirb} , i_{circ} of the three-phase MMC ODE Model

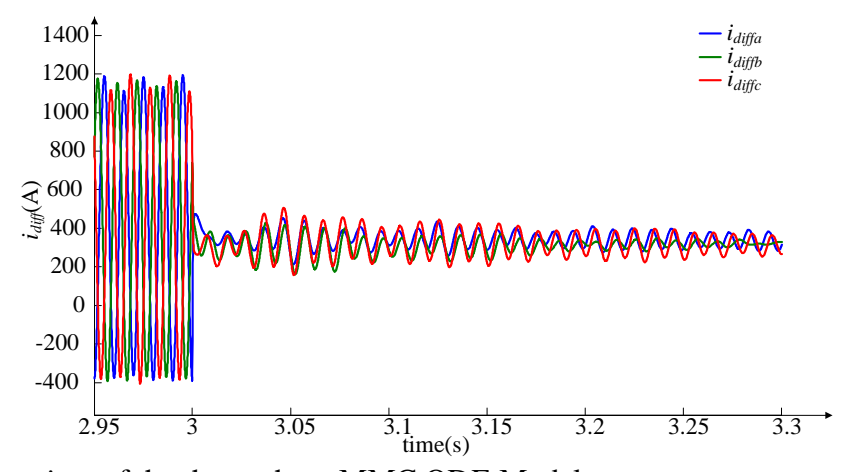


Fig. 3-6 i_{diffa} , i_{diffb} , i_{diffc} of the three-phase MMC ODE Model

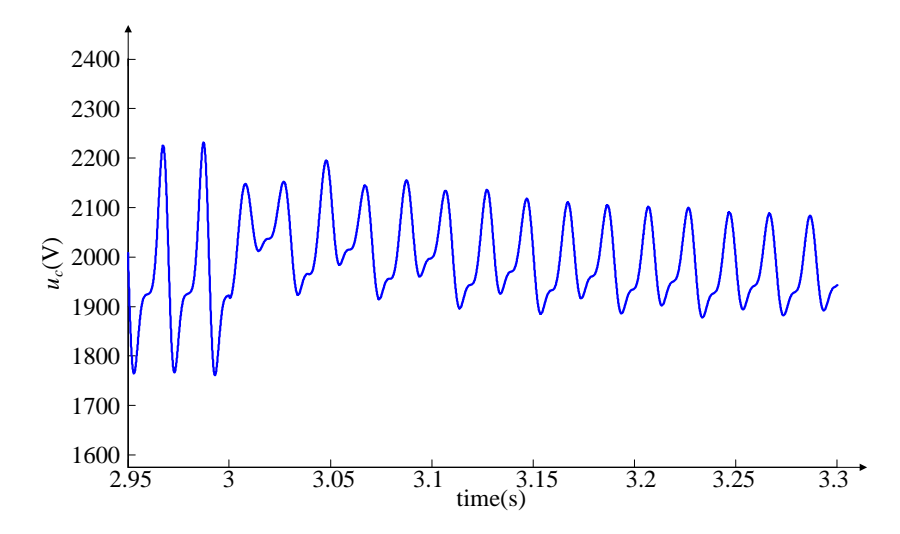


Fig. 3-7 Capacitor voltage in the phase-a upper arm.

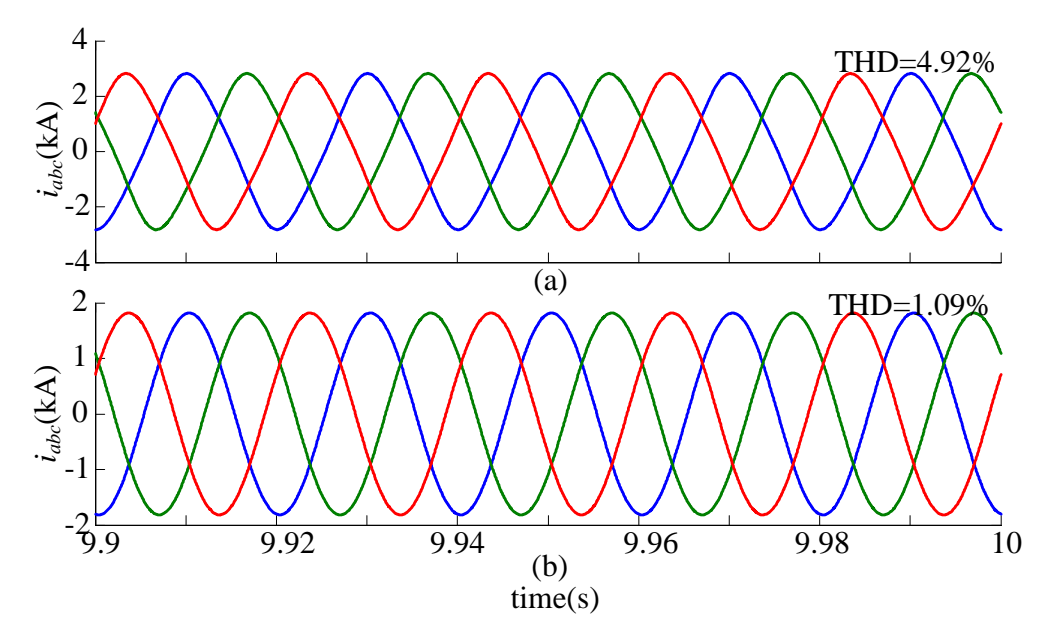


Fig. 3-8 Simulations of 3-phase AC currents when AC-side transformers have a grounded WYE connection. (a) without CCSC; (b) with CCSC.

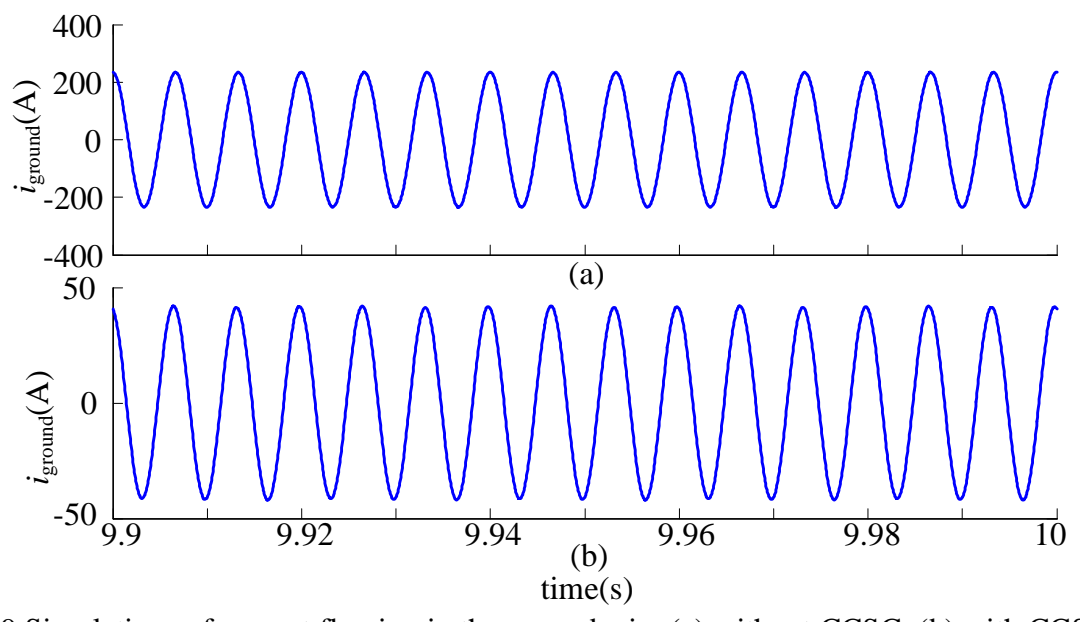


Fig. 3-9 Simulations of current flowing in the ground wire (a) without CCSC; (b) with CCSC.

3.4 Grounding WYE Connection of AC-Side Transformers Tests

MMC-HVDC has the AC-side transformers connected in delta or in open WYE [143]. Protection engineers prefer to ground the WYE and use the ground current to detect the presence of phase faults in the MMC. From the algebraic formulas of [141], the 2^{nd} harmonic causes the even harmonics in the circulating current in $i_{diff}(j=a,b,c)$ and the 3^{rd} order harmonic in the AC currents.

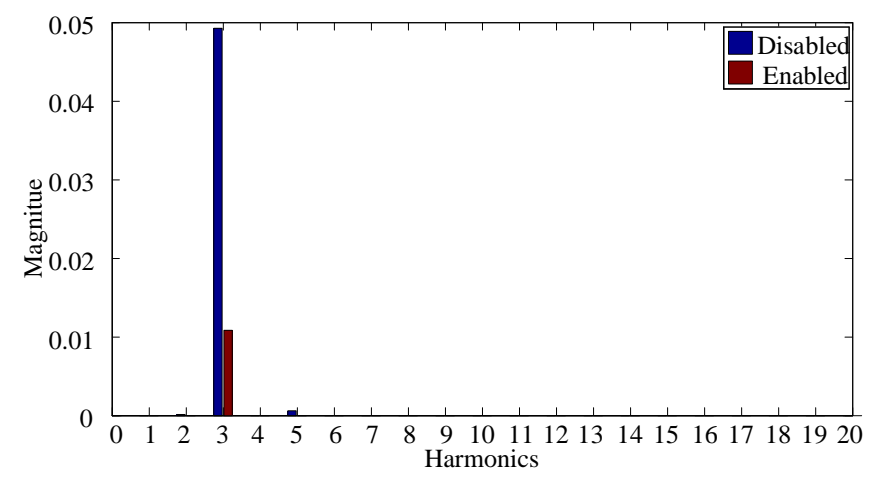


Fig. 3-10 FFT of phase-a AC currents when the AC-side transformers have a grounded WYE connection.

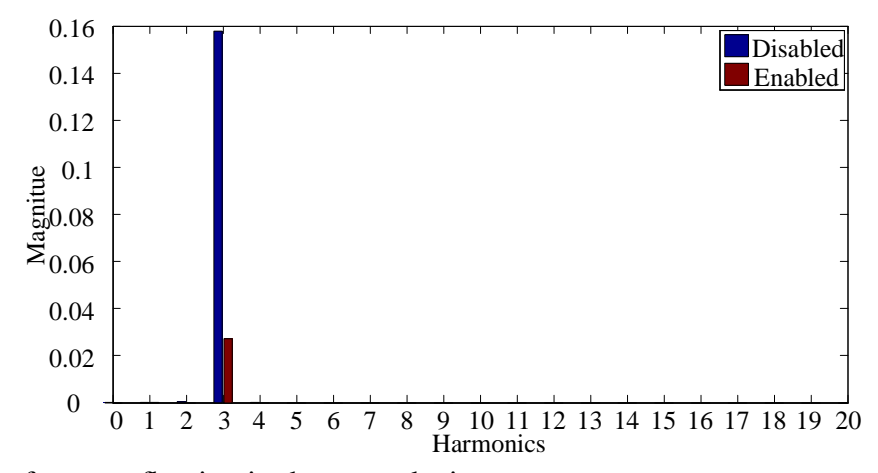


Fig. 3-11 FFT of current flowing in the ground wire.

In the simulation test, the neutral of the WYE of the AC-side transformers is grounded. As shown in Fig. 3-8 (a), the AC-currents indeed have a 3rd order harmonic distortion, giving rise to an unacceptable THD of 4.92%. Fig. 3-8 (b) shows that, with the CCSC reducing the circulating current, the 3rd order and odd harmonic distortion is mitigated. THD is 1.09%. Besides validating the innovative method, the simulation results of Fig.3-8 (b) validate the algebraic formulas of [141].

Fig. 3-9 shows the 3rd order harmonics current in the ground wire for: (a) without circulating current reduction; (b) with circulating current reduction. The magnitude of 3rd order harmonics decreases from 235A to 42A peak-to-peak after incorporating the circulating current reduction.

Fig. 3-10 shows the FFT analysis result of phase A when AC-side transformers have a grounded WYE connection. The blue bar constitutes the result without circulating current reduction while the red bar is enabled. The magnitude is divided by fundamental components

(50Hz) to per unit. The fundamental component is not presented as its magnitude is 1. In Fig. 3-10, the third-order harmonics (150 Hz) decreased from 0.05 to 0.01 after triggering the circulating current reduction.

Fig. 3-11 shows the FFT of the current flowing in the ground wire. The magnitude is divided by the rated value of the AC current to per unit. The 3rd order harmonics (150Hz) constitutes the predominant part. The magnitude of the 3rd order harmonics decreased from 0.16 to 0.03 after that circulating current reduction has been activated.

3.5 SM Capacitor Size Tests

3.5.1 Over-Voltage Tests

Considering overvoltage is important when choosing the voltage rating of IGBTs. In Fig. 3-7, the voltage across the IGBT in a sub-module reaches as high as 2230 V, although it is designed for an average voltage of 2000 V. The overvoltage is about 11.5 percent for the capacitor size of C=9mF. Designers need information such as the one given in Fig. 3-12, which posits the percentage overvoltage as a function of C for two cases: with (enabled) and without (disabled) circulating current reduction through the feedback.

For *C*=15 mF, the overvoltage is 3.25% in the disabled case, and 2.25 % in the enabled case. Without the feedback elimination, the overvoltage climbs to a resonant peak of 113.25% when *C* is reduced to around 6.5 mF. The overvoltage drops to around 20.75% at 5mF. The possibility of resonance has been predicted in [141]. With the feedback elimination, resonance does not exist and the overvoltage at 5 mF is about 10.5%.

3.5.2 Root Mean Square (RMS) Current Tests

IGBTs have to be rated so that the current flowing through them does not exceed the thermal limit. The thermal limit is based on the RMS value of (3-48) to (3-50), which consists of half of the AC current, one-third of the DC bus current and the circulating current flowing through the IGBT. The RMS of the AC current is plotted in Fig. 3-13 as a function of the capacitor size.

3.6 Model Validation Tests

In order to validate the proposed MMC ODE model, the Detail Equivalent Model (DEM) of the 3-phase MMC shown in Fig. 2-1 is simulated in the RT-LAB as the benchmark. In the simulations,

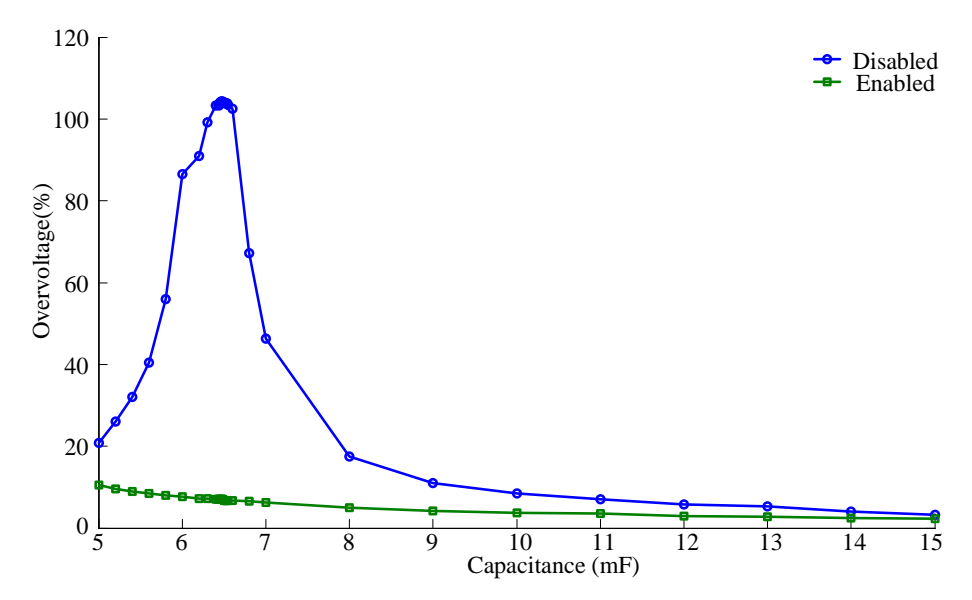


Fig. 3-12 Percentage Over-Voltage of the IGBT in the SM.

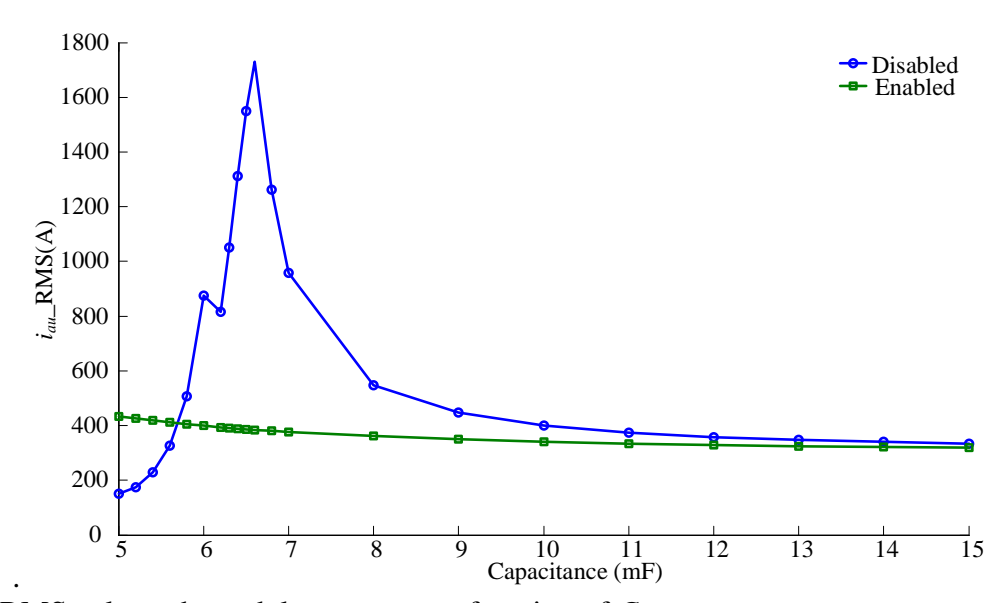


Fig. 3-13 RMS value sub-module current as a function of C.

NLM is used as the modulation method. The capacitor voltages in each individual SM are balanced by means of applying a sorting algorithm [17]. The parameters of the main circuit are shown in Table 3-II.

Fig.3-14 to Fig.3-19 present the simulation results of the MMC DEM and the ODE Model. The blue line stands for the results of the MMC DEM and the red dashed line shows the results of the MMC ODE model. The MMC ODE Model is simulated in the MATLAB/SIMULINK. The MMC DEM Model is simulated in the RT-LAB. The blue curves obtained from the DEM Model coincide with those from the MMC ODE Model, thus validating the correctness of the ODE model.

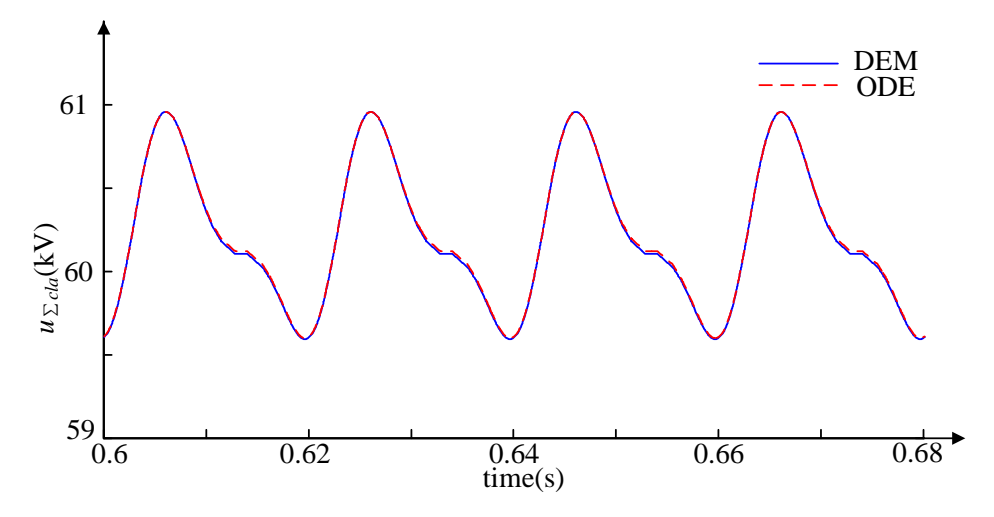


Fig. 3-14 Total capacitor voltage in the upper arm of the MMC phase-a

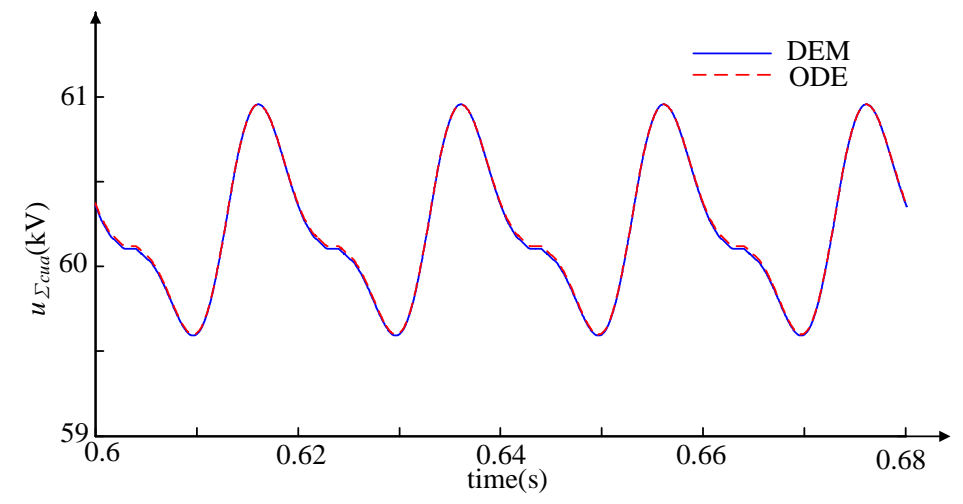


Fig. 3-15 Total capacitor voltage in the lower arm of the MMC phase-a

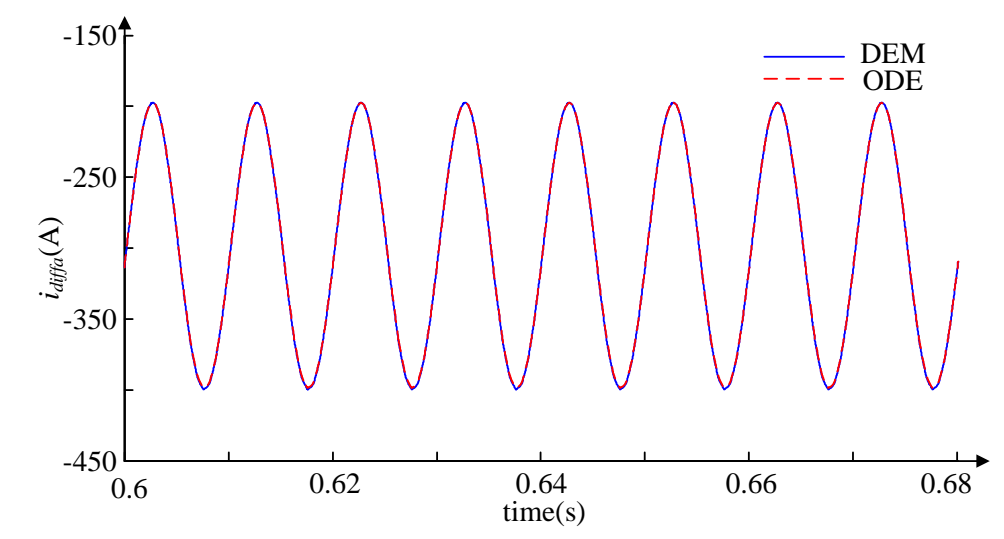


Fig. 3-16 Differential current of the MMC phase-a

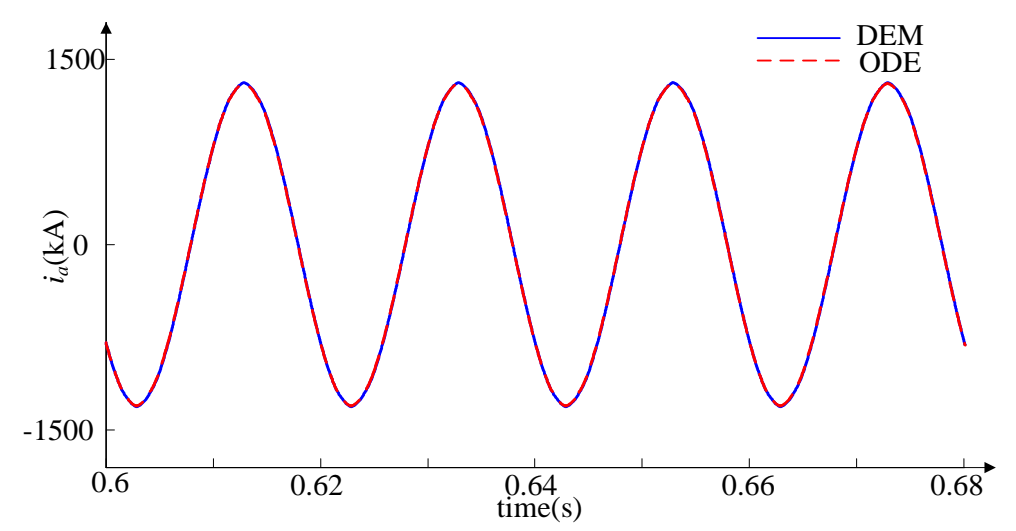


Fig. 3-17 AC current of the MMC phase-a

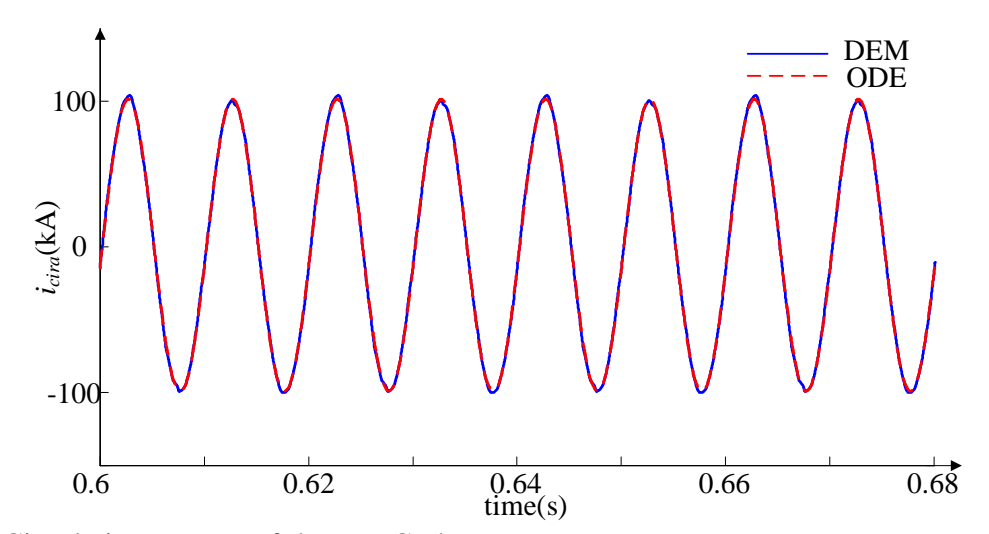


Fig. 3-18 Circulating current of the MMC phase-a

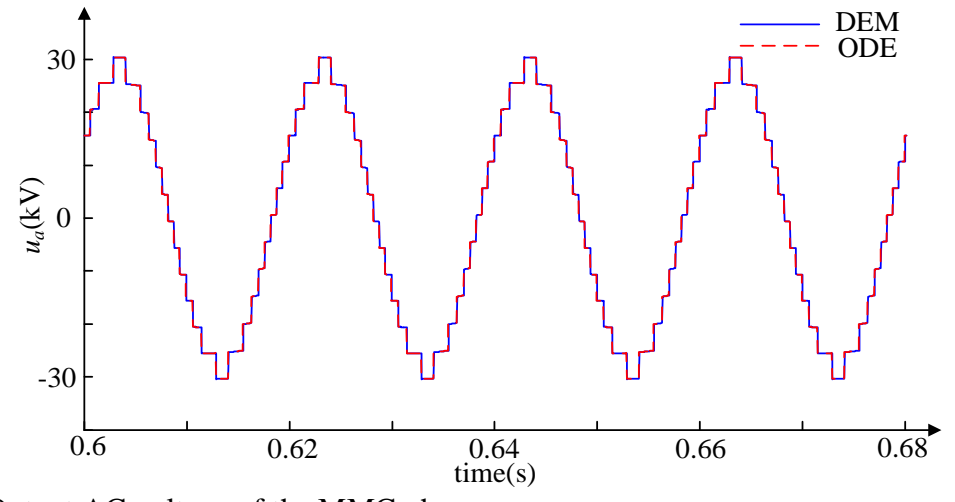


Fig. 3-19 Output AC voltage of the MMC phase-a

Table 3-II Parameters used in Model Validation Tests.

Parameters	Values			
DC Grid Voltage U_{dc}	60kV			
AC Grid Voltage	46kV			
Number of Sub-modules per Arm N	12			
Sub-module capacitor voltage u_c	5kV			
Arm Inductance L_m	5mH			
Arm Equivalent Resistance R_m	1.1Ω			
SM Capacitance C	18mF			
AC Equivalent Inductance L_{ac}	2mH			
AC Equivalent Resistance R_{ac}	0.1Ω			
Frequency f	50Hz			

Fig.3-14 to Fig. 3-17 present the comparison results of the four state variables $u_{\sum cua}$, $u_{\sum cla}$, i_{diffa} , i_a from (3-30) (3-33) (3-36) and (3-39). Fig. 3-18 shows the circulating current i_{cira} . Fig. 3-18 shows the circulating current which has dominant 2^{nd} order harmonics. Fig. 3-19 shows the output AC voltage u_a of MMC. In Fig. 3-19, the staircase waveforms are generated through the Nearest Level Modulation (NLM).

3.7 Chapter Summary

The Ordinary Differential Equation (ODE) Model of MMC with the Circulating Current Suppression Control (CCSC) is developed and validated in this chapter. The Capacitor Modulation Theory is introduced first to present the relationship between the total voltage and the time-varying capacitance of a string of capacitors. Based on the Capacitor Modulation Theory, a single-phase MMC ODE is proposed and has been extended to a three-phase MMC ODE Model. In order to reduce the inherent circulating current, a circulating current suppression control (CCSC) without the electronic/digital filter is developed. After applying the CCSC, the magnitude of the circulating current is reduced by 2500%. To further present the performance of the CCSC, the neutral of the WYE connection of the AC-side transformer is grounded. The effect of the size of the SM capacitor has been investigated. The results show that CCSC is capable of significantly reducing the 3rd order harmonics in the AC current and the RMS value of the arm current. The simulation

results from the MMC DEM Model (RT-LAB), shown in blue, and from the MMC ODE Model (MATLAB SIMULINK), shown in red, have been compared. The lines lie on top of each other. The coinciding lines prove the correctness of the MMC ODE model.

Chapter 4. Dynamic Characteristics Analysis of Modular Multilevel Converters

4.1 Introduction

The existing approach to system design is based on iterative tuning of circuit parameters. For Modular Multilevel Converters (MMC), repetitive simulation runs are very time-consuming. The design is seldom thorough because the waiting time of each iteration are long and tedious. In order to facilitate design, two useful techniques are introduced in this chapter: (1) the method of Aprille and Trick [133], by which the steady-state is solved within one period of 50 or 60 Hz, without having to wait for the transients to be damped out; (2) the Floquet-Lyapunov Theorem [134][135], by which graphs of the damping coefficients of the transients are computed to guide system designers to choose the best size of the circuit parameters.

The nonlinear and linearized model of the MMC is discussed. By linearizing the model of the MMC based on the ordinary differential equations developed in Chapter 3, a linearized time-varying periodic matrix [A(t)]=[A(t+T)] is obtained. The state-transition matrix $\Phi(T,0)$ of the periodic matrix [A(t)] is constructed, and the eigenvalues of $\Phi(T,0)$, where T equals to the period, are solved. With the availability of $\Phi(T,0)$, the method of Aprille and Trick [133] is then applied, which arrives at the steady-state solution in only one period of 50 or 60 Hz of the supply frequency. Therefore, it is no longer necessary to wait for transients to be damped out.

To guide system designers, graphs of the damping coefficients are plotted against the MMC circuit parameters to facilitate the choice for the best damping, and to avoid force-resonance. The damping coefficients represent the magnitudes of the eigenvalues of the state-transition matrix $\Phi(T,0)$ of the periodic linearized [A(t)]=[A(t+T)] matrix. The damping coefficients are plotted as functions of $(C_{arm}, L_{ac}, L_m, R_{ac})$ to guide the choice of parameters.

In this chapter, the nonlinear and linearized model of the MMC is discussed first. The results of the fast steady-state solutions of Aprille and Trick are presented in the second section. The graphs of damping coefficients as functions of MMC circuit parameters and how they are applied to guide designs are presented in the third section. The summary comes in the last section.

4.2 Nonlinear and Linearized Models of MMC

4.2.1 Nonlinear MMC ODE Model

The schematic of one MMC phase is shown in Fig. 3-1. (3-25) to (3-28) are the ODE equations of one-phase MMC. Based on (3-29), the ODE equations are written as:

$$\frac{d\underline{x}}{dt} = \underline{f}(\underline{x}, \underline{u}) \tag{4-1}$$

where $\underline{f}(\underline{x},\underline{u})$ is a 4-tuple nonlinear function of the vectors of state-variables \underline{x} and inputs \underline{u} . The 4 states of the ODE equations are $\underline{x} = [u_{\sum \alpha ua}, u_{\sum cla}, i_{diffa}, i_a]$.

4.2.2 Model Linearization

Linearization consists of defining $\underline{x} = \underline{X}_0(t) + \Delta \underline{x}$ where $\underline{X}_0(t)$ is the vector of steady-state solution and $\Delta \underline{x}$ is the vector of perturbation state-variables. Substituting $\underline{x} = \underline{X}_0(t) + \Delta \underline{x}$ in (4-1)

$$\frac{d\underline{X}_{o}(t)}{dt} + \frac{d\underline{\Delta x}}{dt} = \underline{f}(\underline{X}_{0}(t), \underline{u}_{0}(t)) + \frac{\partial \underline{f}(\underline{x}, \underline{u})}{\partial \underline{x}} \bigg|_{(X_{0}(t), u_{0}(t))} \underline{\Delta x} + \dots + \frac{\partial^{n} \underline{f}(\underline{x}, \underline{u})}{n!} \frac{\underline{\Delta x}^{n}}{\partial \underline{x}^{n}} \bigg|_{(X_{0}(t), u_{0}(t))} \underline{\Delta x}^{n}$$
(4-2)

where n=2,3,4...

In (4-2), because

$$\frac{dX_{0}(t)}{dt} = \underline{f}(X_{0}(t), \underline{u_{0}}(t))$$
(4-3)

According to ODE (3-25) to (3-28), for small Δx for $n \ge 2$, one assumes that

$$\frac{\partial^n \underline{f}(\underline{x},\underline{u})}{n!} \Big|_{(X_0(t),u_0(t))} = \underline{0}$$
(4-4)

Substituting(4-3), (4-4) in (4-2), what is left is the first-order term, which is the linearized equation:

$$\frac{d\Delta \underline{x}}{dt} = \frac{\partial \underline{f}(\underline{x}, \underline{u})}{\partial \underline{x}} \bigg|_{(X_0(t), u_0(t))} \Delta \underline{x} = [A(t)] \Delta \underline{x}$$
(4-5)

Although (4-1) to (4-5) follow the standard procedure of small perturbation linearization, an examination from (3-25) through (3-28) show that the nonlinearity is classified as bilinear. The product terms consist of the multiplication of state variables with forcing functions. A truly nonlinear function consists of multiplications of state-variables, for example, x_1^2 or x_1x_2 . Bilinearity means that there is no requirement for the perturbation vector $\Delta \underline{x}(t)$ to be small to apply linearity. In (4-4), the left side of the equation equals zero. There is no requirement that $\Delta x(t) \rightarrow 0$.

Since the 4 ordinary differential equations modeling its dynamic performance are (3-25) to (3-28), linearization based on (4-2) yields (4-5), where

$$[A(t)] = \begin{pmatrix} 0 & 0 & \frac{1}{C_{arm}} (\frac{1}{2} - \frac{u_{refa}}{U_{dc}}) & \frac{1}{2C_{arm}} (\frac{1}{2} - \frac{u_{refa}}{U_{dc}}) \\ 0 & 0 & \frac{N}{C_{arm}} (\frac{1}{2} + \frac{u_{refa}}{U_{dc}}) & -\frac{1}{2C_{arm}} (\frac{1}{2} + \frac{u_{refa}}{U_{dc}}) \\ -\frac{1}{2L_{m}} (\frac{1}{2} - \frac{u_{refa}}{U_{dc}}) & -\frac{1}{2L_{m}} (\frac{1}{2} + \frac{u_{refa}}{U_{dc}}) & -\frac{1}{2L_{m}} 2R_{m} & 0 \\ -\frac{1}{L_{eq}} (\frac{1}{4} - \frac{u_{refa}}{2U_{dc}}) & \frac{1}{L_{eq}} (\frac{1}{4} + \frac{u_{refa}}{2U_{dc}}) & 0 & -\frac{1}{L_{eq}} (R_{eq}) \end{pmatrix}$$

$$(4-6)$$

where
$$C_{arm} = \frac{C}{N}$$
, $L_{eq} = 0.5L_m + L_{ac}$, $R_{eq} = 0.5R_m + R_{ac}$

4.2.3 Periodic [A(t)]=[A(t+T)] Matrix

Because $u_{refa}(t)$ in (4-6) is periodic in T at 50Hz or 60Hz of the system frequency, it follows that [A(t)]=[A(t+T)].

After forming the linearized matrix, transient response is determined by the damping of the perturbation vector $\Delta \underline{x}(t)$ from the initial state $\Delta \underline{x}(0)$ at t=0. For asymptotic stability, it is required that $\|\Delta \underline{x}(t)\| \to 0$ when $t \to \infty$. For the periodic [A(t)]=[A(t+T)] matrix, there is no known analytical relationship between $\Delta \underline{x}(0)$ at t=0 with $\Delta \underline{x}(t)$ when $t\to \infty$.

4.2.4 State-Transition Matrix $\Phi(T,0)$.

For the linearized equation $\Delta \underline{\dot{x}}(t) = [A(t)]\Delta \underline{x}(t)$, the state transition matrix $\Phi(t,0)$ is constructed to enable $\Delta x(t)$ at time t to be related to its initial value $\Delta x(0)$ at t = 0. The relationship is through

$$\Delta \underline{x}(t) = [\Phi(t,0)] \Delta \underline{x}(0) \tag{4-7}$$

In general, $\Phi(t,0)$ consists of K columns of K-tuple vectors $\Delta x_n(t)$ (n=1,2...,K), as in:

$$\Phi(t,0) = [\Delta x_1(t) | \Delta x_2(t) | ... \Delta x_n(t) |,..., |\Delta x_K(t)]$$
(4-8)

As $\Delta \underline{x}(t)$ and $\Delta \underline{x}(0)$ are the solutions of $\Delta \underline{\dot{x}}(t) = [A(t)]\Delta \underline{x}(t)$, the $K \times K$ state-transition matrix $\Phi(t,0)$ satisfies

$$\frac{d[\Phi(t,0)]}{dt} = [A(t)][\Phi(0,0)] \tag{4-9}$$

When each column of (4-8) satisfies (4-9), it follows that $\Delta \dot{\underline{x}}(t) = [A(t)] \Delta \underline{x}(t)$ is satisfied because:

$$\frac{d[\Phi(t,0)]}{dt} = [A(t)\Delta \underline{x_1}(t)|...A(t)\Delta \underline{x_n}(t)|,...,|A(t)\Delta \underline{x_K}(t)]$$
(4-10)

Consider the initial state of the n^{th} column vector (written as a row to save space):

$$\Delta \underline{x}(0)^{T} = [0, 0, \dots 1_{nth-row}, \dots 0, 0]$$
(4-11)

Apply numerical integration of $\frac{d\Delta \underline{x}_n}{dt} = [A(t)]\Delta \underline{x}_n$ of the n^{th} column from initial the condition of (4-11) to time t=T.

The numerical solution takes the form

$$\Delta \underline{x}_n(t)^T = [\Delta x_{1n}, \Delta x_{2n}, ..., \Delta x_{Kn}]$$
(4-12)

Putting the columns of numerical solutions together

The relationship between $\Delta x(t)$ and the initial state $\Delta x(0)$ is

4.2.5 Dynamics of Discrete-Time System

This section shows that $\Delta x(t)$ and the initial state $\Delta x(0)$ are related by $\Phi(T,0)$ in

$$\Delta \underline{x}(t) = [\Phi(t, MT)][\Phi(T, 0)]^{M} \Delta \underline{x}(0)$$
(4-15)

Once $\Phi(T,0)$ is constructed, a property of the state transition matrix is given by (4-14).

When t=T

$$\Delta \underline{x}(T) = [\Phi(T,0)] \Delta \underline{x}(0) \tag{4-16}$$

For T < t < 2T, one can construct

$$\Delta \underline{x}(t) = [\Phi(t, T)] \Delta \underline{x}(T) \tag{4-17}$$

Substituting (4-16) in (4-17)

$$\Delta x(t) = [\Phi(t,T)][\Phi(T,0)]\Delta x(0) \tag{4-18}$$

Because of periodicity: A(t)=[A(t+T)]

$$[\Phi(MT, (M-1)T)] = ,..., = [\Phi(3T, 2T)] = [\Phi(2T, T)] = [\Phi(T, 0)]$$
 (4-19)

where M=0,1,2,3,..., positive integers.

For 2T < t < 3T

$$\Delta \underline{x}(t) = [\Phi(t, 2T)] \Delta \underline{x}(2T) = [\Phi(t, 2T)] [\Phi(2T, T)] \Delta \underline{x}(T)
= [\Phi(t, 2T)] [\Phi(2T, T)] [\Phi(T, 0)] \Delta x(0)$$
(4-20)

It follows from (4-19) and (4-20) that for MT < t < (M+1)T

$$\Delta x(t) = [\Phi(t, MT)][\Phi(MT, (M-1)T)]...[\Phi(3T, 2T)][\Phi(2T, T)][\Phi(T, 0)]\Delta x(0)$$
(4-21)

Therefore, for $MT \le t < (M+1)T$

$$\Delta \underline{x}(t) = [\Phi(t, MT)][\Phi(T, 0)]^{M} \Delta \underline{x}(0)$$
(4-22)

4.2.6 Asymptotic Stability Based on Geometric Series

For asymptotic stability, one requires $|\Delta \underline{x}(t)| \rightarrow 0$, when $t \rightarrow \infty$.

This is satisfied when

$$\|[\Phi(T,0)]^M\| \to 0 \text{ for } M \to \infty$$
 (4-23)

The state transition matrix $\Phi(T,0)$ can be diagonalized as

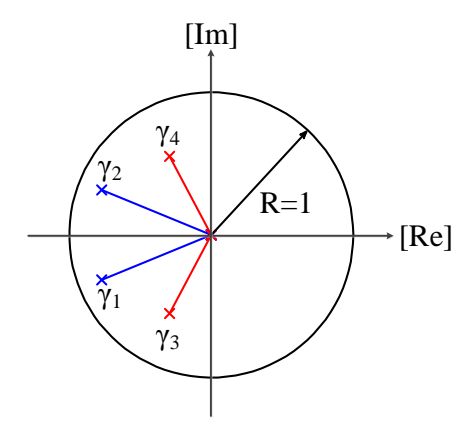


Fig. 4-1 Eigenvalues of $\Phi(T,0)$ and the unit circle

$$[\Phi(T,0)] = [S][\Gamma][S]^{-1} \tag{4-24}$$

where
$$[\Gamma] = \begin{bmatrix} \gamma_1 & & & \\ & \gamma_2 & & \\ & & \gamma_3 & \\ & & & \gamma_4 \end{bmatrix}$$
 (4-25)

It follows that

$$[\Phi(T,0)]^{M} = [S] \begin{bmatrix} (\gamma_{1})^{M} & & & & \\ & (\gamma_{2})^{M} & & & \\ & & (\gamma_{3})^{M} & & \\ & & & (\gamma_{4})^{M} \end{bmatrix} [S]^{-1}$$
 (4-26)

In general, $\gamma_k = |\gamma_k| e^{j\theta_k}$, as illustrated in Fig. 4-1. The magnitude of each arrow representing the phasor of γ_k is proportional to $|\gamma_k|$, and the angle made the real axis is θ_k . When the eigenvalues are complex, they come as conjugate pairs, making angles $+\theta_k$ and $-\theta_k$. When the eigenvalue is real, $\theta_k = 0$ or 2π . Although there is no known analytical relationship between at t = 0 with $\Delta \underline{x}(t)$ when $t \to \infty$, the dynamics of the periodically sampled perturbation states: $\Delta \underline{x}(0)$, $\Delta \underline{x}(T)$, $\Delta \underline{x}(2T)$, ..., $\Delta \underline{x}(MT)$ is determined by the eigenvalues $\gamma_k e^{j\theta_k}$, k=1,2,3,4 of $\Phi(T,0)$. Fig. 4-1 illustrates phasors representing two complex conjugate eigenvalue pairs (k=1, k=2) and (k=3, k=4) in the complex s-plane.

The magnitudes of the periodic samples of modes (k=1, k=2) or (k=3, k=4) are determined by the geometric series of $\gamma_k e^{j\theta_k}$, k=1,2,3,4. In order to be stable, $\gamma_k^M e^{jM\theta_k} \to 0$, and $\gamma_k^M e^{-jM\theta_k} \to 0$; for $M \to \infty$, it is required that all the eigenvalues of $\Phi(T,0)$ must lie within the unit circle shown in Fig. 4-1. The

magnitude is significant even though the system is stable, because a large value of γ_k indicates poor damping.

4.3 Fast Convergence to Steady-State by the Method of Aprille And Trick

In solving (4-1), if the initial value $\underline{x}(0)$ is guessed correctly; that is, equal to the steady-state value $\underline{X}_0(t)$, then numerical integration would immediately yield the correct steady-state value $\underline{x}(t) = \underline{X}_0(t)$ for $t \ge 0$. In general, this guess is wrong, and the waiting time for the transients to damp out is long. The method of Aprille and Trick shows that, once the state-transition matrix $\Phi(T,0)$ has been computed, $\underline{X}_0(t)$ can be reached in only one time period T out of a wrong guess. The theory of Aprille and Trick's method is described in the following paragraphs.

The method exploits periodicity in T. On numerically integrating (4-1) from an initial value $\underline{x}^i = \underline{\hat{x}}(0)$ to the end of the period $\underline{x}(t) = \underline{\hat{x}}(T)$, if, by luck, $\underline{\hat{x}}(0)$ is found to be equal to $\underline{\hat{x}}(T)$, the integration will yield the steady-state $X_0(t)$.

In general,

$$\underline{\hat{x}}(0) \neq \underline{\hat{x}}(T) \tag{4-27}$$

It is necessary to compensate for the wrong guess $\underline{\hat{x}}(0)$ by adding another algebraic unknown vector ξ to improve the guess

$$\underline{x}^{improve}(0) = \underline{\hat{x}}(0) + \underline{\xi} \tag{4-28}$$

Treating $\underline{\xi}$ as an initial state of (4-14), its value at t = T is $\Phi(T,0)\underline{\xi}$. Because of bilinearity, there is no requirement that $\underline{\xi}$ has to be small for linearity to hold. If the improved guess of the initial value is given by (4-28), at t=T,

$$\underline{x}(T) = \hat{\underline{x}}(T) + [\Phi(T,0)]\xi \tag{4-29}$$

Periodicity requires that $\underline{x}(T)$ of (4-29) is equal to the initial state $x^{improve}(0)$ of (4-28), that is

$$\underline{\hat{x}}(T) + [\Phi(T,0)]\underline{\xi} = \underline{\hat{x}}(0) + \underline{\xi}$$
(4-30)

Solving ξ from (4-30)

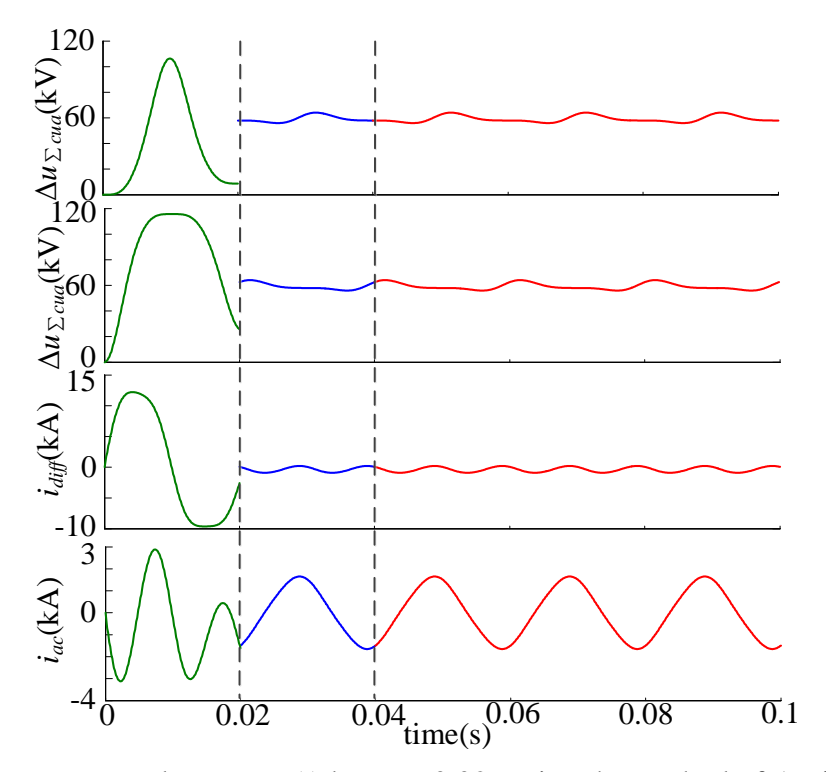


Fig. 4-2 Convergence to steady-state $\underline{X}_0(t)$ by t=T=0.02s using the method of Aprille and Trick

$$\xi = \{ [I] - [\Phi(T,0)] \}^{-1} [\underline{\hat{x}}(T) - \underline{\hat{x}}(0)]$$
 (4-31)

Writing $\underline{x}^i = \hat{\underline{x}}(0)$, substituting (4-31) in (4-28), the next initial value is

$$\underline{x}^{i+1} = \underline{x}^{i} + \{ [I] - [\Phi(T,0)] \}^{-1} [\hat{\underline{x}}(T) - \underline{x}^{i}]$$
 (4-32)

The algorithm has 2 steps:

Step 1) Step 1. From an initial value $\underline{x}^i = \hat{\underline{x}}(0)$, integrate (1) until at = T, $\hat{\underline{x}}(T)$ is reached.

Step 2) If $\|\hat{\underline{x}}(T) - \hat{\underline{x}}(0)\| \le \varepsilon$ (ε is set to e^{-10} in this paper), the iteration is stopped and the steady-state solution is obtained as $\hat{\underline{x}}(T)$. If $\|\hat{\underline{x}}(T) - \hat{\underline{x}}(0)\| > \varepsilon$, (4-32) is substituted as the next initial value until the steady-state solution is obtained.

The more general algorithm of Aprille and Trick [133] for proceeding from the i^{th} to $(i+1)^{th}$ iteration is

$$\underline{x}^{i+1}(0) = \{ [I] - [\Phi(T,0)]\underline{x}^{i}(0) \}^{-1} \{ \underline{x}^{i}(T) - [\Phi(T,0)]\underline{x}^{i}(0) \}$$
 (4-33)

Because of (4-4), there is no requirement that in (4-28), $\|\underline{\xi}\|$ has to be small to apply linearity. The computation required is up to time t=T, which occurs as soon as $\hat{\underline{x}}(T)$ is obtained from the numerical integration from any initial value $\hat{x}(0)$ of t=0.

To illustrate fast convergence to the steady-state of Aprille and Trick's method, the initial states of each phase are set to $\underline{x}(0) = [u_{\sum Cua}, u_{\sum Cla}, i_{diffa}, i_a]^T = [0, 0, 0, 0]^T$. Fig. 4-2 shows the simulations of $\underline{x}(t)$ for $t \geq 0$. The curves in green, blue, and red correspond to the first, second and later periods. It is found that $\|\Delta\underline{x}(T)-\Delta\underline{x}(2T)\| < e^{-10}$. According to the theory above, this implies that the correct steady-state solution $\underline{X_0}(t)$ is already found in t=0.02s=T. The convergence in only one period is a consequence of (4-4), which says that $\Delta\underline{x}(t)$ does not have to be small for linearity to be applied to (4-29).

4.4 Graphs of Damping Coefficients

This section presents the damping coefficients taken from the eigenvalues of $\Phi(T,0)$, and the state-transition matrix of the linearized [A(t)] matrix. Considering the discrete-time dynamics, the transients are examined in the sampled time, t=T, 2T, 3T,..., NT. At the N^{th} sample, the state transition matrix is $\Phi(T,0)^N$. There are 4 eigenvalues $(\gamma_k e^{j\theta_k}, k=1,2,3,4)$ with their magnitudes $(\gamma_k, k=1,2,3,4)$. In the sampled time, t=T, 2T, 3T,..., NT, the magnitudes change according to a geometric series: γ_k , $(\gamma_k)^2$, $(\gamma_k)^3$, ... $(\gamma_k)^N$. The system is stable when the magnitudes lie within the Unit Circle of Fig. 4-1, because $(\gamma_k)^N \to 0$ as $N \to \infty$. Fast damping corresponds to a low value in γ_k . The parameters used in the MMC tests are listed in Table 4-I.

The MMC designer begins with an initial set of parameters, that is, $(C'_{arm}=0.416\text{mF}, L'_{ac}=5\text{mH}, L'_{m}=5\text{mH}, R'_{ac}=0.1\Omega)$. Fig. 4-3 to Fig. 4-6 display the magnitudes of $(\gamma_k, k=1,2,3,4)$ as functions of parameters, centered around the initially chosen parameters. When eigenvalues are complex conjugates, their magnitudes are equal and the colour of one line is hidden by the other.

Poor damping corresponds to the damping coefficient close to 1.0. In each graph, the duration of a transient is determined by least damped eigenvalue (highest γ_k). The designer has to consider Fig. 4-3 to Fig. 4-6 together. The choice is the minimum of the (highest γ_k); from Fig. 4-3; C_{arm} is selected as 0.2mF; from Fig. 4-4 and Fig.4-5, L_{ac} is selected as 50mH and L_m is selected as 50mH. In Fig. 4-6, R_{ac} is selected as 0. From the choice, the design changes from the initial values ($C_{arm}^{'}$, $L_{ac}^{'}$, $L_{m}^{'}$, $R_{ac}^{'}$) to a new operating point ($C_{arm}^{''}$, $L_{ac}^{''}$, $L_{m}^{''}$, $R_{ac}^{''}$). A new set of figures similar to Fig. 4-3 to Fig. 4-6 can be constructed to guide the designer to ($C_{arm}^{'''}$, $L_{ac}^{'''}$, $L_{m}^{'''}$, $R_{ac}^{'''}$). The iterative design proceeds until his objective is met.

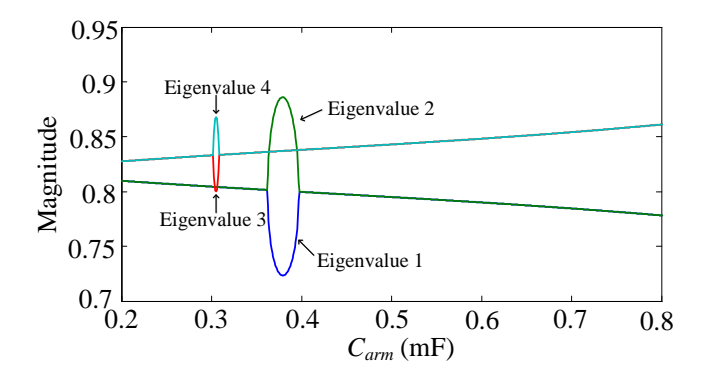


Fig. 4-3 Magnitude of Eigenvalue vs C_{arm} (L_{ac} =5mH, L_m =5mH, R_{ac} =0.1 Ω)

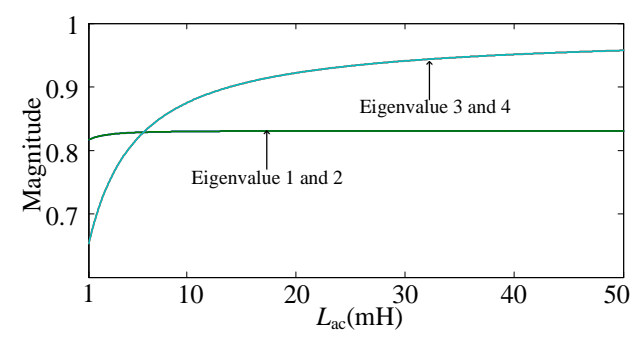


Fig. 4-4 Magnitude of Eigenvalues vs L_m (C_{arm} =0.4167mF/arm, L_{ac} =5mH, $\underline{R_{ac}}$ =0.1 Ω)

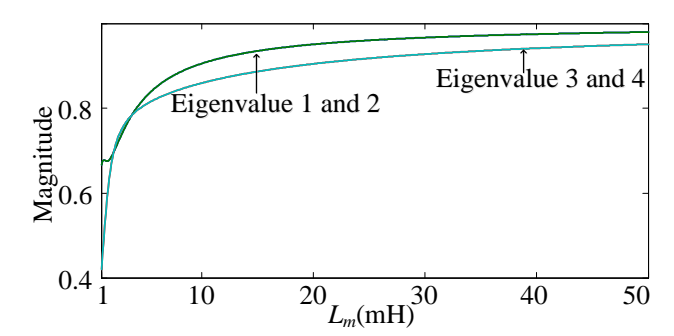


Fig. 4-5 Magnitude of Eigenvalues vs L_{ac} (C_{arm} =0.4167mF/arm, L_m =5mH, R_{ac} =0.1 Ω)

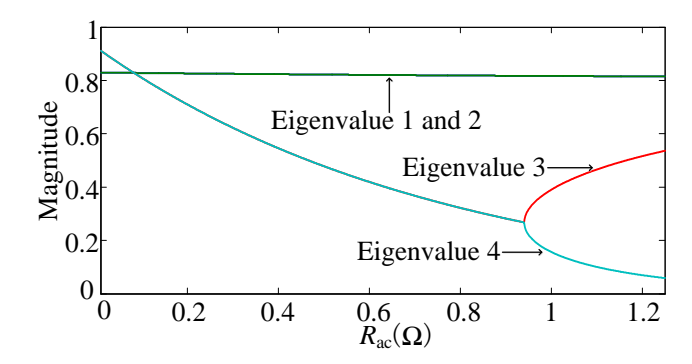


Fig. 4-6 Magnitude of Eigenvalues vs R_{ac} ($C_{arm} = 0.4167 \text{mF/arm}$, $L_{ac} = 5 \text{mH}$, $L_m = 5 \text{mH}$)

Table 4-I Parameters used in MMC Dynamic Characteristics Tests

Symbol	Quantity	Values
$U_{ m DC}$	DC Voltage	60kV
N	Numbers of SMs per Arm N	12
U_m	SM Capacitor Voltage	5kV
R_m	Arm Equivalent Resistance	0.05Ω
L_m	Arm Inductance	5mH
C	SM Capacitance	5mF
C_{arm}	Arm Equivalent Capacitancec (C/N)	0.4167mF/arm
L_{ac}	AC System Inductance	5mH
R_{ac}	AC System Resistance	1.25Ω
arphi	power angle	9.7°
$v_{ m ac}$	Grid Voltage (magnitude)	30.6kV

4.4.1 Validation of Method

The benchmark used in validation of the method consists of the simulations of (4-1), which are graphically coloured blue. The Floquet-Lyapunov Theorem takes the method to the eigenvalues $\gamma_k e^{j\theta_k}$ and $\gamma_k e^{-j\theta_k}$ of the state-transition matrix. Their predictions are graphed as periodic sample values in the form of red bars. Validation consists of showing that the blue benchmark simulations touch the periodic red bars.

For clarity in the validation, the technique of exciting only one selected eigen-mode at a time is implemented. The eigenfunction software which computes the eigenvalues γ_k , k=1,2,3,4 of $\Phi(T,0)$ also computes the eigenvectors $\underline{p}_k + j\underline{q}_k$, k=1,2,3,4. The k^{th} mode is exclusively excited by the initial condition $\underline{x}(0) = a\underline{p}_k + b\underline{q}_k$, where a and b are scalars chosen to determine the size of the transient.

In Fig. 4-3 to 4-6, there are graphs where two eigenvalues are depicted as a single line. The single line represents the magnitude of the complex conjugate eigenvalues $\gamma_k e^{j\theta_k}$ and $\gamma_k e^{-j\theta_k}$. The M^{th} periodic sample $\Delta \underline{x}_{1,2}(M)$ of the (γ_1, γ_2) mode take the form:

$$\Delta \underline{x}_{1,2}(M) = G_{1,2} \gamma_1^M \cos M \theta_1, M = 1, 2, 3... \tag{4-34}$$

The M^{th} periodic samples of the (γ_3, γ_4) mode take the form

$$\Delta \underline{x}_{3,4}(M) = G_{3,4} \gamma_3^M \cos M \theta_3, M = 1, 2, 3... \tag{4-35}$$

where $G_{1,2}$ and $G_{3,4}$ are proportionality constants, M is a positive integer.

Fig. 4-7 shows an example of exciting exclusively mode $\gamma_{1,2} = -0.4608 \pm j0.6627$. The red bars consist of periodic samples of the state variable $u_{\sum cua}$ taken from (4-34). The blue line shows the solution of $\Delta \underline{x}(t) = \underline{x}(t) - \underline{X}_0(t)$, where $\underline{x}(t)$ is obtained from the simulation of (4-1). The red lines show the periodic samples of γ_k whose tips touch the blue line, thus validating the theory. The red lines change polarity because $cosM\theta$ changes the polarity sign in $M\theta$, M=1,2,3... The important conclusion is that the magnitude γ_k determines how quickly the transient is damped out. The procedure for generating an exclusive mode, such as Fig. 4-7, Fig. 4-8 and Fig. 4-9, is through the following steps:

- 1) Solve the steady-state $\underline{X}_0(t)$ using the method of Aprille and Trick, and keep $\underline{X}_0(t)$ in memory.
- 2) Choose the initial time t = 0, where $\underline{X}_0(0) = \underline{X}_0(T)$. In order to excite the k^{th} mode exclusively, choose an initial value

$$\underline{x}(0) = \underline{X}_0(0) + a\underline{p}_k + b\underline{q}_k \tag{4-36}$$

and solve (4-1), which consists of (3-25) through (3-28). The solution is x(t) for t>0.

3) The exclusively excited mode is:

$$\Delta \underline{x}_{\iota}(t) = \underline{x}(t) - \underline{X}_{\circ}(t) \tag{4-37}$$

where
$$\Delta \underline{x}_k(t) = \left[u_{\sum cua,k}(t), u_{\sum cla,k}(t), i_{diff,k}(t), i_{a,k}(t)\right]^T$$
 (4-38)

The solid line in Fig. 4-7, Fig 4-8 and Fig 4-9 are displays of (4-38). The red lines are $\Delta \underline{x}(0), \Delta \underline{x}(T), \Delta \underline{x}(2T), ..., \Delta \underline{x}(MT)$, obtained from (4-22), which is

$$\Delta \underline{x}(MT) = [\Phi(T,0)]^{M} \Delta \underline{x}(0) \tag{4-39}$$

Fig. 4-8 shows the case of γ_I =0.837, which belongs to the bifurcated region in Fig. 4-3. There is no imaginary part to the eigenvalue. Thus, there is no oscillation on the red bars.

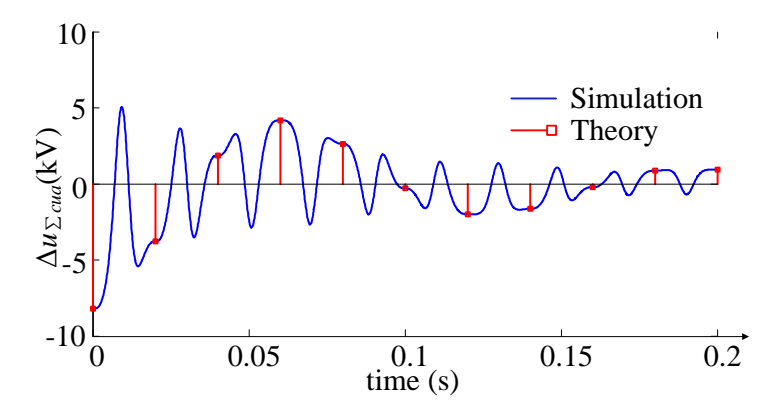


Fig. 4-7 Complex Mode $\gamma_{1,2} = -0.4608 \pm j0.6627 (C_{arm} = 0.25 \text{mF/arm})$

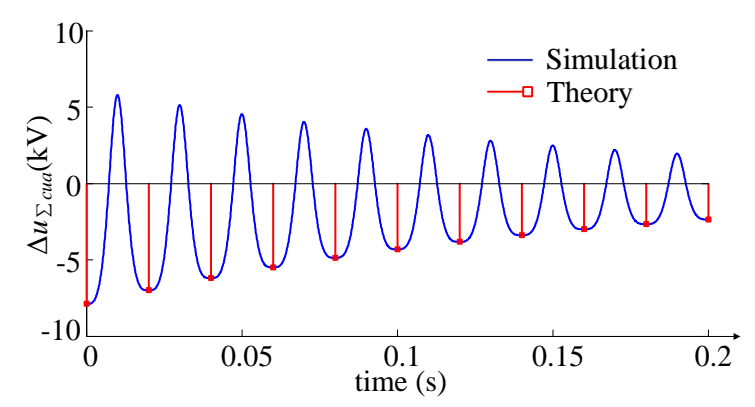


Fig. 4-8 Mode of $\gamma_1 = 0.8371$ ($C_{arm} = 0.379$ mF/arm)

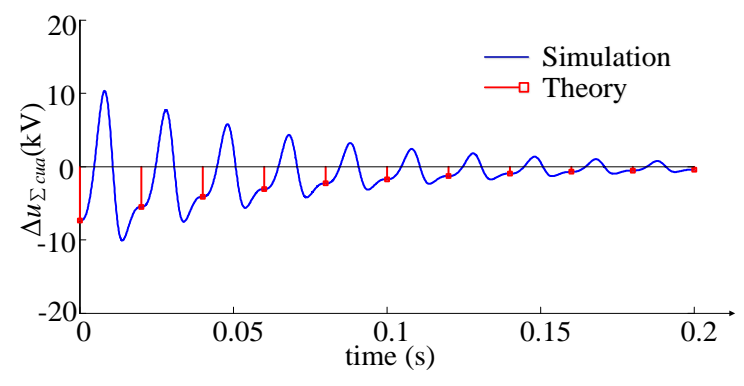


Fig. 4-9 Mode of $\gamma_2 = 0.7478 (C_{arm} = 0.367 \text{mF/arm})$

Fig. 4-9 shows the case of γ_2 =0.748, which, again, belongs to the bifurcated region in Fig. 4-3. As there is no imaginary part to the eigenvalue, there is no oscillation on the red bars.

The graphical agreement in Fig. 4-7 to Fig. 4-9 is very strong proof for the correctness of the method.

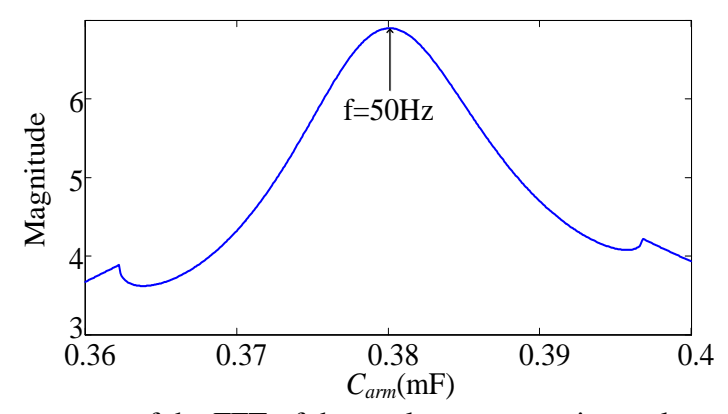


Fig. 4-10 50-Hz measurement of the FFT of the total upper capacitor voltage $u_{\Sigma cua}$

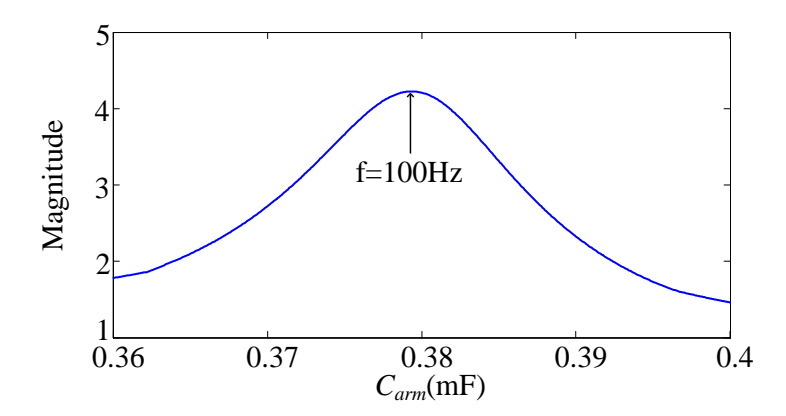


Fig. 4-11 100-Hz measurement of the FFT of the total upper capacitor voltage $u_{\Sigma cua}$

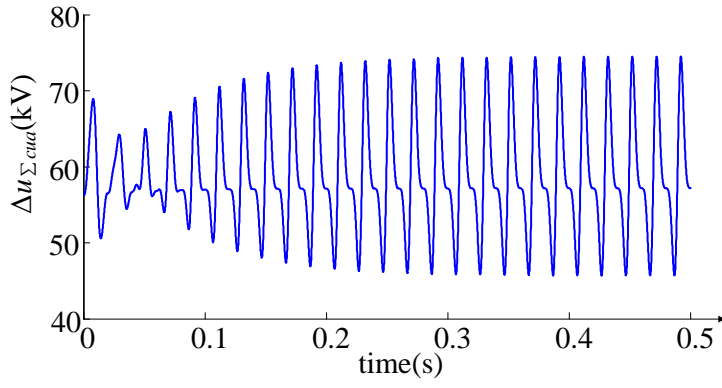


Fig.4-12 Upper arm voltage $u_{\sum cua}$ showing force-resonance because C/N is chosen around peaks of Fig. 4-10 and Fig.4-11

4.4.2 Bifurcated Regions

Fig. 4-3 and Fig. 4-6 show bifurcated regions where single lines divide into two. One way to understand its occurrence is to remember that eigenvalues are the same as poles of a transfer

function. In the method where partial fractions are used to find the poles, the denominator of the partial fraction takes the form $aS^2 + bS + c$. When $b^2 - 4ac > 0$, the poles are real and take two values: $\frac{-b+\sqrt{b^2-4ac}}{2a}$ and $\frac{-b-\sqrt{b^2-4ac}}{2a}$. For example, when the line of the (γ_1, γ_2) mode divides into two, the periodic samples are:

$$\Delta x_1(M) = G_1 \gamma_1^M, M = 1, 2, 3...$$
 (4-40)

and
$$\Delta x_2(M) = G_2 \gamma_2^M, M = 1, 2, 3...$$
 (4-41)

where G_I and G_2 are proportionality constants. There is no oscillation in the periodic samples. Fig. 4-10 and Fig. 4-11 show $u_{\sum cua}$ when the modes of $\gamma_1 = 0.8371$, and $\gamma_2 = 0.7478$ are exclusively excited, respectively.

Unlike Fig. 4-7, the red lines in Fig. 4-8 and Fig. 4-9 do not change polarity. Fig. 4-8 is lightly damped because $\gamma_1 = \left| \frac{-b + \sqrt{b^2 - 4ac}}{2a} \right|$, and Fig. 4-9 is slightly more heavily damped because $\gamma_2 = \left| \frac{-b - \sqrt{b^2 - 4ac}}{2a} \right|$. As the overall damping is determined by the lightly damped mode, the bifurcated region is to be avoided if improving the damping is the goal.

The bifurcated region occurs because $cosM\theta = 1$. It corresponds to $m\theta = 2m\pi$ or 0, where m is an integer. In the complex plane of Fig. 4-1, there is an angle θ of the complex phasors representing the eigenvalues. The phasors of the bifurcated region with the angle $M\theta$ are aligned along the positive real axis.

Inspection of the waveforms of Fig. 4-8 and Fig. 4-9, which is confirmed by FFT measurements, reveals that 50, 100, 150 Hz, and higher harmonics are present in $\Delta \underline{x}(t)$. This has led the authors to investigate the FFT of the exclusively excited modes for C_{arm} between 0.36 and 0.39 mF in Fig. 4-3. Fig. 4-10 and Fig. 4-11 show that the magnitudes of the FFT of 50Hz and 100 Hz of eigenvalue 1 display resonance characteristics.

The resonance characteristics in Fig. 4-10 and Fig.4-11 can give rise to force-resonance, causing overvoltage across the sub-modules which exceed the rating of the IGBTs. To confirm this possibility, (4-1) has been numerically integrated with C_{arm} set around the resonance peaks. Fig. 4-12 shows the upper capacitor voltage $u_{\sum cua}$. Whereas initial transients are damped out, as illustrated in Fig. 4-7 to Fig. 4-9, the force-resonance causes the voltage magnitude to build up

from 60 kV (design value) to about 74 kV at a steady-state. Therefore, the bifurcated regions are to be avoided because they constitute regions where forced-resonance can occur.

[141] shows that the second harmonic of single-phase AC power causes a harmonic voltage proliferation to dc, f_0 , $2f_0$, $3f_0$, ..., mf_0 , m=1,2,3... in the MMC. The frequency proliferation appears in the bifurcated regions. Further investigations conducted by the authors, addressing bifurcated regions of another parameter combination, confirm that dc, f_0 , $2f_0$, $3f_0$, ..., mf_0 are present in FFT measurements.

4.5 Chapter Summary

This chapter introduces two useful analytical techniques: (1) the method of Aprille and Trick, by which the steady-state is solved within one period of 50 or 60 Hz, without having to wait for transients to be damped out; (2) the Floquet-Lyapunov Theorem, by which graphs of the damping coefficients of transients are computed to guide system designers in choosing the best size of circuit parameters. Implementation of the two techniques follows the steps: (a) modeling MMC by ordinary differential equations (ODE); (b) linearization of the ODE equations to yield the linearized timevarying periodic matrix; (c) construction of the state transition matrix of the periodic matrix; (d) solving the eigenvalues of the state transition matrix which contain the damping coefficients; (e) graphing the damping coefficients against MMC circuit parameters to facilitate the choice for the best damping, and to avoid force-resonance.

Chapter 5. Hybrid AC-DC Platform Using MMC-HVDC Based on the ODE Model

5.1 Introduction

Power system engineers require accurate and fast digital simulation platforms for design, operation and planning studies on large hybrid (AC-DC) grids. Because of the low loss, the DC grids will be based on modular multilevel converters based high-voltage direct current (MMC-HVDC) system in the foreseeable future. Super-grids, with the MMC serving as the transmission backbone of the future, have already been proposed [144]. Super-grids will be a hybrid grid with the AC network interconnected with the DC network of MMC stations.

Firstly, it is necessary to address the issue of the simulation platform's accuracy. The proposed multi-terminal MMC-HVDC (MTDC-MMC) is based on extending the ODE model suggested in Chapter 3. Second in importance is the simulation speed. It is well known that the simulation according to the DEM(Detail Equivalent Model) of the MMC is computationally intensive. Well-funded research groups make use of parallel computation in RTDS, OPAL-RT, HYPERSIM, etc., to accelerate simulations. As the system dimension increases, the number of parallel CPUs increases as well. Platforms that serve high dimension multi-terminal MMC-HVDC will be costly. As a super-grid may have several MTDC-MMC lines, the high system dimension requires an examination if there is a limit to using parallel central processing units (CPUs). This limit is due to the time that is required to pass the simulation result of each integration step from one processor to another. From past experience with regard to using the Krylov cluster in a supercomputer [145], speedup met with diminishing returns after 40 to 80 CPUs were used in parallel computation. The theoretical speedup limit comes under Amdahl's Law [146]. Supercomputers can have speedup when using the ODE model.

Research on the hybrid AC-DC platform for super-grid begins in this chapter by considering a modest-sized DC grid with four-terminal MMC-HVDC stations simulated according to the ordinary differential equation (ODE) model. The simulation results from a single MMC station in

chapter 3 has shown the accuracy of MMC ODE model when compared to the Detail Equivalent Model (DEM) in RT-LAB. In order to solve the power system equations, an inductance matrix has to be inverted. This chapter introduces a simple stray capacitor technique [147], which enables the MMC stations to be decoupled without that inversion poses.

This chapter presents multiple control features: (i) coordinating the 4 MMC-HVDC stations to operate harmoniously as Power Dispatchers, DC Voltage Regulator, infinite AC bus controller to receive stochastic power from wind farm, (ii) circulating currents suppression control. The multiple controls are implemented using the modulation signal in the standard MMC command for the upper and the lower arms.

In order to compare the model's accuracy and simulation speed, the four-terminal MMC-HVDC systems based on the ODE models and the DEM are simulated by the same software with RT-LAB. Simulation results show that the ODE model is 10 times faster than the DEM model without losing accuracy.

This chapter is organized as follows: Section 5.2 presents the multi-terminal MMC-HVDC based on the ODE model. Section 5.3 presents the Stray Capacitor Technique to integrate multiple units of the MMC-HVDC connected by their DC sides, and it describes how they are integrated by assigning them the roles of power dispatcher and DC voltage regulator. Section 5.4 describes specific functional controls: acquire stochastic power of renewable power technologies; and, implement circulating currents suppression control. Section 5.5 illustrates the simulation results.

5.2 Multiterminal MMC-HVDC System Based on ODE Model

The radial four-terminal MMC-HVDC system of Fig. 5-1 is presented as a benchmark for MTDC-MMC-HVDC research.

In this chapter, the subscripts j stands for the phase-j, where j=a, b, c and the subscripts n or n stand for the MMC station number, where n=1,2,3,4. Fig.5-2 shows phase-j (j=a, b, c) of the nth(n=1,2,3,4) MMC-HVDC station. u_{$\sum cuj$ -n} and u_{$\sum clj$ -n} are defined to represent the sum of the total capacitor voltages in the upper and lower arms of phase-j for the nth MMC, respectively. u_{uj-n} and u_{lj-n} denote the total inserted capacitor voltage of the upper and the lower arm, respectively. n_{uj-n} and n_{lj-n} symbolize the total number of inserted SMs in the upper and lower arms, which are decided by the modulation signals m_{uj-n} and m_{lj-n}.

When looking at (3-10) and (3-11), the commands of the upper and lower arms of the j^{th} phase of the n^{th} MMC station are:

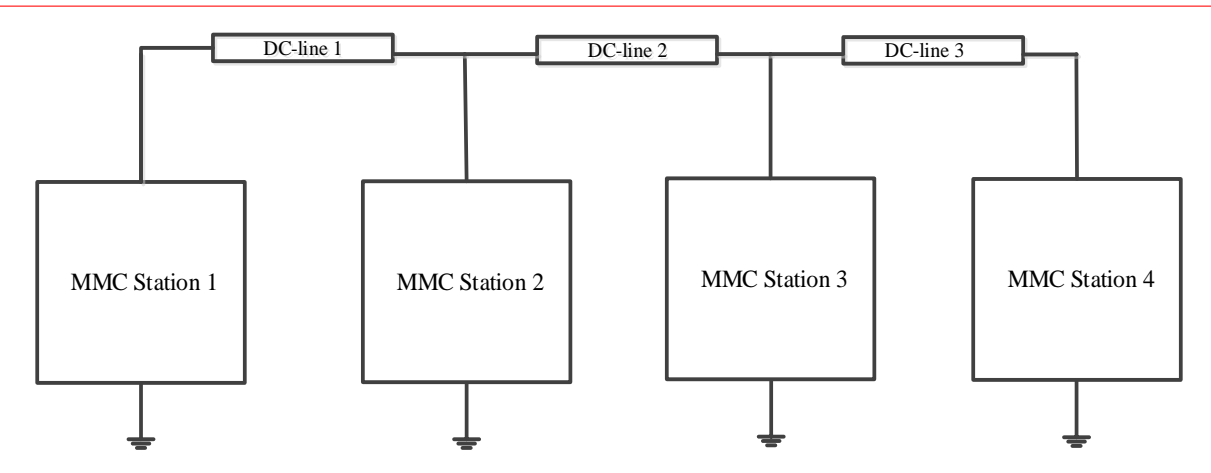


Fig. 5-1 Radial Multi-Terminal MMC Stations *n*=1,2,3,4

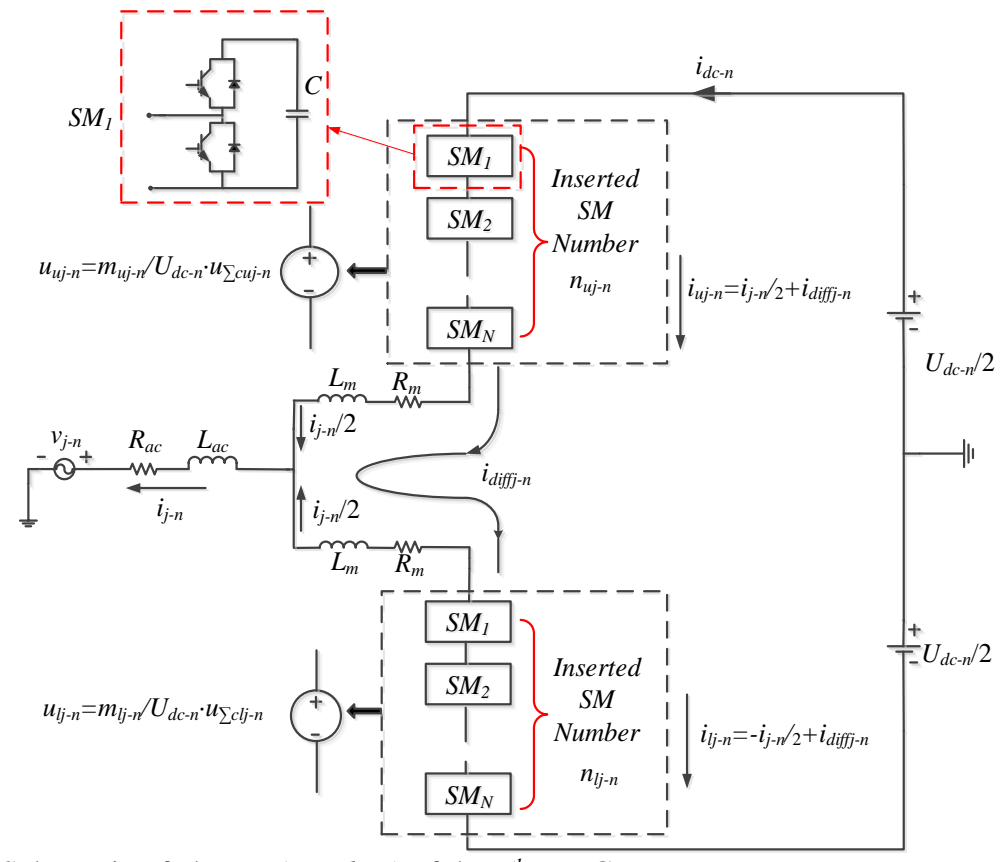


Fig. 5-2 Schematic of phase-j (j=a, b, c) of the n^{th} MMC

$$m_{uj-n} = \left(\frac{1}{2} - \frac{u_{refj-n}}{U_{dc-n}}\right) \cdot U_{dc-n}$$
 (5-1)

$$m_{lj-n} = \left(\frac{1}{2} + \frac{u_{refj-n}}{U_{dc-n}}\right) \cdot U_{dc-n}$$
 (5-2)

Referring from (3-42) to (3-44), the modulating reference signals for the upper and lower arms of phase-i of the n^{th} MMC station are

$$u_{refj-n} = M_n \cos(\omega_0 t - (\ell - 1) \times \frac{2}{3} \pi + \delta_{R-n})$$
 (5-3)

where $\ell=1,2,3$ corresponding to j=a,b,c, respectively. ω_0 is the angular frequency, and δ_{R-n} is the voltage control angle for the nth MMC station (n=1,2,3,4). M_n is the voltage amplitude.

Substituting(5-3) to (5-1) and (5-2), the commands for the upper and lower arms of the j^{th} phase of the nth MMC station are

$$m_{uj-n} = \left(\frac{1}{2} - \frac{M_n \cos(\omega_0 t - (\ell - 1) \times \frac{2}{3} \pi + \delta_{R-n})}{U_{dc-n}}\right) \cdot U_{dc-n}$$
 (5-4)

$$m_{lj-n} = \left(\frac{1}{2} - \frac{M_n \cos(\omega_0 t - (\ell - 1) \times \frac{2}{3} \pi + \delta_{R-n})}{U_{dc-n}}\right) \cdot U_{dc-n}$$
 (5-5)

The modulation reference signals $m_{uj-n}(t)$ and $m_{lj-n}(t)$ connect $n_{uj-n}(t)$ and $n_{lj-n}(t)$ capacitors (each of size C) in series strings as illustrated in Fig. 5-2. The currents i_{uj-n} and i_{lj-n} charge the capacitors of sizes $C/n_{uj-n}(t)$ and $C/n_{lj-n}(t)$ in the upper and lower string. The upper arm voltage $u_{\sum cuj-n}$, and the lower arm voltage $u_{\sum clj-n}$ consist of the sum of the voltage across each sub-module in the strings. The voltages $u_{\sum cuj-n}$ and $u_{\sum cuj-n}$ are charged by (5-6) and (5-7), respectively.

$$\frac{du_{\sum cuj-n}}{dt} = \frac{1}{C_{arm}} \left(\frac{i_{j-n}}{2} + i_{diffj-n} \right) \left(\frac{1}{2} - \frac{u_{reff-n}}{U_{dc-n}} \right)$$
 (5-6)

$$\frac{du_{\sum cuj-n}}{dt} = \frac{1}{C_{arm}} \left(-\frac{i_{j-n}}{2} + i_{diff-n} \right) \left(\frac{1}{2} + \frac{u_{reff-n}}{U_{dc-n}} \right)$$
 (5-7)

where $C_{\text{arm}} = C/N$ and N is the total number of sub-modules in each arm.

From Kirchhoff's Voltage Law along the branches containing $i_{diffj-n}$ and i_{j-n} , their differential equations are

$$\frac{di_{j-n}}{dt} = \frac{1}{\left(\frac{1}{2}L_m + L_{ac}\right)} \left[\left(\frac{1}{4} + \frac{u_{refj-n}}{2U_{dc-n}}\right) u_{\sum clj-n} - \left(\frac{1}{4} - \frac{u_{refj-n}}{2U_{dc-n}}\right) \cdot u_{\sum cuj-n} - \left(\frac{1}{2}R_m + R_{ac}\right) i_{j-n} - v_{j-n} \right] (5-8)$$

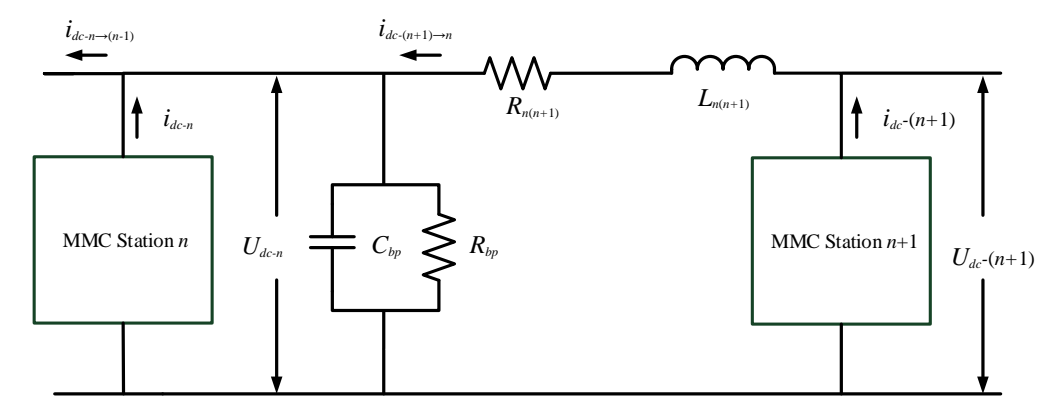


Fig. 5-3 Application of voltage of Stray Capacitor Method for Station $n \ (n \neq 2)$

$$\frac{di_{diffj-n}}{dt} = \frac{1}{2L_m} \left[U_{dc-n} - \left(\frac{1}{2} + \frac{u_{refj-n}}{U_{dc-n}} \right) u_{\sum clj-n} - \left(\frac{1}{2} - \frac{u_{refj-n}}{U_{dc-n}} \right) \cdot u_{\sum cuj-n} - 2R_m i_{diffj-n} \right]$$
(5-9)

Twelve ODEs (4 for each of the 3-phases) are applied to the simulations of each of the 4 MMC HVDC stations of Fig. 5-1.

5.3 Integrating Multi-Terminal MMC-HVDC

5.3.1 Stray Capacitor Technique

As illustrated in Fig. 5-3, the DC line is modeled by an inductance $L_{n(n+1)}$ and a resistance $R_{n(n+1)}$ between the n^{th} and the $(n+1)^{th}$ MMC stations. To obtain the first-order standard form suitable for numerical integration, the stray capacitor technique of [147][148] is used. A stray capacitor C_{bp} (with damping resistor R_{bp}) is placed in shunt across the n^{th} MMC station. The voltage across C_{bp} is a state variable. There is no inductance matrix to be inverted in order to formulate first-order standard form suitable for numerical integration.

 C_{bp} is very small in nature. In the simulation, the size should be big enough so that very small simulation step-size does not have to be used. However, C_{bp} must be sufficiently small so as not to cause inaccuracy.

5.3.2 Modulation Signal Control by M and δ_R

The MMC control of this chapter is structured after the voltage source converter (VSC) control of [53]. Active power P of an AC line is:

$$P = \frac{V^2}{X}\sin(\delta_S - \delta_R) \tag{5-10}$$

where δ_S and δ_R are, respectively, the voltage angles of the sending-end and the receiving-end of a transmission line whose reactance is X (resistance is neglected). Extensive research since [53] shows that it is sufficient to have two kinds of stations: power dispatchers, and the DC voltage regulators which operate the multi-terminal VSC-HVDC.

5.3.2.1 Multi-terminal VSC-HVDC

5.3.2.1.1 Power Dispatcher

For a power dispatcher, active power admitted to the VSC is measured and compared with the reference setting P_{ref} . The error (after passing through a P-I gain block) is applied to the receivingend angle δ_R to put the error to zero through a negative feedback. Based on (5-10), active power is drawn from the AC-side to satisfy the power reference P_{ref} .

5.3.2.1.2 DC Voltage Regulator

The voltage across the DC terminals is measured and compared with the reference $V_{dc\text{-}ref}$. The error (after passing through a P-I gain block) is applied to the receiving-end angle δ_R to put the error to zero through a negative feedback. Based on (5-10), active power is drawn from the AC-side to charge the DC-side to maintain the reference voltage $V_{dc\text{-}ref}$.

5.3.2.2 MTDC-MMC-HVDC

The control of the MMC is achieved through the commands of (5-1) and (5-2) of the f^{th} phase of the n^{th} station. The power dispatcher and the DC voltage regulator control the angle δ_{R-n} to reach P_{ref} and V_{dc-ref} .

5.3.2.3 AC Voltage Control

The terminal AC voltages are measured and compared to the AC voltage reference. The error after passing through a P-I block is applied to the magnitude M_n in (5-3).

5.4 Control of Multi-Terminal MMC-HVDC Platform

In the test system of Fig.5-1, the MMC1 and the MMC4 are assigned the role of power dispatchers. The MMC3 is connected to a stochastic power source. The MMC2 is assigned the role of the DC voltage regulator.

5.4.1 DC Voltage Regulator

The DC voltage regulator is the power slack which ensures power balance in the DC bus:

$$P_2 = -P_{\Sigma}, \quad P_{\Sigma} = [P_1 + P_3 + P_4] + \text{ohmic loss}$$
 (5-11)

The DC Voltage Regulator can be used for trading in collaboration with the Power Dispatchers.

5.4.2 Station to Receive Stochastic Power

Renewable energy technology is exemplified by wind farms. From experience gained in research on double-fed induction generators (DFIGs) [149][150], the MMC station is controlled to operate as an infinite AC bus. It has the features of an ideal voltage source supplying 3-phase AC voltages of constant magnitude and constant frequency to the DFIGs. As infinite AC bus, the MMC station accepts stochastic wind power sent by the DFIGs. Therefore, the upper and lower modulating signals are (5-12) and (5-13)

$$m_{uj-n} = \left(\frac{1}{2} - \frac{M_n \cos(\omega_0 t - (\ell - 1) \times \frac{2}{3} \pi + \delta_{R-n})}{U_{dc-n}}\right) \cdot U_{dc-n}$$
 (5-12)

$$m_{lj-n} = \left(\frac{1}{2} + \frac{M_n \cos(\omega_0 t - (\ell - 1) \times \frac{2}{3} \pi + \delta_{R-n})}{U_{dc-n}}\right) \cdot U_{dc-n}$$
 (5-13)

where M_n and ω_0 are held constant and $\ell=1,2,3$ corresponding to j=a,b,c, respectively.

Some wind farm owners may want to trade wind power by using pitch control of turbine blades to spill wind power above the contracted level. If P_{ref} control is used with the VSC connected to the wind farm, there will be an unavoidable mismatch. By using infinite AC bus control of (5-12) and (5-13) instead of P_{ref} control, wind farm owners can still fulfill contractual requirements despite pitch controls being used to fulfill the contract.

5.4.3 Circulating Currents Suppression Control

As seen in Fig. 5-2, the current passing through the upper string of capacitors of the phase-a of the n^{th} HVDC station is:

$$i_{ua-n} = \frac{1}{2} i_{a-n} + i_{diffa-n} \tag{5-14}$$

The component $i_{diffa-n}$ consists of the share of DC current from the DC line and the circulating current:

$$i_{diffa-n} = \frac{1}{3} i_{dc-n} + i_{cira-n} \tag{5-15}$$

where i_{dc-n} is the DC current measured at the DC bus and i_{cira-n} is the circulating current. Therefore

$$i_{ua-n} = \frac{1}{2}i_{a-n} + \frac{1}{3}i_{dc-n} + i_{cira-n}$$
 (5-16)

Using the same arguments, the equivalent of (5-16) for the *b*-phase and the *c*-phase are:

$$i_{ub-n} = \frac{1}{2}i_{b-n} + \frac{1}{3}i_{dc-n} + i_{cirb-n}$$
 (5-17)

$$i_{uc-n} = \frac{1}{2}i_{c-n} + \frac{1}{3}i_{dc-n} + i_{circ-n}$$
 (5-18)

Because of the balanced 3-phase operation:

$$i_{a-n} + i_{b-n} + i_{c-n} = 0$$
 (5-19)

As phase angles of the circulating currents are integral multiples of $(4\pi/3)$

$$i_{cira-n} + i_{cirb-n} + i_{circ-n} = 0 (5-20)$$

From the sum of (5-16), (5-17) and (5-18)

$$i_{ua-n} + i_{ub-n} + i_{uc-n} = i_{dc-n}$$
 (5-21)

Therefore

$$i_{cira-n} = i_{ua-n} - \frac{1}{2}i_{a-n} - \frac{1}{3}i_{dc-n}$$
 (5-22)

For the j^{th} (j=a,b,c) phase

$$i_{cirj-n} = i_{uj-n} - \frac{1}{2}i_{j-n} - \frac{1}{3}i_{dc-n}$$
 (5-23)

In order to suppress the circulating current of the j^{th} phase, the current of (5-23) is compared to zero. The error is passed through P-I blocks (proportional gain K_{P-n} and integral gain K_{I-n}). Upon rewriting (3-57) to (3-59), we have

$$\xi_{j-n}(t) = K_{P-n} i_{cirj-n}(t) + K_{I-n} \int_{-\infty}^{t} i_{cirj-n}(\tau) d\tau$$
 (5-24)

The signal is $\xi_{j-n}(t)$, inserted in the modulating signals of the j^{th} phase of the n^{th} MMC station.

Referring to (3-42) to (3-44) and (5-3), the reference signals for the upper and lower arms of phase-j of the n^{th} MMC station are

$$u_{refuj-n} = M_n \cos(\omega_0 t - (\ell - 1) \times \frac{2}{3} \pi + \delta_{R-n}) - \xi_{j-n}$$
 (5-25)

$$u_{reflj-n} = M_n \cos(\omega_0 t - (\ell - 1) \times \frac{2}{3} \pi + \delta_{R-n}) + \xi_{j-n}$$
 (5-26)

where ℓ =1,2,3 and j=a,b,c . ω_0 is the angular frequency and δ_{R-n} is the voltage control angle for the nth MMC station (n=1, 2, 3, 4).

In substituting (5-25) for (5-1) and (5-26) for (5-2), the modulation signals of the upper and lower arms of the j^{th} phase of the n^{th} MMC station are

$$m_{uj-n}(t) = \left[\frac{1}{2} - \frac{M_n \cos(\omega_0 t - (\ell - 1)2\pi/3 + \delta_{R-n}) - \xi_{j-n}(t)}{U_{dc-n}}\right] \cdot U_{dc-n}$$
 (5-27)

$$m_{lj-n}(t) = \left[\frac{1}{2} - \frac{M_n \cos(\omega_0 t - (\ell - 1)2\pi/3 + \delta_{R-n}) + \xi_{j-n}(t)}{U_{dc-n}}\right] \cdot U_{dc-n}$$
 (5-28)

Revising (5-6) to (5-9), the ODE Model with CCSC is obtained, shown from (5-27) to (5-30)

$$\frac{du_{\sum cuj-n}}{dt} = \frac{1}{C_{arm}} \left(\frac{i_{j-n}}{2} + i_{diffi-n} \right) \left(\frac{1}{2} - \frac{u_{refuj-n}}{U_{dc-n}} \right)$$
 (5-29)

$$\frac{du_{\sum cuj-n}}{dt} = \frac{1}{C_{arm}} \left(-\frac{i_{j-n}}{2} + i_{\frac{diffj-n}{2}} \right) \left(\frac{1}{2} + \frac{u_{reflj-n}}{U_{dc-n}} \right)$$
 (5-30)

$$\frac{di_{j-n}}{dt} = \frac{1}{\left(\frac{1}{2}L_m + L_{ac}\right)} \left[\left(\frac{1}{4} + \frac{u_{reflj-n}}{2U_{dc-n}}\right) u_{\sum clj-n} - \left(\frac{1}{4} - \frac{u_{reflij-n}}{2U_{dc-n}}\right) \cdot u_{\sum cuj-n} - \left(\frac{1}{2}R_m + R_{ac}\right) i_{j-n} - v_{j-n} \right] (5-31)$$

$$\frac{di_{difff-n}}{dt} = \frac{1}{2L_{m}} \left[U_{dc-n} - \left(\frac{1}{2} + \frac{u_{reflj-n}}{U_{dc-n}} \right) u_{\sum clj-n} - \left(\frac{1}{2} - \frac{u_{reflij-n}}{U_{dc-n}} \right) \cdot u_{\sum cuj-n} - 2R_{m} i_{diffj-n} \right]$$
(5-32)

5.5 Simulation Results

The tests are organized primarily to test the accuracy of ODE against DEM used as a benchmark. The simulation results in Fig. 5-4 to Fig. 5-7 (ODE Model—blue, DEM--red), and it shows that the blue and red lines overlap, demonstrating the very high accuracy of the ODE model.

Both ODE and DEM have feedback suppression of circulating current implemented. The capability of the ODE to implement the suppression of the circulating current is very important because the circulating current proliferates even harmonics inside the MMC controller and odd harmonics on the AC side.

The test includes step-reversal of power in the command of a power dispatcher to demonstrate agreement in the transients.

The tests are also organized to validate the controls of: (a) a method to receive Stochastic Power; (b) a regulated power dispatch; (c) a DC voltage regulator to maintain a DC grid balance of power.

The windfarm power in the test is contrived. The magnitude and frequencies have been chosen so that power from MMC3 does not interfere visually in reading the curves of MMC1, MMC2 and MMC4. Waveforms from wind farms in service are very different from the contrived waveform used in the test. Fig. 5-4 to Fig. 5-7 together shows the interaction of power dispatchers, DC voltage regulators and stochastic power station of Fig. 5-1 along the same time axes. Parameters used in the test of MTDC-MMC-HVDC are shown in Table 5-I.

5.5.1 Test Scenario

Fig. 5-4 shows the output active power of the MMC1 to the MMC 4. Stochastic power is shown in Fig. 5-4 (c). The stochastic power of Fig. 5-4 (c) is passed to the DC-side of Fig. 5-1, and it is noticeable in the waveforms of Fig. 5-4 (a), (b) and (d). At t=6s, P_{ref-1} of the MMC1 is given a step change to reverse the inverter operation to a rectifier operation. In Fig. 5-4(a), after the transient has subsided, it continues to maintain the power regulation at the new P_{ref-1} as shown in Fig. 5-4 (a). The transient affects the other stations. P_{ref-4} is not changed, and, therefore, Fig. 5-4(d) continues to rectify its assignment. The average level of the power of Fig. 5-4(c) does not change either. The MMC1 is accommodated by the MMC2, the DC voltage regulator, which operates as a power slack to maintain the power balance of the DC grid. Fig. 5-4 (a) and Fig. 5-4 (b) show that power balance is maintained.

Fig. 5-5 shows the DC currents from the 4 MMC stations to the DC grid. Fig. 5-6 shows the DC line currents between the MMC stations.

Fig. 5-7 shows the DC voltage of the MMC1, MMC2, MMC3, and the MMC4. The DC voltages along the DC grid are maintained by the MMC2, the DC voltage regulator. Because the y-axis scale of the graphs in Fig. 5-7 ranges from 50 kV to 70 kV, the DC voltages are overshadowed by high-frequency noise, which arises from the stochastic wind power of the MMC3 through using the y-axis scale from 58 kV to 62 kV.

Fig. 5-8 is an enlargement of Fig. 5-7. The simulation results of the ODE and the DEM do not lie on top of each other. The voltage differences in Fig. 5-8 are due to voltage drops in the current of the stochastic power of the MMC3 across the impedances of DC-line 1, DC-line 2 and DC-line-3 in Fig. 5-3. The disagreement is outside the ODE model and the DEM.

The graphs of the DEM model overlap with those of the ODE model in Fig. 5-4 to Fig. 5-8 showing the accuracy of both methods. The accuracy of the ODE model is validated.

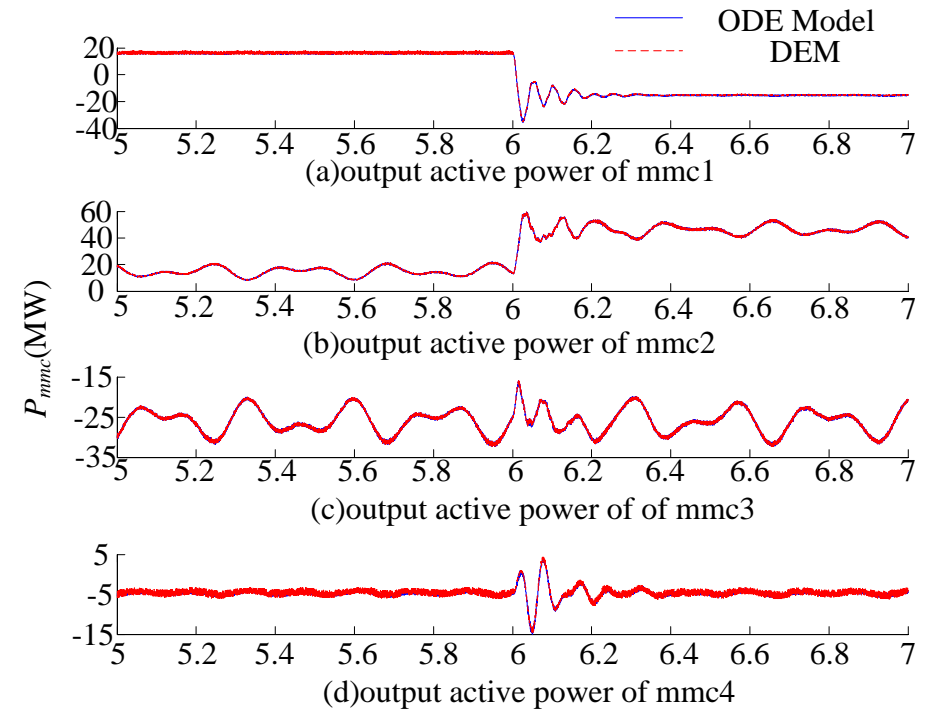


Fig. 5-4 Output active power of the MMC1 to the MMC 4.

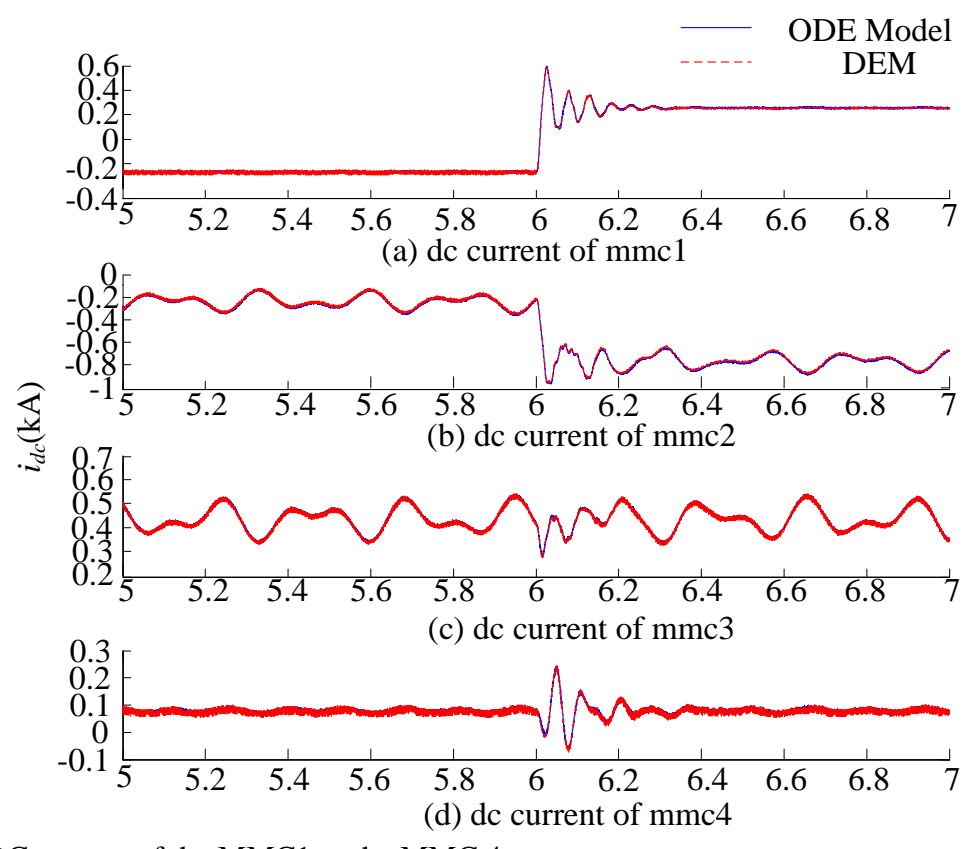


Fig. 5-5 DC current of the MMC1 to the MMC 4

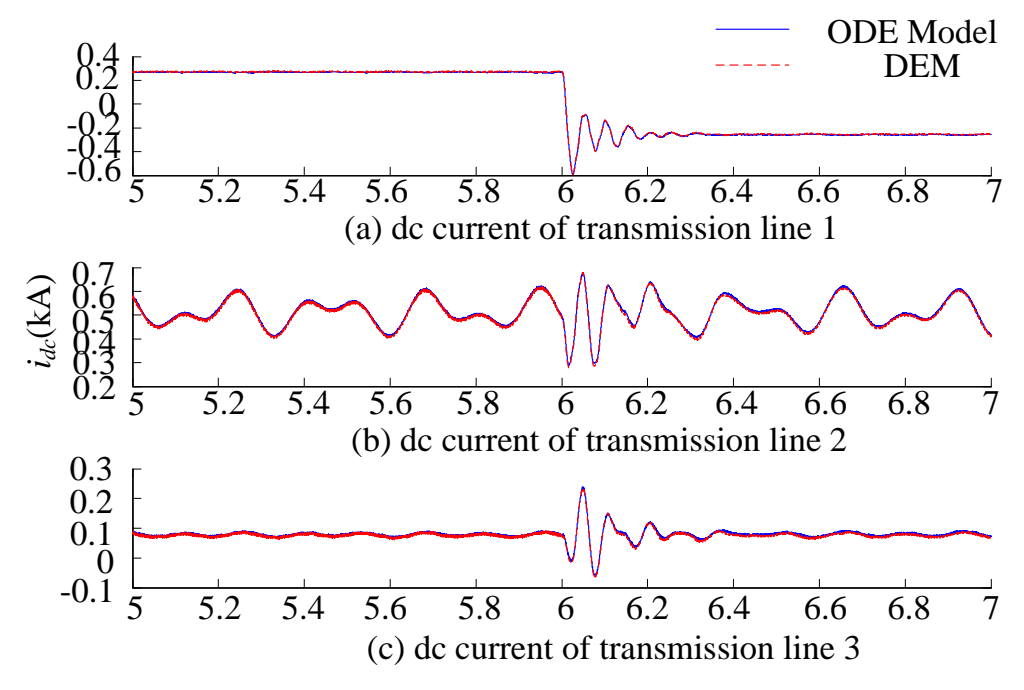


Fig. 5-6 DC line currents: (a) between the MMC 1 and the MMC 2, (b) between the MMC 2 and the MMC 3 and (c) between the MMC 3 and the MMC 4.

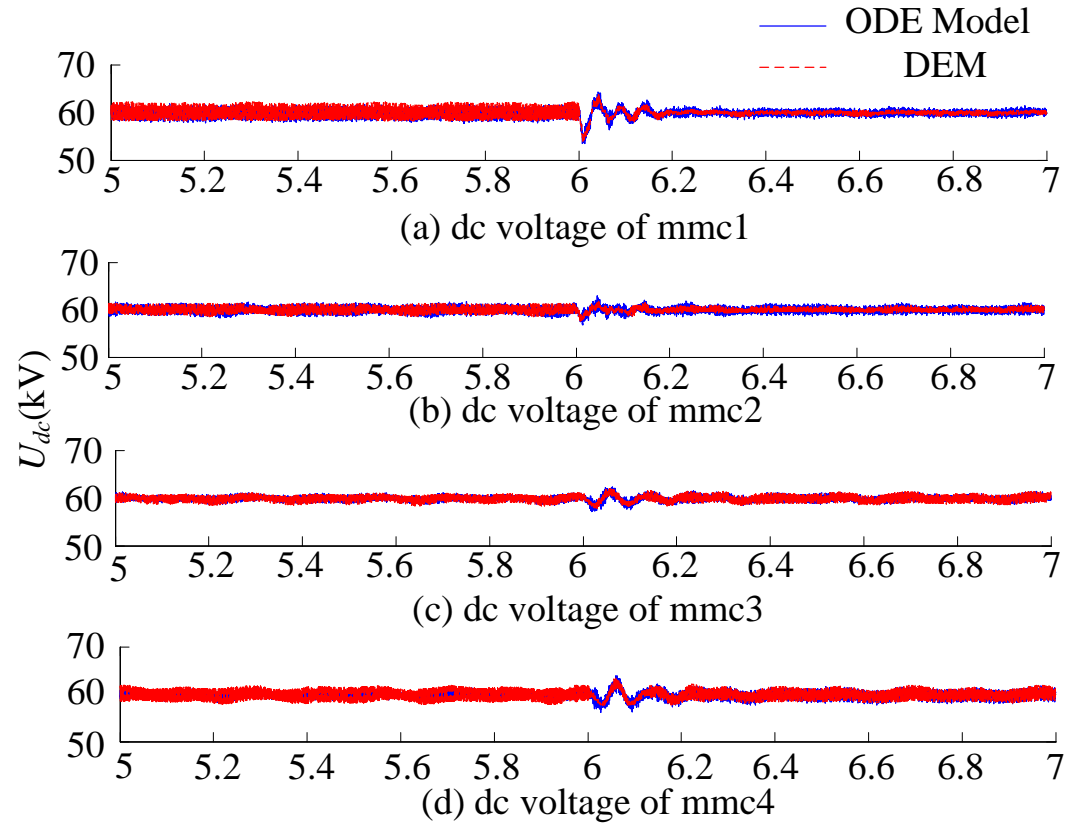


Fig. 5-7 DC voltage of the MMC1 to the MMC4

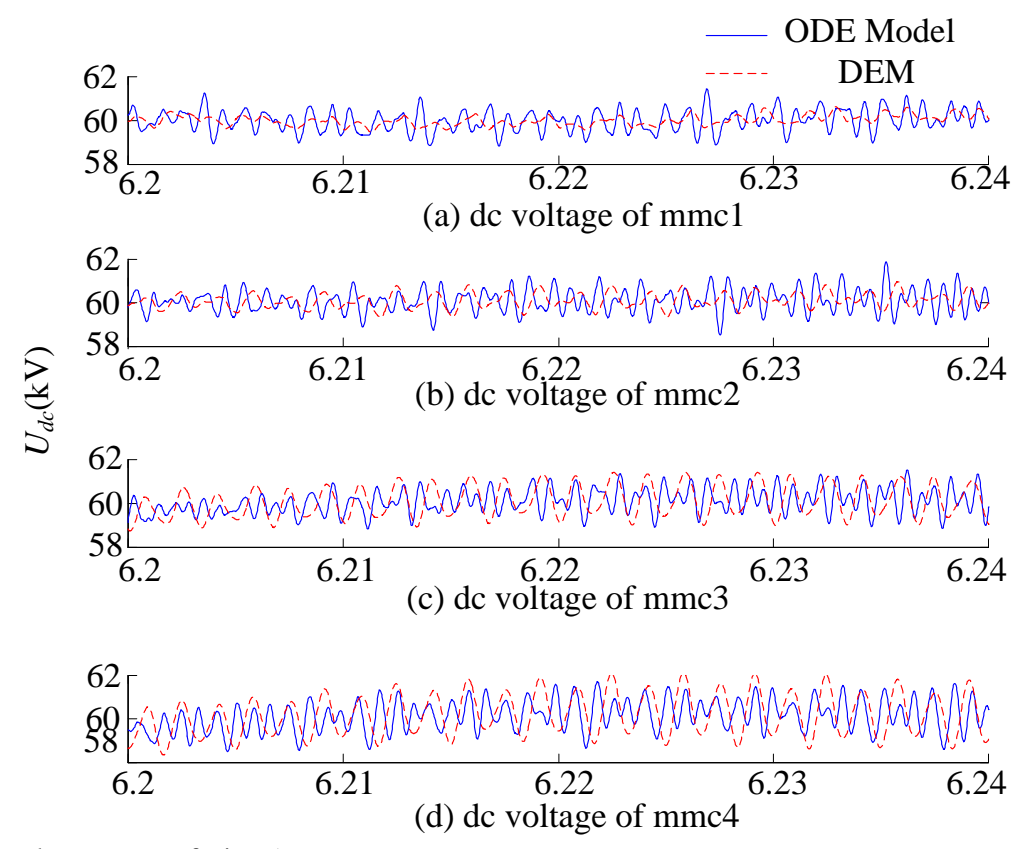


Fig. 5-8 Enlargement of Fig. 5-7

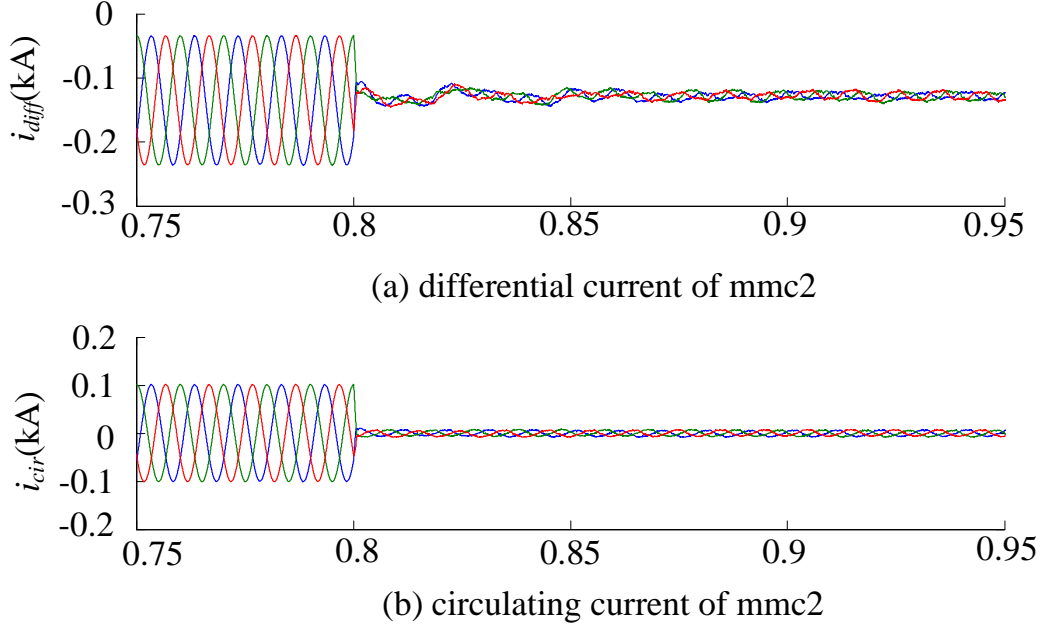


Fig. 5-9 Simulation by the ODE (a) i_{diff} , differential current of a, b and c phase of the MMC2 (b) i_{cir} , circulating current of the a, b and c phases of the MMC2. No suppression t < 0.8s. Suppression enabled: t > 0.8s

Table 5-I Parameters used in MTDC-MMC-HVDC Test

Quantity	Value
DC Grid Voltage U_{dc}	60 kV
AC System nominal voltage	46 kV
Number of Sub-modules per Arm, N	30
Sub-module capacitor voltage	2kV
Arm Inductance L_m	30mH
SM Capacitance C	3 mF
AC Equivalent Inductance L_{ac}	20mH
AC Equivalent Resistance R_{ac}	0.1 Ω
Arm Equivalent Resistance R_m	$0.3~\Omega$
Transmission Line Resistance $R_{n(n+1)}$	0.1 Ω
Transmission Line Inductance $L_{n(n+1)}$	31.8mH
Stray capacitor technique Capacitance C_{bp}	1μF
Damping resistance R_{bp}	$1 \mathrm{M}\Omega$

Table 5-II Comparisons of the computing time between the ODE model and the DEM, obtained from MATLAB/ SIMULINK

	Computin	Computing Times (s)		
Number of SMs/arm	DEM	ODE Model	Speed-up Ratio (%)	
10	171	28.38	602.54	
20	235	28.58	822.25	
30	288	28.64	1005.59	
40	331	28.68	1154.11	

5.5.2 Circulating Currents in Validation Test

Fig.5-9 shows the capability of the ODE model: (a) to represent i_{diff} and circulating current i_{cir} for t < 0.8s and (b) to represent feedback suppression for t > 0.8s. The test was performed on the MMC2.

It must be added that the simulation results of Fig. 5-4 to Fig.5-8 have circulating current suppression applied to both the ODE model and the DEM.

5.5.3 Simulation Speed Comparison

The simulation results of Fig. 5-4 to Fig. 5-8 have the circulating current suppression control that is applied to both the ODE and the DEM methods. The simulation time comparing the ODE and DEM models, obtained from MATLAB/ SIMULINK, are shown in Table 5-II. When DEM is simulated using the optimized standard software RT-LAB in MATLAB/SIMULINK, the speedup time gain is 10.

5.6 Chapter Summary

A four-terminal MMC-HVDC system based on the ODE model is developed in this chapter. The stray capacitor method is introduced as a fast and convenient method to integrate the MMC HVDC stations in a DC grid. The circulating current suppression control (CCSC) to eliminate the inherent 2nd order harmonics is embedded in the proposed ODE model, as well as in the DC voltage control strategy. By comparing the simulation results of the ODE model and the Detail Equivalent Model (DEM) in multiple tests on a multi-terminal MMC-HVDC system, which include stochastic power control and the CCSC, the ODE Model is capable of accelerating the simulation speed by a factor of 10 while maintaining high accuracy. The ODE model has the necessary speed and accuracy to form the simulation platforms for planning, operation and protection studies on a hybrid AC-DC power system.

Chapter 6. Damping Capability of MMC-HVDC Based on the ODE Model

6.1 Introduction

The HVDC has passed through several generations of technology: the 1st-generation mercury arc rectifier, the 2nd-generation line-commutated thyristor, the 3rd-generation VSC-IGBT, and the 4th-generation MMC-IGBT. The 3rd and 4th generations are economical at low power ratings so that they can serve renewable energy technologies, especially in off-shore wind farms where DC transmission favours underwater crossing. Since the MMC is the latest invention, it has received intensive research lately.

This chapter shows that the MMC can provide Power Oscillation Damping (POD). The first step consists of applying small-signal analysis to confirm that the requisite power to implement the POD is proportional to the frequency of power oscillation, that is, $d\delta/dt$, where δ is the rotor angle. Time differentiation with respect to time, is from a theoretical viewpoint, not realizable. The numerical derivative introduces noise that requires filtering by means of a low-pass filter. As low pass filtering consists of integration, it nullifies the derivative operator. An innovative passive local control method is proposed based on a three-phase phase-locked loop (PLL), which measures the signal $d\delta/dt$ without differentiation. After successfully showing that the MMC-HVDC can provide Power Oscillation Damping (POD), this chapter proceeds to use the damping to exceed the transient stability limit, thereby increasing active power transmissibility. However, one obstacle in implementing POD lies in line-to-ground faults in the transmission line. As the MMC-HVDC operates as a voltage source, the very low impedance of the AC line-to-ground fault results in destructively large fault currents, which destroy the IGBTs of the HVDC station, thus making the MMC's power oscillation damping useless. Hence, it is necessary to convert the MMC that operates under reference voltage control to reference current control. Under the individual phase deadbeat control[151], which is the name of the reference current control used in this thesis, only the reference controlled current flows although the AC terminal voltage drops during the AC lineground faults. When protected by the reference current control (Deadbeat), the POD capability of the MMC-HVDC station can be applied to exceed the Transient Stability Limit. Simulation results show that, with the proposed control method, an MMC-HVDC station can not only damp power oscillation, but also increase the active power transmissibility of the AC line.

In this chapter, analysis has been conducted first to confirm that the damping power must be proportional to the frequency of the power oscillation. Secondly, a three-phase Phase-Locked Loop (PLL) is applied to obtain the frequency of power oscillation. For readers unfamiliar with the operation of a three-phase Phase-Locked Loop (PLL), this chapter includes a brief revision.

The method incorporating the frequency obtained by the PLL the MMC modulation signals is described.

The simulation test system consists of a radial AC transmission line with a turbine-generator at one end, and an infinite bus at the other end. The MMC-HVDC station is connected in shunt to the AC line. The MMC-HVDC is simulated by the ODE Model in MATLAB SIMULINK. The effect of damping on the transient stability of the test system is evaluated, and the simulation results are presented.

It should be pointed out that the simulation results contain the multi-function control capability embedded in the ODE model. They are:

- (1) The Power Oscillation Damping capability;
- (2) The Circulating Current Suppression Control (CCSC);
- (3) The Deadbeat control (Reference Current Control) of [151] to protect against short circuit faults.

6.2 Property Required for Damping

Literature research shows that existing methods of implementing damping are based on the leadlag transfer function blocks and a washout block of [152]. However, there is no explanation on how and why they are used. This section returns to the first principle to show that the damping power must be proportional to $\varpi = d\Delta \delta/dt$, where ϖ presents the power oscillation frequency, and δ is the voltage angle.

For the turbine torque T_t to drive the moment inertia J against generator counter-torque T_e , the equation according to Newton's Law of Motion is:

$$J\frac{d\omega}{dt} = T_t - T_e \tag{6-1}$$

$$\frac{d\delta}{dt} = \omega \tag{6-2}$$

Substituting the generator counter-torque $T_e = V^2 \sin \delta / X \omega_c$, where X is the equivalent transmission line impedance of the radial transmission line connecting the generator to an infinite AC bus, (6-1) and (6-2) are compacted as:

$$J d^2 \delta / dt = T_t - \frac{V^2 \sin \delta}{X \omega_C}$$
 (6-3)

where ω_c is the line frequency.

6.2.1 Small Signal Linearization

Writing $\delta = \delta_0 + \Delta \delta$, (6-3) becomes

$$J d^{2}(\delta_{0} + \Delta \delta) / dt = T_{t} - \frac{V^{2} \sin(\delta_{0} + \Delta \delta)}{X \omega_{c}}$$

$$(6-4)$$

(6-4) decomposes into two terms by neglecting the 2^{nd} and higher-order terms of $\Delta\delta$.

$$J d^{2}(\delta_{0})/dt = T_{t} - \frac{V^{2} \sin(\delta_{0})}{X \omega}$$

$$\tag{6-5}$$

$$J d^{2}(\Delta \delta)/dt = -\frac{(V^{2} \cos \delta_{0}) \Delta \delta}{X \omega_{c}}$$
(6-6)

From (6-5), steady-state operation is when

$$T_t = \frac{V^2 \sin(\delta_0)}{X \omega_c} \tag{6-7}$$

Taking the Laplace Transform of (6-6)

$$s^{2} \Delta \delta(s) = -\frac{(V^{2} \cos \delta_{0}) \Delta \delta(s)}{JX \omega_{c}}$$
(6-8)

The solution requires finding the roots of

$$s^2 = -\frac{(V^2 \cos \delta_0)}{JX \omega_0} \tag{6-9}$$

The time-domain solution is:

$$\Delta \delta(t) = A\cos(\omega_{\text{osc}}t) + B\sin(\omega_{\text{osc}}t)$$
 (6-10)

where $\omega_{osc} = \sqrt{(V^2 \cos \delta_0)/JX\omega_c}$. In this case, no damping has been applied.

6.2.2 Dynamics Small Signal Linearization with Damping

In order to damp the oscillation, a $d\delta/dt$ term is added to (6-3) so the new equation is

$$J d^{2} \delta / dt = T_{t} - \frac{V^{2} \sin \delta}{X \omega_{t}} - C \frac{d \delta}{dt}$$
(6-11)

where *C* is the damping coefficient.

Following the same small signal linearization, (6-6) becomes

$$J d^{2}(\Delta \delta)/dt = -\frac{(V^{2} \cos \delta_{0})\Delta \delta}{X \omega} - \frac{C d \Delta \delta}{dt}$$
(6-12)

Taking the Laplace Transform of (6-12), one has

$$s^{2}\Delta\delta(s) = -\frac{(V^{2}\cos\delta_{0})\Delta\delta(s)}{JX\omega_{c}} - \frac{C}{J}\Delta\delta(s)$$
 (6-13)

The characteristic roots are solved from

$$s^{2} + \frac{C}{I}s + \frac{(V^{2}\cos\delta_{0})}{IX\omega} = 0$$
(6-14)

The roots of the quadratic equation are:

$$s = -\frac{C}{2J} \pm j \sqrt{\frac{(V^2 \cos \delta_0)}{JX \omega_c} - (\frac{C}{J})^2}$$
 (6-15)

The time-domain solution is

$$\Delta \delta(t) = [A\cos\omega_{osc-d}(t) + B\sin\omega_{osc-d}(t)]e^{-\sigma t}$$
 (6-16)

where A and B are constants of integration and the damping factor is $\sigma = C/2J$ and $\omega_{osc} = \sqrt{(V^2 \cos \delta_0)/JX\omega_C - (C/J)^2}$.

Damping comes from the exponentially time-decaying term $e^{-(0.5C/J)t}$ in (6-16) which originates from $(-Cd\delta/dt)$ added to (6-3). The conclusion is that damping requires the injection of active power proportional to $d\Delta\delta/dt$ term.

6.3 Damping Power Implementation

For MMC-HVDC, $d\Delta\delta/dt$ has to be obtained from the terminal voltages $v_a(t), v_b(t), v_c(t)$ at the point-of-common-coupling (PCC) with the AC grid. A phase-locked loop (PLL), as illustrated in Fig.6-1, extracts this information without differentiation.

6.3.1 Principle of PLL Operation

The PLL tracks the voltage angle θ_0 of the grid voltages $v_a(t)$, $v_b(t)$, $v_c(t)$ by negative feedback. Negative feedback requires having an error ε (shown in Fig. 6-1) which is obtained by the Detector. The error ε activates a Voltage Controlled Oscillator (VCO) to increase the output angle θ_v until the error is zero, whereupon $\theta_v = \theta_0$ so that the angle of $v_a(t)$, $v_b(t)$, $v_c(t)$ is tracked. This requires that, in Fig. 6-1, θ_v increases monotonically with non-zero error ε .

6.3.1.1 Detector

At the point-of-common-coupling (PCC), $v_a(t)$, $v_b(t)$, $v_c(t)$ are measured and transformed into 2-phase $v_\alpha(t)$, $v_\beta(t)$, which are the inputs of Fig. 6-1. The details of the transformation between the a-b-c frame to an α - β frame is presented in Appendix A.

The detector obtains the error ε with the help of functions $sin\theta_v$ and $cos\theta_v$ formed from the output angle θ_v in Fig. 6-1. The signal $sin\theta_v$ is multiplied by $v_{\alpha}(t)$. Likewise, $cos\theta_v$ is multiplied by $v_{\beta}(t)$. Their products are subtracted to form the error ε .

The feedback error is based on the trigonometric identity $\sin(A-B) \equiv \sin A \cos B - \cos A \sin B$.

$$\varepsilon = v_{\beta} \cos \theta_{\nu} - v_{\alpha} \sin \theta_{\nu} = V \sin \theta_{0} \cos \theta_{\nu} - V \cos \theta_{0} \sin \theta_{\nu} = V \sin(\theta_{0} - \theta_{\nu}) \quad (6-17)$$

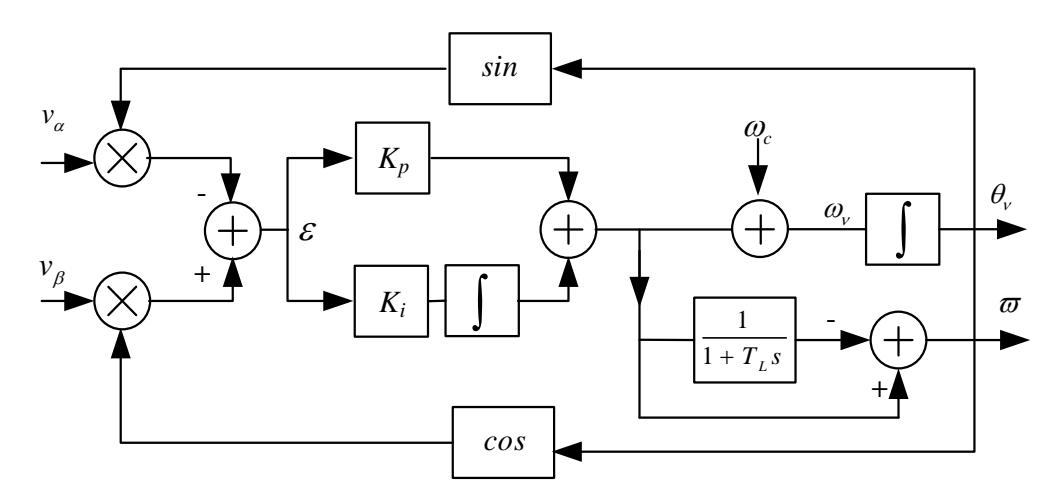


Fig. 6-1 Three-phase Phase-Locked Loop (PLL)

In (6-17), $\sin(\theta_0 - \theta_v)$ is a monotonically increasing function of $(\theta_0 - \theta_v)$ within the region $-90^{\circ} < (\theta_0 - \theta_v) < 90^{\circ}$.

6.3.1.2 Voltage Controlled Oscillator (VCO)

The *P-I* block (proportional gain K_p and integral gain K_i) serves the same function as the traditional Voltage Controlled Oscillator (VCO). This is because a positive error ε causes the frequency ω_{ν} to increase so that one has effectively a VCO.

The constant frequency $\omega_c = 2\pi f_0$ ($f_0 = 50$ Hz, 60Hz) is added by PLL designers to increase the range of frequency acquisition, and to improve the transient response.

Their sum ω_{ν} is the input of an integrator block whose output is θ_{ν} . The trigonometric functions $\cos \theta_{\nu}$ and $\sin \theta_{\nu}$ are formed and multiplied to $v_{\alpha}(t)$ and $v_{\beta}(t)$ to produce the error in (6-17).

As $\sin(\theta_0 - \theta_v)$ in (6-17) is a monotonically increasing function within the region -90°<(θ_0 - θ_v)<90°, the output increases until the error ε =0 is reached when θ_0 - θ_v =0. The PLL has then tracked the input phase angle θ_0 .

6.3.2 Frequency of Power Oscillation

The angle θ_v is the output of the integration block in Fig. 6-1, whose input is frequency ω_v . In the presence of a power oscillation, the sought-after signal $\varpi = d\delta/dt$ is contained in ω_v . When there is no power oscillation, the sought-after signal $\varpi = d\delta/dt = 0$ is also contained in ω_v . It is necessary to distinguish $\varpi = d\delta/dt$, (which arises because of a fault), from the grid frequency ω_{grid} (which has a low frequency close to 50 Hz). When there is no power oscillation, $\omega_v = \omega_{grid}$.

To extract ω_{grid} , ω_v is passed through a low pass filter so that $\omega_{grid} = [1/(1+T_L s)]\omega_v$. The signal to implement damping is obtained from the difference, $\varpi = \omega_v - \omega_{grid}$, which is shown as output in Fig.6-1.

6.4 Damping by Modular Multilevel Converter (MMC)

6.4.1 MMC-HVDC and Modulating Signals

Fig. 6-2 illustrates the three phases of the MMC-HVDC connected to the DC voltage U_{dc} . The control for the MMC is based on modulating signals of the upper and lower arms. For phase-a, they are:

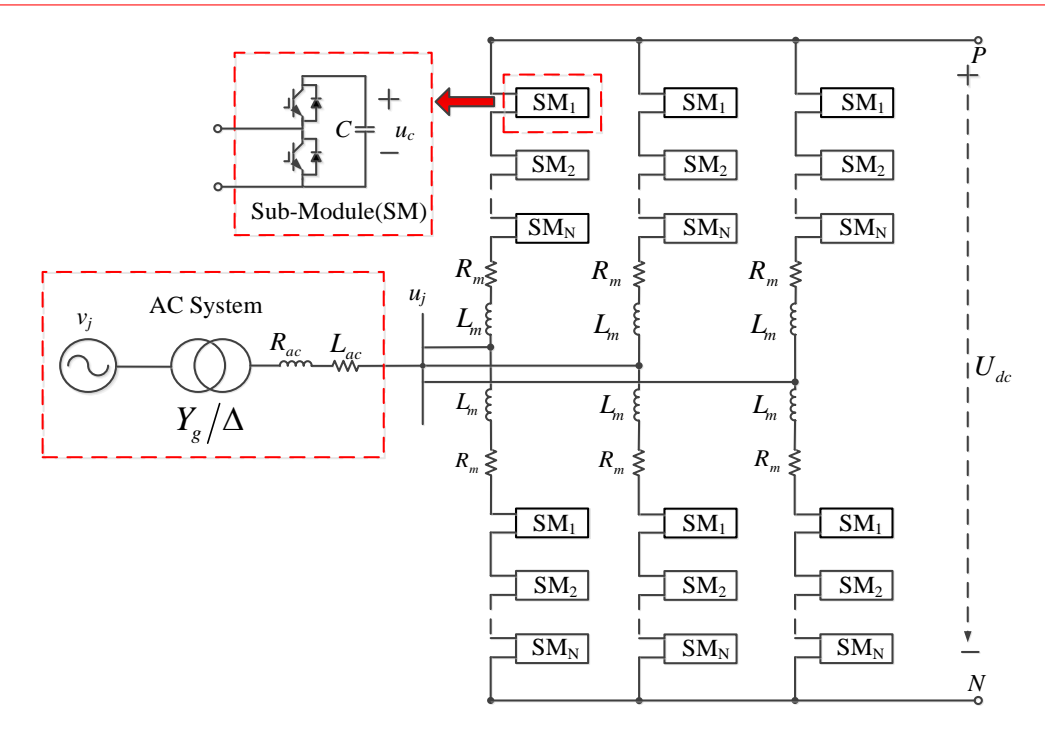


Fig. 6-2 Schematic of three phases of the MMC-HVDC

$$m_{ua}(t) = \left(\frac{1}{2} - \frac{M}{U_{dc}}\cos(\omega_0 t + \delta_{ref})\right) \cdot U_{dc}$$
 (6-18)

$$m_{la}(t) = \left(\frac{1}{2} + \frac{M}{U_{dc}}\cos(\omega_0 t + \delta_{ref})\right) \cdot U_{dc}$$
 (6-19)

where M and δ_{ref} control the voltage magnitude and the voltage angle of the AC voltage output of the phase-a, respectively. The phase-b and phase-c have the same modulating signals as (6-18) and (6-19) except for phase shifts of -120 and -240 degrees.

From power system engineering practice [153], δ and M in (6-18) (6-19) are used to control the active power and the voltage magnitude, respectively.

6.4.2 Incorporating Signal for Power Oscillation Damping

In order to incorporate active damping power, the modulating signals of (6-18) and (6-19) are modified to:

$$m_{ua}(t) = \left(\frac{1}{2} - \frac{M}{U_{dc}}\cos(\omega_0 t + \delta_{ref} + k_\theta \varpi)\right) \cdot U_{dc}$$
 (6-20)

$$m_{la}(t) = \left(\frac{1}{2} + \frac{M}{U_{dc}}\cos(\omega_0 t + \delta_{ref} + k_\theta \varpi)\right) \cdot U_{dc}$$
 (6-21)

where k_{θ} represents the damping control gain.

In (6-20) and (6-21), $k_{\theta}\overline{\omega}$ is added to δ_{ref} to output the active power for damping.

In the control based on the Decoupled P-Q control, $k_{\theta}\varpi$ is added to P_{ref} .

6.5 Multiple Control Capability in MMC-HVDC

In order to operate in the power system, the MMC-HVDC must have multiple control capability. The MMC-HVDC naturally operates under voltage control. One desirable controllability consists of changing the control of the MMC-HVDC station from the voltage control to regulated current control so that the IGBTs are not destroyed by detrimental large fault currents. Fig. 6-3 shows all the multi-function control of the MMC HVDC station in this chapter. The multi-function control implements (*i*) damping, (ii) individual phase deadbeat for protection and (iii) decoupled P-Q control. The AC lines of the MMC station, in Fig. 6-3, are connected in shunt to the AC grid.

6.5.1 Damping control

The voltages v_{PCC} , after transformation to the α - β frame are fed to the PLL in Fig.6-1, which has 2 outputs ϖ and θ_v . The signal ϖ is passed through the gain block k_θ . The signal $k_\theta \varpi$ to produce damping power is added to i_{dref} , the output of the decoupled P-Q control block.

6.5.2 Decoupled P-Q Control

Decoupled P-Q control is implemented in the d-q frame. The output θ_v from the Phase Locked Loop (PLL) of Fig.6-1 is applied to form $\cos \theta_v$ and $\sin \theta_v$, which are used in the α - β to d-q transformation, and inversely from d-q back to α - β . Complex power references are P_{ref} , Q_{ref} , incorporating the feedback measurements P_s , Q_s . From the PLL, phase-a equates phase-d. Transformation yields the voltage v_d and v_q =0. In Decoupled P-Q Control as v_q =0, i_{dref} = P/v_d and i_{qref} = Q/v_d .

6.5.3 Regulated Current Control

The MMC is naturally a voltage reference controller. The AC voltages are commanded by u_{ref} in the modulating signal (3-10) and (3-11). The first step in regulated current control consists of measuring the voltages v_{PCC} at the point-of-common-coupling (PCC) in Fig. 6-3. The voltages v_{PCC} vary as the grid voltage. During short circuit faults, the v_{PCC} drops to very low voltages, close to ground potential. The voltages v_{PCC} at the PCC differ from the voltages outputted by the

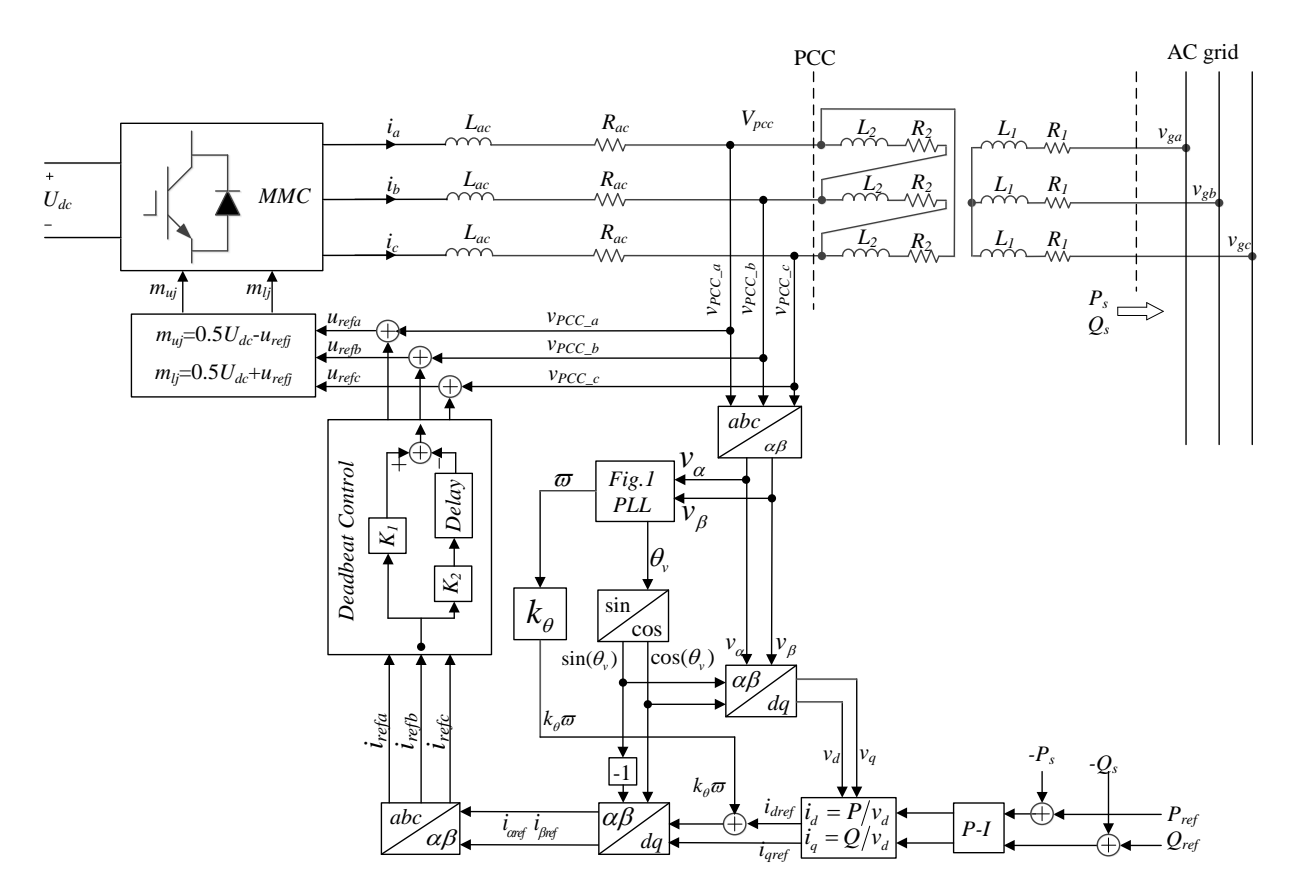


Fig. 6-3 Multi-Function Control Diagram of the MMC

modulating signals (3-10) and (3-11), and by the voltage drops of the injected currents i_a , i_b and i_c across L_{ac} and R_{ac} . Thus, if i_{ref} is to be the regulated current, it is a matter of using u_{ref} in the modulating signal (3-10) and (3-11) to produce the sum of v_{PCC} , and the voltage drops of the injected currents i_{ref} of the a-, b- and c-phase across L_{ac} and R_{ac} . As the feed-forward voltage from the PCC is $v_a = v_{PCC_a}$, the resultant voltage u_{ref} is $v_a + L_{ac} di_{refa} / dt + R_{ac} i_{refa}$.

As the d/dt operation is inherently noisy and therefore inaccurate, the current i_{refa} is passed through the deadbeat block, which is simple to implement because it contains a gain K_1 in parallel to another gain K_2 with a time delay block. The digital closed-loop deadbeat controller is briefly introduced in Appendix B.

In Fig. 6-3, u_{ref} for the 3-phases are u_{refa} , u_{refb} , u_{refc} . The measured PCC voltages are feed-forwarded as v_{PCC_a} , v_{PCC_c} , v_{PCC_c} . The voltage drops across internal resistance R_{ac} and inductor L_{ac} are added from the Deadbeat control block. In the deadbeat control, each reference current i_{refa} , i_{refb} , i_{refc} has 2 branches. The references are multiplied by gain constants K_1 and K_2 . The branch of

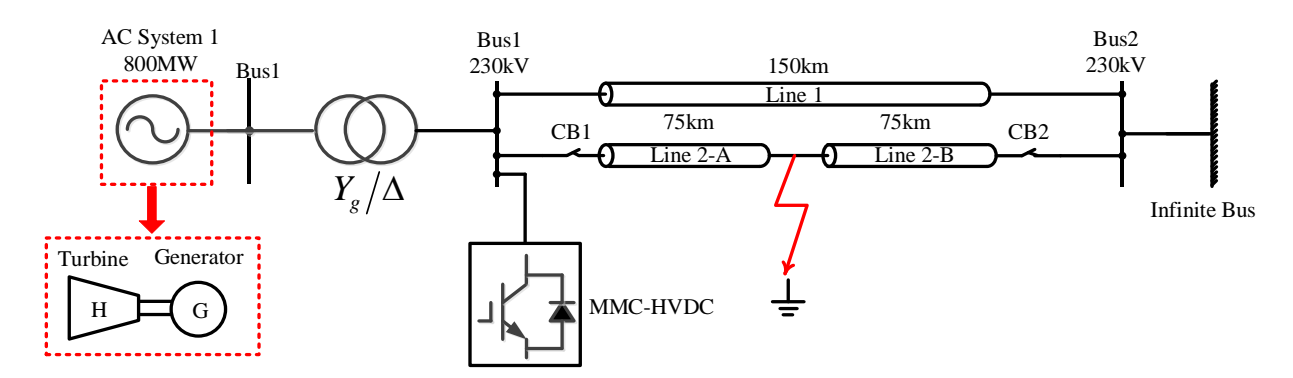


Fig. 6-4 Test system of a radial transmission line with the MMC-HVDC station connected in a shunt.

 K_2 has a time delay. The combinations of the two branches are added to the feedforward voltages v_{PCC_a} , v_{PCC_b} , v_{PCC_c} to form the MMC voltage references u_{refa} , u_{refb} , u_{refc} . Individual Phase Deadbeat ensures that asymmetrical faults can be dealt with.

Deadbeat is applied because the method bypasses the need to differentiate in the term $L_{\rm ac}di_{\rm ref}/dt$. In addition, there is no time delay associated with the time constant $L_{\rm ac}/R_{\rm ac}$.

The AC output voltages of the MMC-HVDC consist of the voltage drops of R_{ac} and L_{ac} by the regulated current and the feed-forward PCC voltages. The MMC-HVDC outputs the regulated current irrespective of the voltages of the PCC. When there is a 3-phase short-circuit-to-ground fault, the voltages of the PCC are at ground potential, but the MMC-HVDC continues to output regulated current.

6.6 Simulation Results

6.6.1 Simulation Test Platform

Fig. 6-4 shows the single-line diagram of a radial power system planned for transient stability tests. The test line transmits power from a turbine-generator to the infinite bus. In the transients, the rotor angle δ of the turbine-generator "swings" against the infinite bus. MATLAB SIMULINK is used as simulation software.

Appendix C lists the detail parameters of the generator (GENROU). The models, taken from IEEE, are: turbine-governor system (1981 IEEE type 2), field excitation system (IEEE type 1), and transformers. Transmission Lines 1 and 2, are both of a length of 150 km. They are modeled by

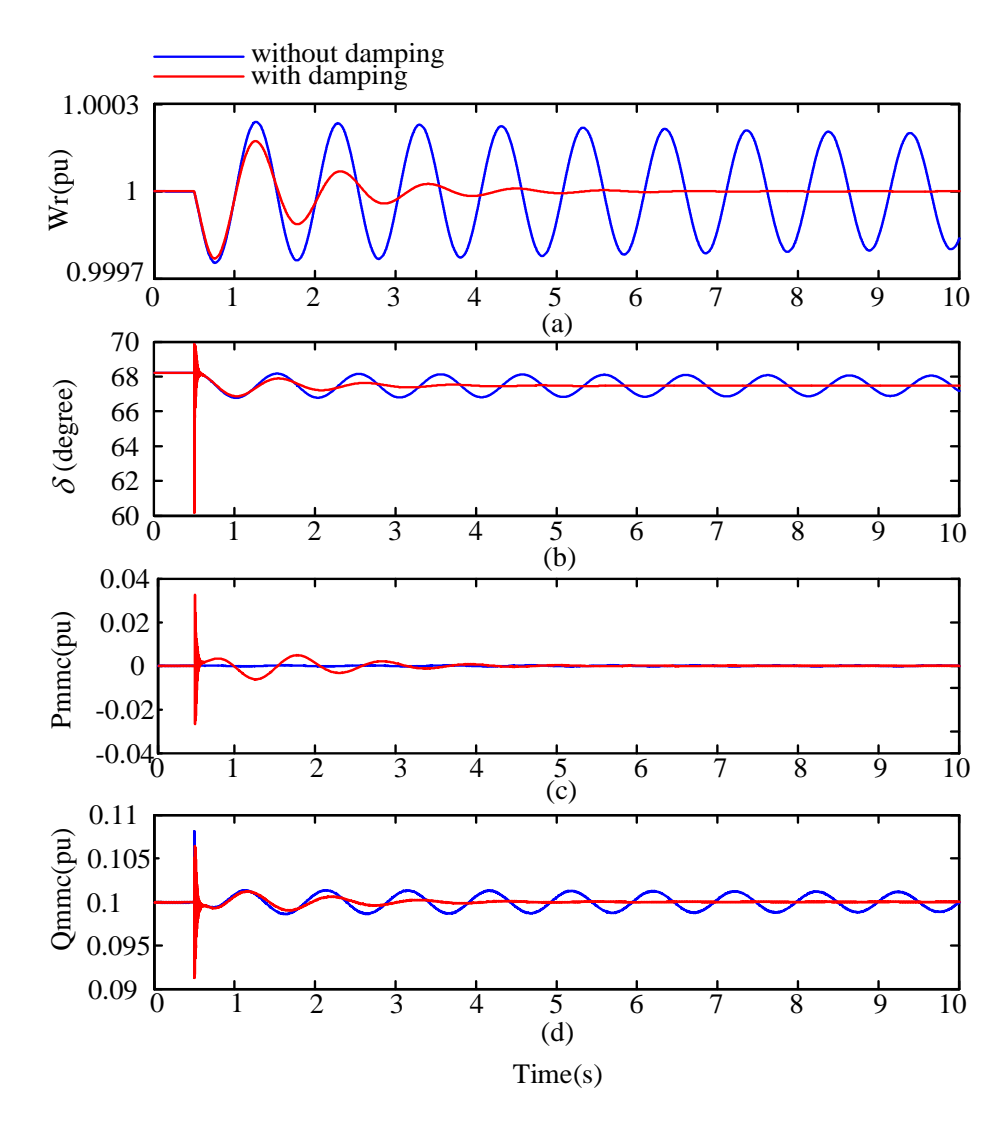


Fig.6-5 Response to load increase (12.5%) at t=0.5s. (a) rotor speed pu (ac grid frequency); (b) voltage angle δ ;(c) MMC active power output (pu); (d) MMC reactive power output (pu).

distributed pi-sections, with each pi-section representing a length of 150 km. The generator is driven by a speed-regulated DC motor (for the turbine).

The MMC-HVDC is connected in shunt to the AC transmission line. The HVDC station belongs to a point-to-point HVDC system. Each phase of the MMC-HVDC station is modeled with 200 sub-modules per arm.

6.6.2 Damping Capability Tests

After the steady-state has been reached, a step increment of a load of 12.5% at t=0.5s is given to excite power oscillation. In Fig. 6-5, the blue and red lines of the simulation results are with and

without damping by the MMC-HVDC, respectively. The red line shows that the power oscillations are damped by the MMC-HVDC. Fig. 6-5 (a) displays the rotor speed which is proportional to the power oscillation frequency. The constant rotor speed of 1.0 pu corresponds to the grid frequency ω_{grid} . Fig. 6-5 (b) shows the generator voltage angle δ with respect to the infinite bus. Fig. 6-5 (c) and (d) show the active and reactive power outputted by the MMC-HVDC station. The reference of the active power of the MMC-HVDC is set to zero in all tests. This enables the active power required to implement damping to be studied in isolation.

The parameter settings of the generator, the turbine-governor system, and the field excitation system are listed in Appendix C.

6.6.3 Transient Stability Test Conditions and Results

This section investigates if damping can increase the transient stability limit, thereby allowing for more power to be transmitted.

In the transient stability limit test, a 3-phase line-to-ground fault is simulated in the mid-point of Line 2 of Fig. 6-4 at t=0.5s. The voltages at the fault location collapse to ground potential. Between the incidence of the fault and the opening of circuit breakers, there is a delay of 5 AC cycles. It is critical that the IGBTs of the MMC-HVDC station are not destroyed by the fault current. The MMC-HVDC station must have the deadbeat protection [151] in addition to the damping capability.

After 5 cycles (100ms), the circuit breakers of Line 2 (CB1 and CB2) open. The transmission line voltages recover. Power is transmitted through transmission Line 1.

Damping control is determined by k_{θ} , the damping control gain of (6-20) and (6-21). Results, in which there is no MMC-HVDC damping, are identified by k_{θ} =0. Negative k_{θ} indicates that the MMC-HVDC station removes the power oscillations from the AC-side by rectifying it to DC.

Table 6-I summarizes the test conditions of Fig. 6-6 and Fig. 6-7. As the results on transient stability tests are new, they are presented to familiarize readers with: (i) the waveforms of δ and transmitted active power P_e ; (ii) the roles played by k_{θ} and P_e in determining stable operation. It should be noted that P_e is the active power through the transmission line because the active power of the MMC-HVDC is set to zero.

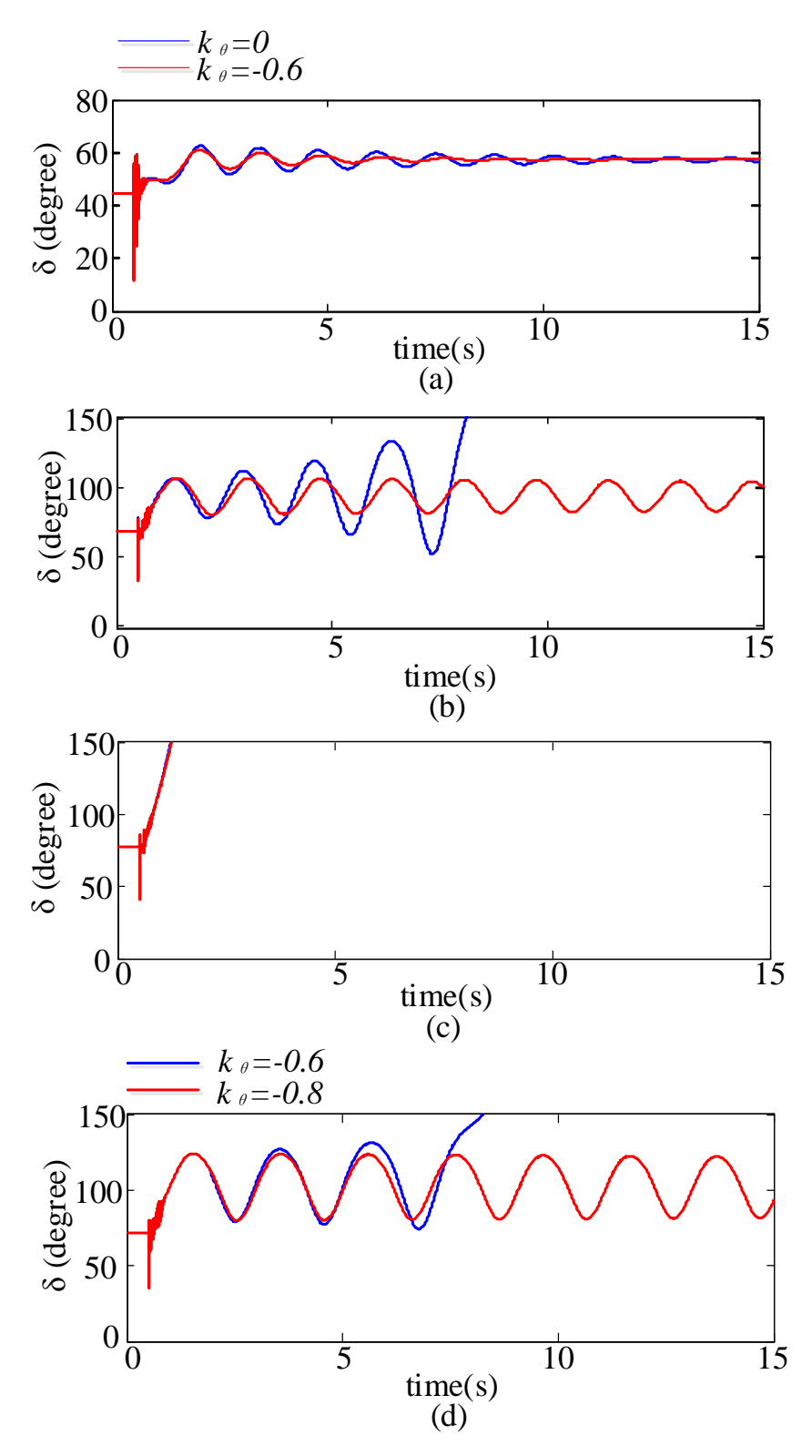


Fig. 6-6 Power angle during transient stability test (a) P_e =0.4pu, k_θ =0 stable, k_θ =-0.6 stable. (b) P_e =0.7pu, k_θ =0 unstable, k_θ =-0.6 stable. (c) P_e =0.85pu, k_θ =0 unstable, k_θ =-0.6 unstable. (d) P_e =0.75pu, k_θ =-0.6 unstable, k_θ =-0.8 stable.

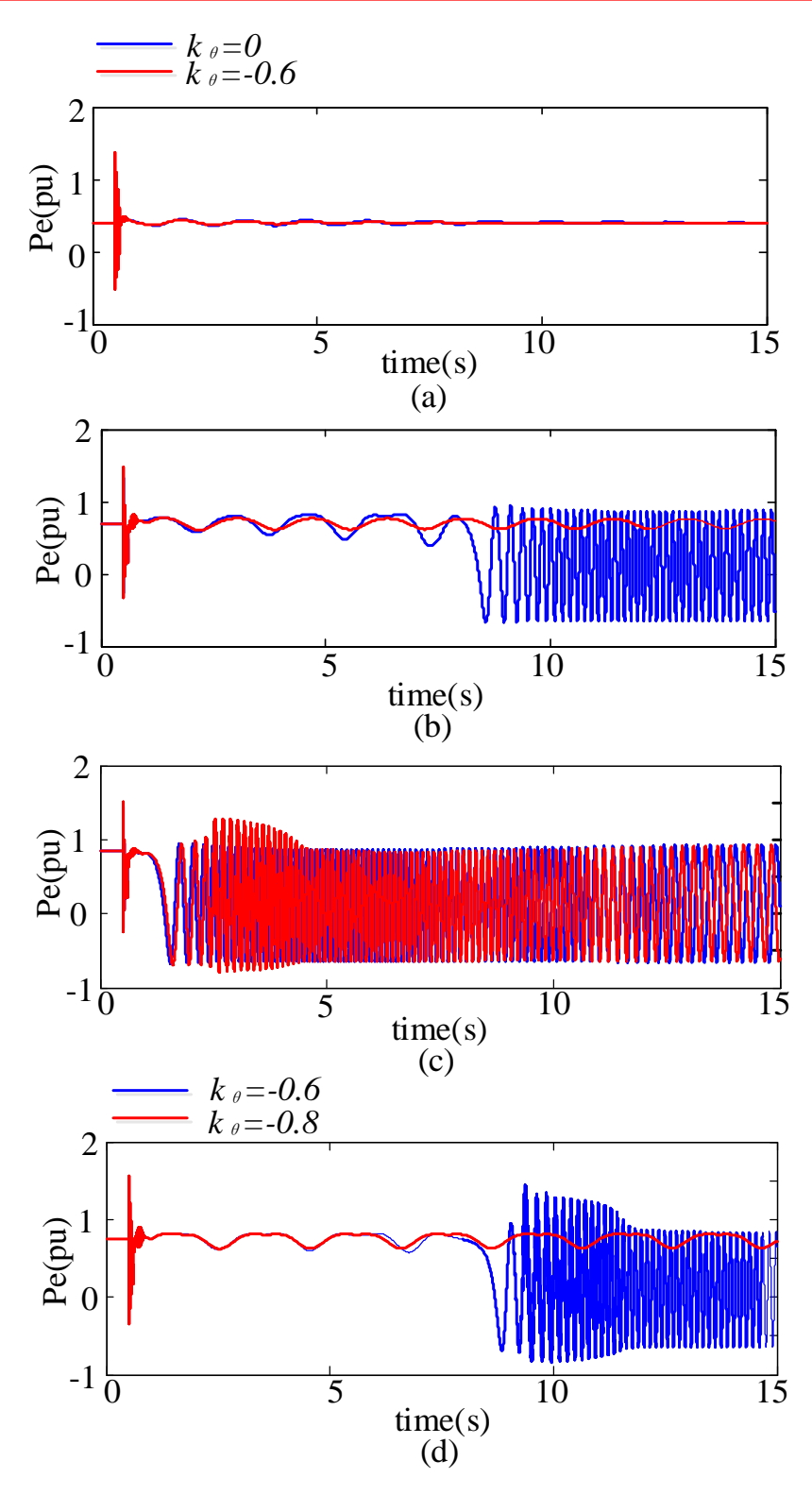


Fig. 6-7 Active power in transmission line in transient stability test. (a) P_e =0.4pu, k_θ =0 stable, k_θ =-0.6 stable. (b) P_e =0.7pu, k_θ =0 unstable, k_θ =-0.6 stable. (c) P_e =0.85pu, k_θ =0 unstable, k_θ =-0.6 unstable. (d) P_e =0.75pu, k_θ =-0.6 unstable, k_θ =-0.8 stable.

Table 6-I Transient Stability Test

	P_e	k_{θ} (blue)	No damping	k_{θ} (red)	with damping
Fig. 5(a) and Fig. 6(a)	0.4	0	Stable	-0.6	Stable
Fig. 5(b) and Fig. 6(b)	0.7	0	Unstable	-0.6	Stable
Fig. 5(c) and Fig. 6(c)	0.85	0	Unstable	-0.6	Unstable
Fig. 5(d) and Fig. 6(d)	0.75	-0.6	Unstable (with damping)	-0.8	Stable

Table 6-II Power Transmissibility Gain from Damping

Damping	Transient Stability Limit	Power Angle	Power Transmissibility Gain	
Constant	Transmitted Power (pu)	(/acma)	Per Unit Gain	
$(k_{ heta})$	P_{base} =800MW	δ (degree)	Base Power: 0.53×800MW	
0	0.53	72.85	1.00	
-0.1	0.56	76.55	1.06	
-0.2	0.59	80.04	1.17	
-0.3	0.62	83.54	1.30	
-0.4	0.65	87.14	1.23	
-0.5	0.68	90.82	1.28	
-0.6	0.71	94.83	1.34	
-0.7	0.73	97.48	1.42	
-0.8	0.75	100.45	1.42	
-0.9	0.75	100.45	1.42	

Fig. 6-6(a) and Fig. 6-7(a) show for P_e =0.4pu, the system is stable. Fig. 6-6(b) and Fig. 6-7(b) show that, in raising the active power to P_e =0.7 pu, the system becomes unstable when there is no MMC damping. However, it is stabilized by the damping of the MMC-HVDC. Fig. 6-6(c) and Fig. 6-7(c) show that, when P_e is raised above 0.85pu, MMC-HVDC damping fails to stabilize the system. Fig. 6-6 (d) and Fig. 6-7 (d) show that, for P_e =0.75pu, the system is unstable when the

MMC damping k_{θ} =-0.6. But, by changing k_{θ} to -0.8, the system is stabilized. The maximum transmitted power obtained when k_{θ} =-0.8.

From Fig. 6-6(b), Fig. 6-6(c) and Fig. 6-6(d), instability is characterized by a steep ascending ramp in δ . From Fig. 6-7 (b), Fig. 6-7(c) and Fig. 6-7(d), instability is characterized by $P_e(t)$ having a high-frequency oscillation. Fig. 17.16 (a) and (b) provide validation on page 1143 in [152], respectively, because the waveforms of voltage angle δ and P_e in Fig. 6-7, are similar in terms of stable and unstable operation.

6.6.4 Increasing Power Transmissibility by MMC-HVDC Damping

As the simulations of Fig. 6-6 (b) to Fig. 6-6 (d) and of Fig. 6-7(b) to Fig.6-7(d) show that the transient stability limit can be increased by MMC-HVDC damping, a systematic study has been pursued to evaluate the increase of power transmissibility by increasing the magnitude of the damping constant k_{θ} . Table 6-II summarizes the results. Table 6-II keeps a record of the power angle for future research on nonlinearity associated with $\sin \delta$ of (6-3).

The power angle δ at the transient stability limit increases from 72.85 degrees to 100.45 degrees. The results are unfamiliar because conventional wisdom sets 90 degrees as the steady-state stability limit. The power angle δ constitutes the angle difference between the voltage behind the reactance of the generator and the voltage of the infinite bus. The output voltage at the terminals of the generator is regulated at 1.0 pu by the feedback through field excitation.

In Table 6-II, the transient stability limit increases with k_{θ} decreases. The maximum power transmitted (0.75pu) within the transient stability limit is obtained when k_{θ} =-0.9, which is 42% more compared to k_{θ} =0 (0.53pu).

6.6.5 Impact of Damping Power on Ratings of MMC Components

Test results in Fig.6-8 show that in increasing the transient stability limit, the ratings of the MMC components are not exceeded. In the tests, the active power reference setting is set to zero, that is P_{ref} =0. This enables the active power required by damping to be evaluated in isolation.

Fig. 6-8 (a) shows the magnitude of the AC voltages across the point-of-common coupling of the MMC-HVDC station. From Fig. 6-8 (b), the peak values of currents from the MMC-HVDC

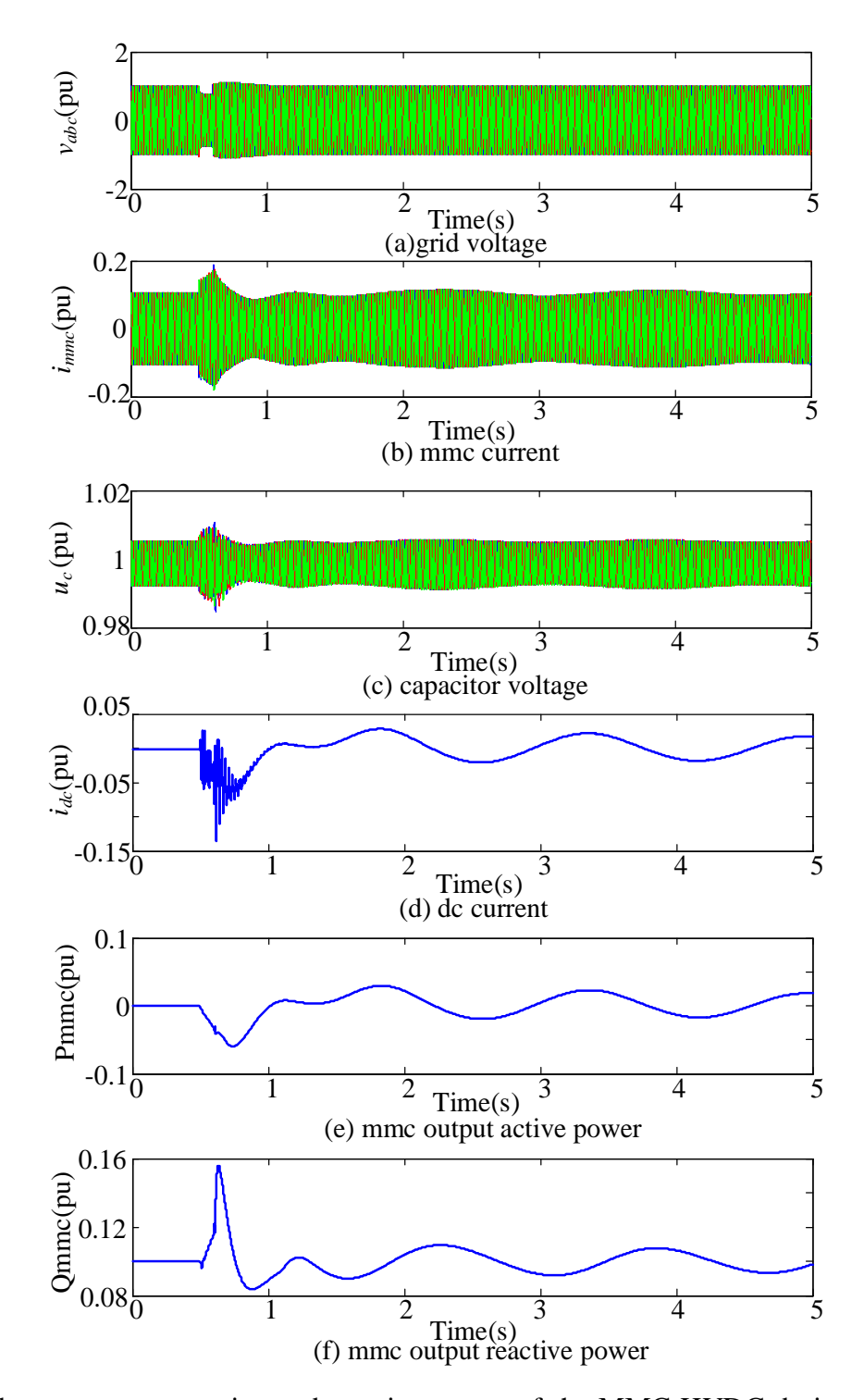


Fig. 6-8 Voltages, currents, active and reactive power of the MMC-HVDC during the transient stability test.

station is less than 0.20 pu during the fault. This is because regulated current control, by means of the deadbeat control [127][128], has been incorporated into the control. From Fig. 6-8(c), the

capacitor voltage across the sub-modules rises to 1.01 pu from 1.0 pu (SM voltage 2 kVdc). Because the active power is regulated at zero, Fig. 6-8(d) shows that the DC current spikes, at 0.14 pu at most in the DC bus. Fig.6-8(e) shows the deviations of active power in the 0.05 pu range. Fig.6-8(f) shows the reactive power drawn to support the AC voltage magnitude specified by *M* in (6-18) and (6-19).

6.7 Chapter Summary

This chapter shows that the MMC can provide Power Oscillation Damping (POD). Small signal analysis is applied to show that damping power must be proportional to the frequency of the power oscillation. An innovative passive local control method is proposed based on a three-phase phase-locked loop (PLL), which measures the frequency of the power oscillation without differentiation. The damping provided by the MMC to increase the active power transmissibility and transient stability is investigated. Furthermore, a universal control strategy is proposed and discussed, including the POD control, decoupled PQ control, second-order circulating current control, and reference current control deadbeat to protect the MMC from the AC side short circuit fault. A two-bus-one-generator system integrated alongside the MMC-HVDC is implemented in MATLAB SIMULINK as the test system through the ODE Model. The effect of damping the transient stability of the test system is evaluated, and the simulation results are presented. Results show that the MMC-HVDC can damp power oscillation and increase the transient stability limit so that power transmissibility is increased by 42%. Further, the results also prove that the employed deadbeat control is capable of protecting the MMC from the destructively large fault current induced by the AC system's short-circuit fault.

Chapter 7. Conclusions and Future Work

7.1 Conclusions

Modular-Multilevel-Converter (MMC)-based High Voltage Direct Current (HVDC) is the topology of choice for long-distance, bulk power transmission, and for underwater cable transmission, such as off-shore wind farms. This thesis focuses on the fast simulation capability of and control strategies for the MMC-HVDC. The main objectives are: (1) to develop a fast and accurate simulation model of a single MMC station and models of multi-terminal stations (MTDC); (2) to investigate design parameters for high damping; (3) to design a MMC-HVDC that has power oscillation damping (POD) capability.

In meeting the objectives, the following original contributions have been made:

- i. A fast and accurate analytical model based on Ordinary Differential Equations (ODEs) is developed for a single MMC-HVDC station and extended to Multi-Terminal systems (MTDC). Using the detail equivalent model (DEM) as a benchmark, the ODE model has the accuracy so that its simulation results lie under those of the DM model. The simulation is faster by a factor of 10.
- ii. The ODE model is nonlinear. Obtaining the steady-state solution requires the simulation to be long enough for the transients to have damped out. The Aprille and Trick method is applied for fast convergence to the steady-state (limit cycle) in one period of the system frequency of 50 or 60 Hz.
- iii. Small signal perturbation about the limit cycle yields a time-periodic characteristic matrix [A(t)]=[A(t+T)]. The small perturbation vector $\Delta\underline{x}(t)$ is shown to be related to the state-transition matrix $\Delta\underline{x}(t)=[\Phi(t,0)]\Delta\underline{x}(0)$. By applying the Floquet-Lyapunov Theorem, the state-transition matrix $\Phi(t,0)$ is constructed from [A(t)]. The dynamic properties of the MMC-HVDC are embedded in the eigenvalues of $\Phi(T,0)$. To be useful to designers, graphs of Damping Coefficients are prepared as functions of parameters (C_{arm} , L_m , L_{ac} , R_{ac}). From the graphs, designers can choose parameters sizes which optimize damping, and choose to avoid bad sizes which lead to instability caused by resonance.

- iv. The requisite signal to implement Power Oscillation Damping is $d\delta/dt$. The signals at the AC-terminals are functions of the voltage angle δ . The requisite signal is obtained through innovative application of the phase-locked loop (PLL) which extracts $d\delta/dt$, without incurring the noise associated with digital differentiation.
- v. The MMC-HVDC must have multi-function control capability. Many operators prefer to work with decoupled P-Q control. The MMC-HVDC must have a CCSC to suppress circulating current inside the sub-modules and the odd harmonics proliferated by circulating current on the AC-side. The MMC-HVDC can operate as the Power Oscillation Damper (POD). The MMC-HVDC must be protected from short-circuit AC-faults and the individual-phase Deadbeat control can achieve it. The schematic of such a universal controller is given. The capability of the universal controller is proven by simulations in which: (a) the harmonic proliferation is absent because of the CCSC; (b) power oscillation damping is introduced; (c) protection against short circuit fault is secured through the Deadbeat control.
- vi. Because of Deadbeat protection, the MMC-HVDC station survives destructively large AC-fault currents so that its Power Oscillation Damping capability is put to use so to extend the transient stability limit and thereby increasing the line transmissibility by a factor bigger than 20%.

7.2 Future Work

The thesis has explored several new ideas which have promise and are worth pursuing in further research. They are:

- (a) Developing the ODE model for simulation platforms for planning, operation and protection studies of a large hybrid AC-DC power system.
- (b) Universal control of multiple functions;
- (c) Study of stability and damping coefficients of the grid-connected VSC-HVDC or MMC-HVDC in accordance with the Floquet-Lyapunov Theorem.

Appendix A. Clarke and Park Transformation

Appendix A provides the theory of Clarke and Park transformation in Chapter 6.

With a-b-c to α - β transformation (also known as the Clarke transformation), variables of the stationary a-b-c frame can be converted into their equivalent variables of the stationary α - β frame:

$$\begin{bmatrix} f_{\alpha} \\ f_{\beta} \\ f_{\gamma} \end{bmatrix} = \begin{bmatrix} C \end{bmatrix} \begin{bmatrix} f_{a} \\ f_{b} \\ f_{c} \end{bmatrix}, \text{ where } \begin{bmatrix} C \end{bmatrix} = \frac{2}{3} \begin{bmatrix} 1 & -\frac{1}{2} & -\frac{1}{2} \\ 0 & \frac{\sqrt{3}}{2} & -\frac{\sqrt{3}}{2} \\ \frac{1}{2} & \frac{1}{2} & \frac{1}{2} \end{bmatrix}$$
(A-1)

where [C] is the Clarke transformation matrix.

This inverse transformation is

$$\begin{bmatrix} f_{a} \\ f_{b} \\ f_{c} \end{bmatrix} = [C]^{-1} \begin{bmatrix} f_{\alpha} \\ f_{\beta} \\ f_{\gamma} \end{bmatrix}, \text{ where } [C]^{-1} = \begin{bmatrix} 1 & 0 & 1 \\ -\frac{1}{2} & \frac{\sqrt{3}}{2} & 1 \\ -\frac{1}{2} & -\frac{\sqrt{3}}{2} & 1 \end{bmatrix}$$
(A-2)

where $[C]^{-1}$ is the inverse Clarke transformation matrix.

For a balanced three-phase system, $f_y=0$. Therefore, the simplified a-b-c to α - β transformation is

$$\begin{bmatrix} f_{\alpha} \\ f_{\beta} \end{bmatrix} = \begin{bmatrix} C_s \end{bmatrix} \begin{bmatrix} f_a \\ f_b \\ f_c \end{bmatrix}, \text{ where } \begin{bmatrix} C_s \end{bmatrix} = \frac{2}{3} \begin{bmatrix} 1 & -\frac{1}{2} & -\frac{1}{2} \\ 0 & \frac{\sqrt{3}}{2} & \frac{\sqrt{3}}{2} \end{bmatrix}$$
(A-3)

where $[C_S]$ is the simplified Clarke transformation matrix.

The simplified inverse transformation is

$$\begin{bmatrix} f_a \\ f_b \\ f_c \end{bmatrix} = \begin{bmatrix} C_s \end{bmatrix}^{-1} \begin{bmatrix} f_\alpha \\ f_\beta \end{bmatrix}, \text{ where } \begin{bmatrix} C_s \end{bmatrix}^{-1} = \begin{bmatrix} 1 & 0 \\ -\frac{1}{2} & -\frac{\sqrt{3}}{2} \\ -\frac{1}{2} & -\frac{\sqrt{3}}{2} \end{bmatrix}$$

$$(A-4)$$

where $[C_S]^{-1}$ is the simplified inverse Clarke transformation matrix.

With a-b-c to d-q transformation (also known as the Park transformation), variables of the stationary a-b-c frame can be converted into their equivalent variables of the rotational d-q frame:

$$\begin{bmatrix} f_d \\ f_q \\ f_0 \end{bmatrix} = \begin{bmatrix} P \end{bmatrix} \begin{bmatrix} f_a \\ f_b \\ f_c \end{bmatrix}, \text{ where } \begin{bmatrix} P \end{bmatrix} = \frac{2}{3} \begin{bmatrix} \cos(\omega t) & \cos(\omega t - 120^\circ) & \cos(\omega t + 120^\circ) \\ -\sin(\omega t) & -\sin(\omega t - 120^\circ) & -\sin(\omega t + 120^\circ) \\ \frac{1}{2} & \frac{1}{2} & \frac{1}{2} \end{bmatrix} \tag{A-5}$$

where [*P*] is the Park transformation matrix.

This inverse transformation is

$$\begin{bmatrix} f_a \\ f_b \\ f_c \end{bmatrix} = [P]^{-1} \begin{bmatrix} f_a \\ f_b \\ f_c \end{bmatrix}, \text{ where } [P]^{-1} = \begin{bmatrix} \cos(\omega t) & -\sin(\omega t) & 1 \\ \cos(\omega t - 120^\circ) & -\sin(\omega t - 120^\circ) & 1 \\ \cos(\omega t + 120^\circ) & -\sin(\omega t + 120^\circ) & 1 \end{bmatrix}$$
(A-6)

where $[P]^{-1}$ is the inverse Park transformation matrix.

For a balanced three-phase system, f_0 =0. Therefore, the simplified a-b-c to α - β transformation is

$$\begin{bmatrix} f_d \\ f_q \end{bmatrix} = \begin{bmatrix} P_s \end{bmatrix} \begin{bmatrix} f_a \\ f_b \\ f_c \end{bmatrix}, \text{ where } \begin{bmatrix} P_s \end{bmatrix} = \frac{2}{3} \begin{bmatrix} \cos(\omega t) & \cos(\omega t - 120^\circ) & \cos(\omega t + 120^\circ) \\ -\sin(\omega t) & -\sin(\omega t - 120^\circ) & -\sin(\omega t + 120^\circ) \end{bmatrix}$$
(A-7)

where $[P_S]$ is the simplified Park transformation matrix.

The simplified inverse transformation is

$$\begin{bmatrix} f_a \\ f_b \\ f_c \end{bmatrix} = [P_s]^{-1} \begin{bmatrix} f_d \\ f_q \end{bmatrix}, \text{ where } [P_s]^{-1} = \begin{bmatrix} \cos(\omega t) & -\sin(\omega t) \\ \cos(\omega t - 120^\circ) & -\sin(\omega t - 120^\circ) \\ \cos(\omega t + 120^\circ) & -\sin(\omega t + 120^\circ) \end{bmatrix}$$
(A-8)

where $[P_S]^{-1}$ is the simplified inverse Clark transformation matrix.

Appendix B. Digital Closed-Loop Deadbeat Control

Appendix B illustrates the digital closed-loop deadbead control in Chapter 6.

Fig. B-1 shows the block diagram of a digital closed-loop deadbeat control system. In Fig. B-1, $i_{refa}(t)$ and $i_a(t)$ stand for the reference current and for the measured feedback current for phase-a in time domain separately. Two control paths are included in the control diagram: a forward path and a feedback path. The forward path includes a control block $G_C(z)$, a computation delay block $G_D(z)$, a zero-order-hold (ZOH) block $G_{ZOH}(z)$, and the system plant block $G_P(z)$. The feedback path includes the control block $G_F(z)$. $G_2(z)$ is defined as the combination control blocks of computation delay, ZOH, and the plant block. Since the overall discrete transfer function for a digital deadbeat controller is z^{-2} , and since the system plant block $G_P(z)$ is decided by the system configurations, the main idea to design of the digital closed-loop deadbeat controller is to design a proper control block $G_C(z)$ and feedback control block $G_F(z)$.

The MMC plant circuit is shown in Fig. B-2. L_{ac} and R_{ac} represent the arm impedance and arm resistance, respectively. Therefore, in the continuous frequency domain, the ZOH block and the plant (L-R) in Fig. B-1 are:

$$G_{P}(S) = \frac{b}{S+a} \tag{B-1}$$

$$G_{ZOH}(S) = \frac{1 - e^{-s\Delta T}}{S}$$
 (B-2)

where, $a=R_{ac}/L_{ac}$, $b=1/L_{ac}$, ΔT is the delay period. Taking the Z transform of (B-1) and (B-2)

$$G_{P}(z)G_{ZOH}(z) = Z(G_{P}(s)G_{ZOH}(s)) = \frac{b}{a} \frac{1 - e^{-a\Delta T}}{1 - e^{-a\Delta T}z^{-1}} z^{-1}$$
(B-3)

The transfer function for the delay block is

$$G_n(z) = z^{-1} \tag{B-4}$$

Therefore, the defined $G_2(z)$ is the combination of (B-3) and (B-4),

$$G_2(z) = G_D(z)G_P(z)G_{ZOH}(z) = z^{-1}\frac{b}{a}\frac{1 - e^{-a\Delta T}}{1 - e^{-a\Delta T}z^{-1}}z^{-1} = \frac{b}{a}\frac{1 - e^{-a\Delta T}}{1 - e^{-a\Delta T}z^{-1}}z^{-2}$$
(B-5)

The main idea is to design a $G_C(z)$ and $G_F(z)$, so that

$$G(z) = \frac{I(z)}{I_{ref}(z)} = \frac{G_c(z)G_2(z)}{1 + G_F(z)G_c(z)G_2(z)} = Z^{-2}$$
(B-6)

z⁻² means a total delay of two sampling period will be introduced.

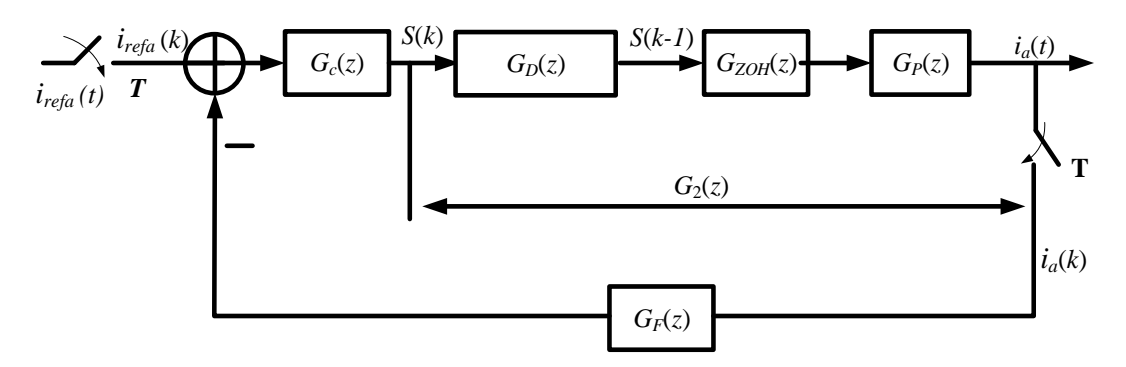


Fig. B-1 Schematic of digital current feedback of deadbeat control block.

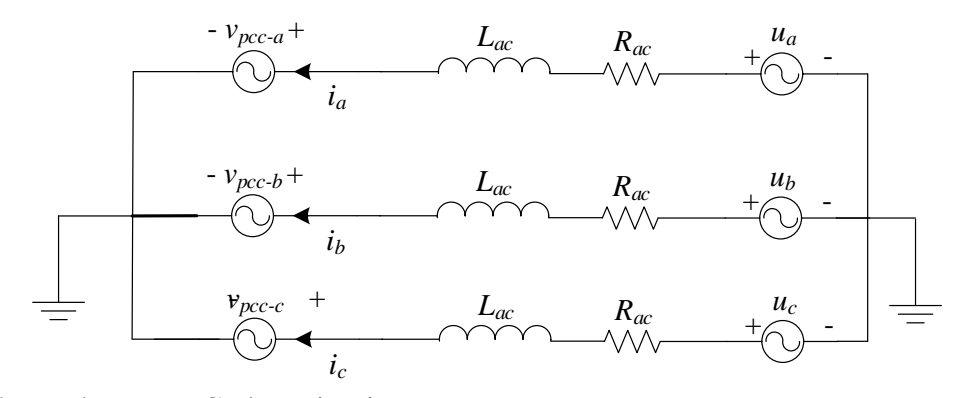


Fig. B-2 Three-phase MMC plant circuit.

Defining N(z) and D(z), as the numerator and denominator of a transfer function, respectively,

$$G_C(z) = \frac{N_C(z)}{D_C(z)}$$
 (B-7)

$$G_F(z) = \frac{N_F(z)}{D_F(z)} \tag{B-8}$$

Substituting (B-7) and (B-8) in (B-6)

$$G(z) = \frac{G_c(z)G_2(z)}{1 + G_F(z)G_c(z)G_2(z)} = \frac{N_C(z)D_F(z)\left(\frac{b}{a}1 - e^{-a\Delta T}\right)}{D_C(z)D_F(z)\left(1 - e^{-a\Delta T}z^{-1}\right)z^2 + N_C(z)N_F(z)\left(\frac{b}{a}1 - e^{-a\Delta T}\right)}z^{-1} = z^{-2} \quad (B-9)$$

Therefore,

$$N_C(z)D_F(z)\left(\frac{b}{a}1 - e^{-a\Delta T}\right) = 1$$
 (B-10)

$$D_{C}(z)D_{F}(z)\left(1 - e^{-a\Delta T}z^{-1}\right)z^{2} + N_{C}(z)N_{F}(z)\left(\frac{b}{a}1 - e^{-a\Delta T}\right) = z^{2}$$
(B-11)

Setting $D_F(z)=1$ [154], and substituting $D_F(z)$ in (B-11)

$$N_C(z) = \left(\frac{b}{a}1 - e^{-a\Delta T}\right)^{-1} = \frac{a}{b}\frac{1}{1 - e^{-a\Delta T}}$$
 (B-12)

Substituting $D_F(z)=1$ and (B-12) in (B-11)

$$D_C(z)(1 - e^{-a\Delta T}z^{-1})z^2 + N_F(z) = z^2$$
(B-13)

When $D_c(z)$ is defined as

$$D_C(z)=1+e^{-a\Delta T}z^{-1}$$
 (B-14)

Substituting (B-14) into (B-13)

$$N_F(z) = e^{-2a\Delta T} \tag{B-15}$$

Substituting (B-14) and (B-15) in (B-7) and (B-8),

$$G_C(z) = \frac{\frac{a}{b} \frac{1}{1 - e^{-a\Delta T}}}{1 + e^{-a\Delta T} z^{-1}}$$
 (B-16)

$$G_F(z) = e^{-2a\Delta T} \tag{B-17}$$

Appendix C. Parameters used in MMC-HVDC Damping Tests

Appendix C lists all the corresponding parameters used in MMC-HVDC damping tests in Chapter 6.

1) Generator (Standard GENROU Synchronous Machine)

$$\begin{aligned} \mathbf{S}_{B} &= 800 \mathrm{MW} \,, \ V_{B} = 230 \mathrm{kV} \,, \ f_{B} = 50 \mathrm{Hz} \,, \ H = 4.00 \,, \ r_{a} = 0 \,, \ x_{d} = 1.41 \mathrm{pu} \,, \ x_{d}' = 0.3 \, \mathrm{pu} \,, \\ x_{d}'' &= 0.2 \mathrm{pu} \,, \ x_{q} = 1.35 \mathrm{pu} \,, \ x_{q}' = 0.6 \, \mathrm{pu} \,, \ x_{q}'' = 0.2 \mathrm{pu} \,, \ x_{l} = 0.12 \mathrm{pu} \,, \ T_{do}' = 0.5 \mathrm{s} \,, \ T_{do}'' = 0.05 \mathrm{s} \,, \\ 0.05 \mathrm{s} \,, \ T_{do}' &= 0.7 \mathrm{s} \,, \ T_{do}'' = 0.1 \,. \end{aligned}$$

2) Turbine-Governor System (1981 IEEE type 2 turbine-governor model)

$$K = 20, T_1 = 50 \text{sec}, T_2 = 10 \text{sec}, T_3 = 1 \text{sec}, T_4 = 0.1 \text{sec}, P_{min} = 0, P_{max} = 1.5 \text{pu}$$

3) Field Excitation System. (IEEE type 1 synchronous machine voltage regulator combined to an exciter)

$$T_r = 0.02 \text{sec}, T_b = 0, T_c = 0, K_a = 200, T_a = 0.001 \text{s}, E f_{min} = 0, E f_{max} = 12.3 \text{pu}, K_p = 0, K_f = 0, T_f = 0$$

4) Transformers ($\Delta/Y-g$)

$$R_1 = 0.005$$
pu, $L_1 = 0.05$ pu, $R_2 = 0.005$ pu, $L_2 = 0.05$ pu.

5) Transmission Line (Distributed Pi Section)

Line 1 length:150km

Line 2-A length:75km, Line 2-A length:75km

 $r=0.0529\Omega/\text{km}$, l=0.0017H/km, c=1.0535e-08F/km

6) MMC

DC grid Voltage U_{dc} : 400kV

AC system nominal voltage: 230 kV

Number of Sub-modules per Arm N:200

Sub-module capacitor voltage:2kV

Arm Inductance L_m : 40mH

Arm Equivalent Resistance R_m : 0.1 Ω

SM Capacitance C_{SM} : 9mF

AC Equivalent Inductance L_{ac} : 20mH

AC Equivalent Resistance R_{ac} : 0.05 Ω

References

- [1] R. H, Mercury-Arc Current Converters, Pitman, 1941.
- [2] A. Canelhas, "High Voltage Direct Current (HVDC) Technology," 22 September 2010. [Online]. Available: http://www.alstom.com.
- [3] "Fact Sheet: High-voltage direct current transmission (HVDC)," July 2012. [Online]. Available: https://www.siemens.com/press/pool/de/events/2012/energy/2012-07-wismar/factsheet-hvdc-e.pdf.
- [4] "why-hvdc-economic and environmental advantages," ABB, [Online]. Available: https://new.abb.com/systems/hvdc/why-hvdc/economic-and-environmental-advantages.
- [5] D. Beaty and et al, Standard Handbook for Electrical Engineers, 11th Ed., McGraw Hill, 1978.
- [6] R. Rudervall, J. Charpentire and R. Sharma, "High voltage direct current (HVDC) transmission systems technology review paper," *Energy week*, vol. 2000, p. 2, 2000.
- [7] D. Tiku, "History," *IEEE Power & Energy Magzine*, March/Apil 2014.
- [8] Siemens, "HVDC-High-voltage direct current transmission," 2017. [Online]. Available: https://www.siemens.com/content/dam/webassetpool/mam/tag-siemens-com/smdb/energy-management/high-voltage-power-transmission/high-voltage-direct-current-transmission-systems-hvdc/hvdc/hvdc-referenzflyer.pdf.
- [9] R. C. Dorf, *The Electrical Engineering Handbook*, Second ed., CRC Press, 1997, p. 1343.
- [10] J. Sun, M. Li, Z. Zhang, T. Xu, J. He, W. Haijiao and L. Guanghui, "Renewable Energy Transmission by HVDC Across the Continent: System Challenges and Opportunities," *CSEE Journal of Power and Energy Systems*, vol. 3, no. 4, pp. 353-364, Dec. 2017.
- [11] "HVDC Classic- Reference List," 2013. [Online]. Available: https://library.e.abb.com/public/cc5e8e4e59c5231cc1257b2800575825/POW0013.pdf.
- [12] "Québec New England: The first large scale multiterminal HVDC transmission in the world to be upgraded," [Online]. Available: https://new.abb.com/systems/hvdc/references/quebec-new-england.
- [13] N. Flourentzou, V. G. Agelidis and G. D. Demetriades, "VSC-Based HVDC Power Transmission Systems: An Overview," *IEEE Transactions on Power Electronics*, vol. 24, no. 3, pp. 592-602, 2009.
- [14] G. P. Adam, I. A. Abdelsalam, K. H. Ahmed and B. W. Williams,, "Hybrid Multilevel Converter With Cascaded H-bridge Cells for HVDC Applications: Operating Principle and Scalability," *IEEE Transactions on Power Electronics*, vol. 30, no. 1, pp. 65-77, Jan, 2015.

- [15] Y. H. Liu, J. Arrillaga and N. R. Watson, "Cascaded H-Bridge Voltage Reinjection—Part I: A New Concept in Multilevel Voltage—Source Conversion," *IEEE Transactions on Power Delivery*, vol. 23, no. 2, pp. 1175-1182, Apr. 2008.
- [16] Y. H. Liu, J. Arrillaga and N. R. Watson, "Cascaded H-Bridge Voltage Reinjection—Part II: Application to HVDC Transmission,," *IEEE Transactions on Power Delivery*, vol. 23, no. 2, pp. 1200-1206, Apr. 2008.
- [17] A. Lesnicar and R. Marquardt, "An innovative modular multilevel converter topology suitable for a wide power range," in 2003 IEEE Bologna Power Tech Conference Proceedings, Bologna, Italy, 2003.
- [18] S. Du, A. Dekka, B. Wu and N. Zargari, "Role of Modular Multilevel Converters in The Power System," in *Modular Multilevel Converters: Analysis, Control, and Applications*, IEEE, 2018.
- [19] T. Westerweller, K. Friedrich, U. Armonies, A. Orini, D. Parquet and S. Wehn, "Trans Bay cable world's first HVDC system using multilevel voltage-sourced converter," in *CIGRÉ session*, Paris, 2010.
- [20] S. AG, "HVDC PLUS—the decisive step ahead: Stabilized power flows improve transmission grid performance," 2016. [Online]. Available: http://m.energy.siemens.com/US/pool/hq/power-transmission/HVDC/HVDC-PLUS/hvdc-plus_US.pdf.
- [21] "http://www.nrec.com/en/news-content-253.html," NR Electric Co., Ltd, [Online]. Available: http://www.nrec.com/en/news-content-253.html.
- [22] X. Han, W. Sima, M. Yang, L. Li, T. Yuan and Y. Si, "Transient Characteristics Under Ground and Short-Circuit Faults in a MMC-Based HVDC System With Hybrid DC Circuit Breakers,," *IEEE Transactions on Power Delivery*, vol. 33, no. 3, pp. 1378-1387, Jun. 2018.
- [23] S. Norrga, X. Li and L. Angquist, "Converter topologies for HVDC grids," in *IEEE International Energy Conference (ENERGYCON)*, Cavtat, 2014.
- [24] L. Zhang and et. al, "Modeling, control, and protection of modular multilevel converter-based multi-terminal HVDC systems: A review," *CSEE Journ. Power Energ. Syst.*, vol. 3, no. 4, pp. 340 352, Dec. 2017.
- [25] H. Rao, "Architecture of Nan'ao multi-terminal VSC-HVDC system and its multi-functional control," *CSEE Journ. Power Energ.*, vol. 1, no. 1, pp. 9-18, Mar. 2015.
- [26] Y. Li, X. Huang, J. Zhang and W. Sun, "China Upgrades Capacity to the Zhoushan Islands:State Grid Corporation installs first HVDC five-terminal voltage source converter project.," Mar.2017. [Online]. Available: https://www.tdworld.com/digital-innovations/china-upgrades-capacity-zhoushan-islands.
- [27] G. Tang, Z. He, H. Pang, X. Huang and X.-P. Zhang, "Basic topology and key devices of the five-terminal DC grid," *CSEE Journ. Power Energ. Syst.*, vol. 1, no. 2, pp. 22 35, Jun. 2015.
- [28] R. Irnawan, F. F. d. Silva, C. L. Bak and T. C. Bregnhøj, "An initial topology of multi-terminal HVDC transmission system in Europe: A case study of the North-Sea region," in *Proceedings of 2016 IEEE International Energy Conference (ENERGYCON)*, Leuven, Belgium, Jul. 2016.

- [29] L. He, K. Zhang, J. Xiong, S. Fan and Y. Xue, "Low-frequency ripple suppression for medium-voltage drives using modular multilevel converter with full-bridge submodules," *IEEE Trans. Emerg. Sel. Topics Power Electron.*, vol. 4, no. 2, pp. 657–667, Jun 2016.
- [30] Y. Li, X. Lyu and D. Cao, "A Zero-Current-Switching High Conversion Ratio Modular Multilevel DC–DC Converter," *IEEE Trans. Emerg. Sel. Topics Power Electron.*, vol. 5, no. 1, pp. 151 161, Mar. 2017.
- [31] G. J. Kish, "On the Emerging Class of Non-Isolated Modular Multilevel DC–DC Converters for DC and Hybrid AC–DC Systems," *IEEE Trans. Smart Grid*, vol. 10, no. 2, pp. 1762 1771, Mar. 2019.
- [32] B. Zhao, Q. Song, J. Li, Y. Wang and W. Liu, "Modular Multilevel High-Frequency-Link DC Transformer Based on Dual Active Phase-Shift Principle for Medium-Voltage DC Power Distribution Application," *IEEE Trans. Power Electron.*, vol. 32, no. 3, pp. 1779-1791, Mar. 2017.
- [33] Y. Wang, Q. Song, Q. Sun, B. Zhao, J. Li and W. Liu, "Multilevel MVDC Link Strategy of High-Frequency-Link DC Transformer Based on Switched Capacitor for MVDC Power Distribution," *IEEE Trans. Ind. Electron.*, vol. 64, no. 4, pp. 2829-2835, Apr. 2017.
- [34] B. Zhao, Q. Song, J. Li and W. Liu, "A Modular Multilevel DC-Link Front-to-Front DC Solid-State Transformer Based on High-Frequency Dual Active Phase Shift for HVDC Grid Integration," *IEEE Trans. Ind. Electron.*, vol. 64, no. 11, pp. 8919-8927, Nov. 2017.
- [35] M. Perez and et. al, "Circuit topologies, modeling, control schemes, and applications of modular multilevel converters," *IEEE Trans.Power Electron.*, vol. 30, no. 7, pp. 4-17, Jan 2015.
- [36] S. Debnath and et. al, "Operation, control, and applications of the modular multilevel converter," *IEEE Trans. Power Electron.*, vol. 30, no. 1, pp. 37-55, Jan 2015.
- [37] A. Dekka and et. al, "Evolution of Topologies, Modeling, Control Schemes, and Applications of Modular Multilevel Converters," *IEEE Trans. Emerg. Sel. Topics Power Electron.*, vol. 5, no. 4, pp. 1631-1656, Dec 2017.
- [38] M. Hagiwara, R. Maeda and H. Akagi, "Negative-sequence reactive power control by the modular multilevel cascade converter based on double-star chopper-cells (MMCC-DSCC)," in *Proc. IEEE Energy Convers. Congr. Expo.*, Sep. 2010.
- [39] A. Korn and et. al, "Direct modular multi-level converter for gearless low-speed drives," in *Proc.* 14th Eur. Conf. Power Electron. Appl, 2011.
- [40] R. Lizana, M. Perez and J. Rodriguez, "DC voltage balance control in a modular multilevel cascaded converter," in *Proc. IEEE Int. Symp. Ind.*, 2012.
- [41] P. Munch, D. Gorges, M. Izak and S. Liu, "Integrated current control, energy control and energy balancing of modular multilevel converters," in *Proc. IEEE 36th Annu. Conf. Ind. Electron. Soc.*, 2010.
- [42] L. Angquist, A. Haider, H.-P. Nee and H. Jiang, "Open-loop approach to control a modular multilevel frequency converter," in *Proc. 14th Eur. Conf. Power Electron. Appl.*, 2011.

- [43] T. Q., X. Z. and X. L., "Reduced switching-frequency modulation and circulating current suppression for modular multilevel converters," *IEEE Trans. Power Del.*, vol. 26, no. 3, pp. 2009–2017, 2011.
- [44] B. B., D. S. and S. M., "Circulating current suppression of the modular multilevel converter in a double-frequency rotating reference frame," *IEEE Trans. Power Electron.*, vol. 31, no. 1, pp. 783– 792, 2016.
- [45] Z. Li, P. Wang, Z. Chu, H. Zhu, Y. Luo and Y. Li, "An inner current suppressing method for modular multilevel converters," *IEEE Trans.Power Electron.*, vol. 28, no. 11, pp. 4873–4879, 2013.
- [46] X. She, A. Huang, X. Ni and R. Burgos, "AC circulating currents suppression in modular multilevel converter," in *Proc. 38th Annu. Conf. IEEE Ind. Electron. Soc. (IECON)*, Montreal, 2012.
- [47] X. She and A. Huang, "Circulating current control of double-star chopper-cell modular multilevel converter for HVDC system," in *Proc. 38th Annu. Conf. IEEE Ind. Electron. Soc. (IECON)*, Montreal, 2012.
- [48] M. Zhang, L. Huang, W. Yao and Z. Lu, "Circulating harmonic current elimination of a CPS-PWM-based modular multilevel converter with a plug-in repetitive controller,"," *IEEE Trans. Power Electron.*, vol. 29, no. 4, pp. 2083–2097, Apr. 2014.
- [49] L. He, K. Zhang, J. Xiong and S. Fan, "A repetitive control scheme for harmonic suppression of circulating current in modular multilevel converters," *IEEE Trans. Power Electron.*, vol. 30, no. 1, pp. 471–481, Jan. 2015.
- [50] J.-W. Moon, C.-S. Kim, J.-W. Park, D.-W. Kang and J.-M. Kim, "Circulating current control in MMC under the unbalanced voltage," *IEEE Trans. Power Del.*, vol. 28, no. 3, pp. 1952–1959, Jul. 2013.
- [51] Y. Zhou, D. Jiang, J. Guo, P. Hu and Y. Liang, "Analysis and control of modular multilevel converters under unbalanced conditions," *IEEE Trans. Power Del.*, vol. 28, no. 4, pp. 1986–1995, Oct. 2013.
- [52] S. Li, X. Wang, Z. Yao, T. Li and Z. Peng, "Circulating current suppressing strategy for MMC-HVDC based on nonideal proportional resonant controllers under unbalanced grid conditions," *IEEE Trans. Power Electron.*, vol. 30, no. 1, pp. 387–397, Jan. 2015.
- [53] B. Ooi and X. Wang, "Boost-type PWM HVDC transmission System," *IEEE Transaction on Power Delivery*, vol. 52, no. 4, pp. 1557-1563, October 1991.
- [54] B. Ooi and X. Wang, "Voltage angle lock loop control of the boost type PWM converter for HVDC application," *IEEE Trans. Power Eletron.*, vol. 5, no. 2, pp. 229-235, May 1990.
- [55] W. Lu and B. Ooi, "Multiterminal LVDC system for optimal acquisition of power in wind-farm using induction generators," *IEEE Trans. Power Electron.*, vol. 17, no. 4, pp. 558-563, July 2002.
- [56] B. M. Mwinyiwiwa, P. M. Birks and B. T. Ooi, "Delta-modulated buck-type PWM converter," *IEEE Trans. Ind. Appl.*, vol. 28, no. 3, pp. 552-557, May/June 1992..
- [57] M. Hagiwara and H. Akagi, "Control and Experiment of Pulsewidth-Modulated Modular Multilevel Converters," *IEEE Trans. Power Electron.*, vol. 24, no. 7, pp. 1737-1746, Jul. 2009.

- [58] J. Mei and et. al, "Modular Multilevel Inverter with New Modulation Method and Its Application to Photovoltaic Grid-Connected Generator," *IEEE Trans. Power Electron.*, vol. 28, no. 11, pp. 5063-5073, Nov. 2013.
- [59] G. S. Konstantinou, M. Ciobotaru and V. G. Agelidis, "Analysis of multi-carrier PWM methods for back-to-back HVDC systems based on modular multilevel converters," in *Proc. IEEE 37th Annu. Conf. Ind. Electron.*, 2011.
- [60] M. Saeedifard and R. ravani, "Dynamic Performance of a Modular Multilevel Back-to-Back HVDC System," *IEEE Trans. Power Del.*, vol. 25, no. 4, pp. 2903–2912, Oct. 2010.
- [61] B. P. McGrath, C. A. Teixeira and D. G. Holmes, "Optimised phase disposition (PD) modulation of a modular multilevel converter using a state machine decoder," in *Proc. IEEE Energy Convers. Congr.*, Sep. 2015.
- [62] B. P. McGrath, C. A. Teixeira and D. G. Holmes, "Optimized Phase Disposition (PD) Modulation of a Modular Multilevel Converter," *IEEE Trans. Ind. Appl.*, vol. 53, no. 5, pp. 4624 4633, 2017.
- [63] A. Dekka, B. Wu and N. R. Zargari, "A Novel Modulation Scheme and Voltage Balancing Algorithm for Modular Multilevel Converter," *IEEE Trans. Ind. Appl.*, vol. 52, no. 1, pp. 432-443, Jan. 2016.
- [64] Y. Deng, Y. Wang, K. H. Teo and R. G. Harley, "A Simplified Space Vector Modulation Scheme for Multilevel Converters," *IEEE Trans. Power Electron.*, vol. 31, no. 3, pp. 1873–1886, Mar. 2016.
- [65] Y. Deng and R. G. Harley, "Space-Vector Versus Nearest-Level Pulse Width Modulation for Multilevel Converters," *IEEE Trans. Power Electron.*, vol. 30, no. 6, pp. 2962–2974, Jun. 2015.
- [66] P. M. Meshram and V. B. Borghate, "A Simplified Nearest Level Control (NLC) Voltage Balancing Method for Modular Multilevel Converter (MMC)," *IEEE Trans. Power Electron.*, vol. 30, no. 1, pp. 450–462, Jan. 2015.
- [67] B4.57 Working Group, "Guide for the Development of Models for HVDC Converters in a HVDC Grid," *CIGRE*, Dec. 2014.
- [68] N. Lin and V. Dinavahi, "Exact Nonlinear Micromodeling for Fine-Grained Parallel EMT Simulation of MTDC Grid Interaction With Wind Farm," *IEEE Trans. Ind. Electron.*, vol. 66, no. 8, pp. 6427-6436, Aug. 2019.
- [69] S. Yan, Z. Zhou and V. Dinavahi, "Large-Scale Nonlinear Device-Level Power Electronic Circuit Simulation on Massively Parallel Graphics Processing Architectures," *IEEE Trans. Power Electron.*, vol. 33, no. 6, pp. 4660-4678, Jun. 2018.
- [70] N. Lin and V. Dinavahi, "Behavioral Device-Level Modeling of Modular Multilevel Converters in Real Time for Variable-Speed Drive Applications," *IEEE Trans. Emerg. Sel. Topics Power Electron.*, vol. 5, no. 3, pp. 1177 1191, Feb. 2017.
- [71] N. Lin and V. Dinavahi, "Variable Time-Stepping Modular Multilevel Converter Model for Fast and Parallel Transient Simulation of Multiterminal DC Grid," *IEEE Trans. Ind. Electron.*, vol. 66, no. 9, pp. 6661-6670, Sep. 2019.

- [72] J. Peralta and et. al, "Detailed and Averaged Models for a 401-Level MMC–HVDC System," *IEEE Trans. Power Del.*, vol. 27, no. 3, pp. 1501-1508, Jul. 2012.
- [73] H. Saad and et. al, "Dynamic Averaged and Simplified Models for MMC-Based HVDC Transmission Systems," *IEEE Trans. Power Del.*, vol. 28, no. 3, pp. 1723-1729, 2013.
- [74] U. N. Gnanarathna, A. M. Gole and R. P. Jayasinghe, "Efficient Modeling of Modular Multilevel HVDC Converters (MMC) on Electromagnetic Transient Simulation Programs," *IEEE Trans. Power Del.*, vol. 26, no. 1, pp. 316-324, 2011.
- [75] W. Li, L. Grégoire and J. Bélanger, "A Modular Multilevel Converter Pulse Generation and Capacitor Voltage Balance Method Optimized for FPGA Implementation," *IEEE Trans. Ind. Electron.*, vol. 62, no. 5, pp. 2859-2867, May 2015.
- [76] W. Li and J. Bélanger, "An Equivalent Circuit Method for Modeling and Simulation of Modular Multilevel Converters in Real-Time HIL Test Bench," *IEEE Trans. Power Del.*, vol. 31, no. 5, pp. 2401-2409, Oct. 2016.
- [77] H. Saad and et. al, "Real Time simulation of MMCs using the State-Space Nodal Approach," in *Conference on Power Systems Transients*, Vancouver, BC, Canada, Jul. 2013.
- [78] A. Antonopoulos, L. Angquist and H. Nee, "On dynamics and voltage control of the Modular Multilevel Converter," in *13th European Conference on Power Electronics and Applications*, Barcelona, 2009.
- [79] G. Bergna, M. Boyra and J. H. Vivas, "Evaluation and proposal of MMC-HVDC control strategies under transient and steady state conditions," in *Proceedings of the 2011 14th European Conference on Power Electronics and Applications*, Birmingham, 2011.
- [80] N. Ahmed and et. al, "A Computationally Efficient Continuous Model for the Modular Multilevel Converter," *IEEE Trans. Emerg. Sel. Topics Power Electron.*, vol. 2, no. 4, pp. 1139-1148, Dec. 2014.
- [81] S. R. Deore, P. B. Darji and A. M. Kulkarni, "Dynamic phasor modeling of Modular Multi-level Converters," in 2012 IEEE 7th International Conference on Industrial and Information Systems (ICIIS), Chennai, 2012.
- [82] D. Jovcic and A. A. Jamshidifar, "Phasor Model of Modular Multilevel Converter With Circulating Current Suppression Control," *IEEE Trans. Power Del.*, vol. 30, no. 4, pp. 1889-189, Aug. 2015.
- [83] J. Rupasinghe, S. Filizadeh and L. Wang, "A Dynamic Phasor Model of an MMC With Extended Frequency Range for EMT Simulations," *IEEE Trans. Emerg. Sel. Topics Power Electron.*, vol. 7, no. 1, pp. 30-40, Mar. 2019.
- [84] Y. Wei and et. al, "Real-Time Simulation of Hybrid Modular Multilevel Converters Using Shifted Phasor Models," *IEEE Access*, vol. 7, pp. 2376-2386, 2019.
- [85] T. Soong and L. P. W., "Internal Power Flow of a Modular Multilevel Converter With Distributed Energy Resources," *IEEE Trans. Emerg. Sel. Topics Power Electron.*, vol. 2, no. 4, pp. 1127-1138, Dec. 2014.

- [86] F. Deng and Z. Chen, "A Control Method for Voltage Balancing in Modular Multilevel Converters," *IEEE Trans. Power Electron.*, vol. 29, no. 1, pp. 66-76, Jan. 2014.
- [87] K. Wang, Y. Li, Z. Zheng and L. Xu, "Voltage Balancing and Fluctuation-Suppression Methods of Floating Capacitors in a New Modular Multilevel Converter," *IEEE Trans. Ind. Electron.*, vol. 60, no. 5, pp. 1943-1954, May 2013.
- [88] E. V. Larsen and D. A. Swann, "Applying Power System Stabilizers Part I: General Concepts," *IEEE Trans. Power Appa. Syst.*, Vols. PAS-100, no. 6, pp. 3017-3024, Jun. 1981.
- [89] "IEEE Recommended Practice for Excitation System Models for Power System Stability Studies," *IEEE Std 421.5-2005 (Revision of IEEE Std 421.5-1992)*, pp. 1-93, Apr. 2006.
- [90] G. Rogers, Power System Oscillations, Springer US, 2000.
- [91] I. Kamwa, R. Grondin and G. Trudel, "IEEE PSS2B versus PSS4B: the limits of performance of modern power system stabilizers," *IEEE Trans. Power Syst.*, vol. 20, no. 2, pp. 903-915, May 2005.
- [92] P. Kundur, "Power System Stability and Control," New York, McGraw-Hill, pp. 1128-1160, 1994.
- [93] D. Rimorov, I. Kamwa and G. Joós, "Model-based tuning approach for multi-band power system stabilisers PSS4B using an improved modal performance index,"," *IET Gen. Trans. Dist*, vol. 9, no. 15, pp. 2135-2143, Nov. 2015.
- [94] D. Rimorov, I. Kamwa and G. Joós, "Quasi-Steady-State Approach for Analysis of Frequency Oscillations and Damping Controller Design," *IEEE Trans. Power Syst.*, vol. 31, no. 4, pp. 3212-3220, Jul. 2016.
- [95] Y.-H. Song and A. Johns, Flexible Ac Transmission Systems (FACTS), IET, 1999.
- [96] R. L. Cresap and et. al, "Operating Experience with Modulation of the Pacific HVDC Intertie," *IEEE Trans. Power Appar. Syst.*, Vols. PAS-97, no. 4, pp. 1053-1059, Jul. 1978.
- [97] D. Trudnowski, D. Kosterev and J. Undrill, "PDCI damping control analysis for the western North American power system," in *IEEE Power & Energy Society General Meeting*, Vancouver, BC, 2013.
- [98] B. Yang, Z. Huang and D. Kosterev, "Multi-terminal subsystem model validation for pacific DC intertie," in 2008 IEEE Power and Energy Society General Meeting Conversion and Delivery of Electrical Energy in the 21st Century, Pittsburgh, PA., 2008.
- [99] D. V. Hertem, O. Gomis-Bellmunt and J. Liang, "HVDC Grids: For Offshore and Supergrid of the Future," in *Power system oscillation damping by means of VSC-HVDC systems*, IEEE, pp. 391-411, 2016.
- [100] L. Fan, "Yin and Z. Miao, "On Active/Reactive Power Modulation of DFIG-Based Wind Generation for Interarea Oscillation Damping," *IEEE Trans. Ener. Conv.*, vol. 26, no. 2, pp. 513-521, Jun. 2011.
- [101] Y. Wang and et. al, "Contribution of VSC-HVDC connected wind farms to grid frequency regulation and power damping," in *IECON 2010 36th Annual Conference on IEEE Industrial Electronics Society*, Glendale, AZ, 2010.

- [102] A. E. Leon and J. A. Solsona, "Power Oscillation Damping Improvement by Adding Multiple Wind Farms to Wide-Area Coordinating Controls," *IEEE Trans. Power Syst.*, vol. 29, no. 3, pp. 1356-1364, May 2014.
- [103] L. Zeni and et al., "Power Oscillation Damping From VSC–HVDC Connected Offshore Wind Power Plants," *IEEE Trans. Power Del.*, vol. 31, no. 2, pp. 829-838, Apr. 2016.
- [104] Y. Pipelzadeh and et al., "Coordinated Control of Offshore Wind Farm and Onshore HVDC Converter for Effective Power Oscillation Damping," *IEEE Trans. Power Syst.*, vol. 32, no. 3, pp. 1860-187, May 2017.
- [105] R. Preece and et al., "Damping of inter-area oscillations in mixed AC/DC networks using WAMS based supplementary controller,," *IEEE Trans. Power Syst.*, vol. 28, no. 2, pp. 1160-1169, May 2013.
- [106] M. Hadjikypris, O. Marjanovic and V. Terzija, "Damping of inter-area power oscillations in hybrid AC-DC power systems based on supervisory control scheme utilizing FACTS and HVDC," in *Power Systems Computation Conference (PSCC)*, Genoa, 2016.
- [107] J. Zhu and et al., "Coordinated Damping Control of VSC-HVDC Controllers and Wide Area Controllers," in *Asia-Pacific Power and Energy Engineering Conference*, Shanghai, 2012.
- [108] B. Pierre and et al, "Supervisory system for a wide area damping controller using PDCI modulation and real-time PMU feedback," in *IEEE Power and Energy Society General Meeting (PESGM)*, Boston, MA, 2016.
- [109] i. Jiang-Hafner and et al., "Improvement of subsynchronous torsional damping using VSC HVDC," in *Proceedings. International Conference on Power System Technology*, Kunming, China, 2002.
- [110] M. Bongiorno, J. Svensson and L. Angquist, "Single-Phase VSC Based SSSC for Subsynchronous Resonance Damping," *IEEE Trans. Power Del.*, vol. 23, no. 3, pp. 1544-1552, Jul. 2008.
- [111] S. Wang and Z. Xu, "An active damping scheme of the voltage-source converter driving the induction machine damping unit for mitigating subsynchronous oscillation in power systems," in 11th IET International Conference on AC and DC Power Transmission, Birmingham, 2015.
- [112] R. Thirumalaivasan, M. Janaki and N. Prabhu, "Damping of SSR Using Subsynchronous Current Suppressor With SSSC," *IEEE Trans. Power Syst.*, vol. 28, no. 1, pp. 64-74, Feb. 2013.
- [113] J. Chen, T. T. Lie and D. M. Vilathgamuwa, "Enhancement of power system damping using VSC-based series connected FACTS controllers," *in IEE Proceedings Generation, Transmission and Distribution*, vol. 150, no. 3, pp. 353-359, May 2003.
- [114] K. R. Padiyar and N. Prabhu, "Design and performance evaluation of subsynchronous damping controller with STATCOM," *IEEE Trans. Power Del.*, vol. 21, no. 3, pp. 1398-1405, Jul. 2016.
- [115] I. Kamwa, R. Grondin and Y. Hebert, "Wide-area measurement based stabilizing control of large power systems-a decentralized/hierarchical approach," *IEEE Trans. Power Syst*, vol. 16, no. 1, pp. 136-153, Feb. 2001.
- [116] G. Zhai, M. Ikeda and Y. Fujisaki, "Decentralized H∞ controller design: a matrix inequality approach using a homotopy method," *Automatica*, vol. 37, no. 4, pp. 565-572, 2001.

- [117] R.Ramos, L. Alberto and N. Bretas, "A new methodology for the coordinated design of robust decentralized power system damping controllers," *IEEE Trans. Power Syst*, vol. 19, no. 1, pp. 444-454, Feb. 2004.
- [118] D. Fan and et al., "Analysis on submodule monitoring strategy of Nan'ao multi-terminal VSC-HVDC transmission system," in *12th IET International Conference on AC and DC Power Transmission (ACDC 2016)*, Beijing, 2016.
- [119] N. T. Trinh, I. Erlich and S. P. Teeuwsen, "Methods for utilization of MMC-VSC- HVDC for power oscillation damping," in *2014 IEEE PES General Meeting | Conference & Exposition*, National Harbor, MD, 2014.
- [120] N. T. Trinh and et al., "Generic Model of MMC-VSC-HVDC for Interaction Study with AC Power System," *IEEE Trans. Power Syst*, vol. 31, no. 1, pp. 27-34, Jan. 2016.
- [121] N. T. Trinh and I. Erlich, "Analytical investigation of factors influencing controllability of MMC-VSC-HVDC on inter-area and local oscillations in interconnected power systems," in 2016 IEEE Power and Energy Society General Meeting (PESGM), Boston, MA, 2016.
- [122] G.-C. Hsieh and J. C. Hung, "Phase-locked loop techniques. A survey," *IEEE Trans. Ind. Electron.*, vol. 43, no. 6, pp. 609-615, Dec. 1996.
- [123] M. Karimi-Ghartemani, H. Karimi and M. R. Iravani, "A magnitude/phase-locked loop system based on estimation of frequency and in-phase/quadrature-phase amplitudes," *IEEE Trans. Ind. Electron.*, vol. 51, no. 2, pp. 511-517, Apr. 2004.
- [124] W. F. Egan, *Phase-Lock Basics*, New York: Wiley Inter-Science, 1998.
- [125] H. Awad, J. Svensson and M. J. Bollen, "Tuning software phase-locked loop for series-connected converters," *IEEE Trans. Power Del.*, vol. 20, no. 1, pp. 300-308, Jan. 2015.
- [126] M.Karimi-Ghartemani, "A novel three-phase magnitude-phase-locked loop system," *IEEE Trans. Cir. Syst. I: Regular Papers*, vol. 53, no. 8, pp. 1792-1802, Aug. 2006.
- [127] M. Karimi-Ghartemani and et al., "Derivation and Design of In-Loop Filters in Phase-Locked Loop Systems," *IEEE Trans. Instr. Meas.*, vol. 61, no. 4, pp. 930-940, Apr. 2012.
- [128] M. Karimi-Ghartemani and et al., "A New Phase-Locked Loop System for Three-Phase Applications," *IEEE Trans. Power Electron.*, vol. 28, no. 3, pp. 1208-1218, Mar. 2013.
- [129] M. Karimi-Ghartemani, "Linear and Pseudolinear Enhanced Phased-Locked Loop (EPLL) Structures," *IEEE Trans. Ind. Electron.*, vol. 61, no. 3, pp. 1464-1474, Mar. 2014.
- [130] S. Gao and M. Barnes, "Phase-locked loops for grid-tied inverters: Comparison and testing," in 8th IET International Conference on Power Electronics, Machines and Drives (PEMD 2016), Glasgow, 2016.
- [131] J. D. Ainsworth, "The Phase-Locked Oscillator A New Control System for Controlled Static Convertors," *IEEE Trans. Power Appa. Syst.*, Vols. PAS-87, no. 3, pp. 859-865, Mar. 1968.
- [132] C. Guo and et al., "A Frequency-Based Synchronization Approach for the VSC-HVDC Station Connected to a Weak AC Grid," *IEEE Trans. Power Del.*, vol. 32, no. 3, pp. 1460-1470, Jun. 2017.

- [133] T. J. Aprille and T. N. Trick, "Steady-state analysis of nonlinear circuits with periodic inputs," *Proceedings of the IEEE*, vol. 60, no. 1, pp. 108-114, Jan. 1972.
- [134] R. W. Brockett, Finite Dimensional Linear Systems, Society for Industrial and Applied Mathematics (SIAM), 2015.
- [135] P. Montagnier, R. J. Spiteri and J. Angeles, "The control of linear time-periodic systems using Floquet–Lyapunov theory," *International Journal of Control*, vol. 77, no. 5, pp. 472-490, Feb. 2007.
- [136] B. T. Ooi, "Steady State and Stability Analyses of the Single-Phase Induction Motor," in *IAS Conference Record* 72-CHO 763-31A, Milwaukee, Oct. 1973.
- [137] "Powering Real-Time Simulation," OPAL-RT TECHNOLOGIES, Inc, 2018. [Online]. Available: https://www.opal-rt.com/software-rt-lab/.
- [138] 徐政, "柔性直流输电系统," *MMC 的调制方式-MMC 的基本单元工作原理*, 北京, 机械工业出版社, pp. 19-20, 2017.
- [139] L.-A. Gregoire, W. Li, J. Belanger and L. Snider, "Validation of a 60-level modular multilevel converter model-overview of offline and real-time HIL testing and results," in *Proc. of IPST*, Delft, Netherlands, Jun. 2011.
- [140] R. U. Haque, S. Leng, N. Perera and J. Salmon, "Ripple voltage minimization in single phase floating bridge converter modules using a Transformer Coupled Asymmetrical bridge converter," in 2015 IEEE Applied Power Electronics Conference and Exposition (APEC), Charlotte, NC, 2015.
- [141] C. Wang, Q. Hao and B. Ooi, "Reduction of low-frequency harmonics in modular multilevel converters (MMCs) by harmonic function analysis," *IET Gen. Trans. & Dist.*, vol. 8, no. 2, pp. 328-338, Feb. 2014...
- [142] L. Harnefors and et. al, "Dynamic Analysis of Modular Multilevel Converters," *IEEE Trans. Ind. Electron.*, vol. 60, no. 7, pp. 2526-2537, Jul. 2013.
- [143] H. Wang, G. Tang, Z. He and J. Yang, "Efficient Grounding for Modular Multilevel HVDC Converters (MMC) on the AC Side," *IEEE Trans. Power Del.*, vol. 29, no. 3, pp. 1262-1272, Jun. 2014.
- [144] N. Ahmed and et al., "HVDC SuperGrids with modular multilevel converters The power transmission backbone of the future," in *International Multi-Conference on Systems*, Signals & Devices, Chemnitz, 2012.
- [145] Y. Jiao, "MPI Parallel Computing on Eigensystems of Small Signal Stability Analysis for Large Interconnected Power Grids," M.S. Thesis, Dept. Elect. Comp. Eng., McGill Univ., Montreal, QC, Canada, 2010.
- [146] M. Bach, "Estimating CPU Performance using Amdahls Law," Puget Systems, Auburn, WA, USA, 4 May 2015. [Online]. Available: https://www.pugetsystems.com/labs/articles/Estimating-CPU-Performance-using-Amdahls-Law-619/.

- [147] B.-T. Ooi, Y. Guo and H. C. Lee, "Capacitor break-point partitioning of multi-machine systems for numerical integration by parallel processing," *IEEE Trans. Ener. Con.*, vol. 11, no. 1, pp. 1-7, Mar. 1996.
- [148] R. M. Fano, L. J. Chu and R. B. Adler, Electromagnetic Fields, Energy and Forces, Wiley, pp. 249-259, 1960,.
- [149] W. Lu and B.-T. Ooi, "Optimal acquisition and aggregation of offshore wind power by multiterminal voltage-source HVDC," *IEEE Trans. Power Del.*, vol. 18, no. 1, pp. 201-206, Jan. 2003.
- [150] B. Mwinyiwiwa, Y. Zhang, B. Shen and B. Ooi, "Rotor Position Phase-Locked Loop for Decoupled P-Q Control of DFIG for Wind Power Generation," *IEEE Trans. Ener. Conv.*, vol. 24, no. 3, pp. 758-765, Sept. 2009.
- [151] C. Wang and B.-T. Ooi, "Incorporating deadbeat and low-frequency harmonic elimination in modular multilevel converters," *IET Gen.Trans. Dist.*, vol. 9, no. 4, pp. 369-378, 2015.
- [152] P. Kundur, "17.2 Small-Signal Stablity Enhancement," in *Power System Stability and Control*, New York, McGraw-Hill, pp. 1128-1160, 1994.
- [153] O. I. Elgerd, Electric Energy Systems Theory, McGraw-Hill, 1982.
- [154] J. Hu, *Deatbeat Controlled PWM Converter*, Montreal, Canada: M. Eng Thesis, McGill University, 1999.